2020

# EFFECTS OF HOLE TRANSPORTING LAYERS AND SURFACE LIGANDS ON INTERFACE ENERGETICS AND PHOTOVOLTAIC PERFORMANCE OF METHYLAMMONIUM LEAD IODIDE PEROVSKITES

So Min Park
*University of Kentucky*, somin.park@uky.edu
Author ORCID Identifier:
http://orcid.org/0000-0001-7677-5564
Digital Object Identifier: https://doi.org/10.13023/etd.2020.470

STUDENT AGREEMENT:

I represent that my thesis or dissertation and abstract are my original work. Proper attribution has been given to all outside sources. I understand that I am solely responsible for obtaining any needed copyright permissions. I have obtained needed written permission statement(s) from the owner(s) of each third-party copyrighted matter to be included in my work, allowing electronic distribution (if such use is not permitted by the fair use doctrine) which will be submitted to UKnowledge as Additional File.

I hereby grant to The University of Kentucky and its agents the irrevocable, non-exclusive, and royalty-free license to archive and make accessible my work in whole or in part in all forms of media, now or hereafter known. I agree that the document mentioned above may be made available immediately for worldwide access unless an embargo applies.

I retain all other ownership rights to the copyright of my work. I also retain the right to use in future works (such as articles or books) all or part of my work. I understand that I am free to register the copyright to my work.

REVIEW, APPROVAL AND ACCEPTANCE

The document mentioned above has been reviewed and accepted by the student's advisor, on behalf of the advisory committee, and by the Director of Graduate Studies (DGS), on behalf of the program; we verify that this is the final, approved version of the student's thesis including all changes required by the advisory committee. The undersigned agree to abide by the statements above.

So Min Park, Student

Dr. Yang-Tse Cheng, Major Professor

Dr. Matthew Beck, Director of Graduate Studies

# EFFECTS OF HOLE TRANSPORTING LAYERS AND SURFACE LIGANDS ON INTERFACE ENERGETICS AND PHOTOVOLTAIC PERFORMANCE OF METHYLAMMONIUM LEAD IODIDE PEROVSKITES

---

DISSERTATION

---

A dissertation submitted in partial fulfillment of the
requirements for the degree of Doctor of Philosophy in the
College of Engineering
at the University of Kentucky

By

So Min Park

Lexington, Kentucky

Directors: Dr. Yang-Tse Cheng, Professor of Chemicals and Materials Engineering

Lexington, Kentucky

2020


https://orcid.org/0000-0001-7677-5564

ABSTRACT OF DISSERTATION

# EFFECTS OF HOLE TRANSPORTING LAYERS AND SURFACE LIGANDS ON INTERFACE ENERGETICS AND PHOTOVOLTAIC PERFORMANCE OF METHYLAMMONIUM LEAD IODIDE PEROVSKITES

Organic metal halide perovskites are promising materials for various optoelectronic device applications such as light emitting diodes (LED) and photovoltaic (PV) cells. Perovskite solar cells (PSCs) have shown dramatic increases in power conversion efficiency over the previous ten years, far exceeding the rate of improvement of all other PV technologies. PSCs have attracted significant attention due to their strong absorbance throughout the visible region, high charge carrier mobilities, color tunability, and ability to make ultralight weight devices. However, organic metal halide perovskites still face several challenges. For example, their environmental stability issue must be overcome to enable widespread commercialization. Meeting this challenge involves material and interface development and optimization throughout the whole PV device stack. Fundamental understanding of the optical properties, electrical properties, interfacial energetics, and device physics is key to overcome current challenges with PSCs. In this dissertation, we report a new family of triarylaminoethynyl silane molecules as hole transport layers (HTLs), which are in part used to investigate how the PV performance depends on the ionization energy (IE) of the HTL and provide a new and versatile HTL material platform. We find that triarylaminoethynyl silane HTLs show comparable PV performance to the state-of-the art HTLs and demonstrate that different processing conditions can influence the IE of methylammonium lead iodide ($MAPbI_3$).

Surface ligand treatment provides a promising approach to passivate defect states and improve the photoluminescence quantum yield (PLQY), charge-carrier mobilities, material and device stability, and performance of PSCs. Numerous surface treatments have been applied to perovskite films and shown to passivate defect states and improve the PLQY and performance of PSCs, but it is not clear which surface ligands bind to the surface

and to what extent. As surface ligands have the potential to passivate defect states, alter interface energetics, and manipulate material and device stability, it is important to understand how different functional groups interact with the surfaces of perovskite films. We investigate a series of ligand binding groups and systematically probe the stability of the bound surface ligands, how they influence energetics, PLQYs, film stability, and PV device performance. We further explore ligand penetration and whether surface ligands prefer to remain on the surface or penetrate into the perovskite. Three variations of tail groups including aryl groups with varying extents of fluorination, bulky groups of varying size, and linear alkyl groups of varying length are examined to probe ligand penetration and the impact on material stability.

KEYWORDS: perovskite solar cells, methylammonium lead iodide, surface ligand, photoelectron spectroscopy

So Min Park

*(Name of Student)*

11/20/2020

Date

# EFFECTS OF HOLE TRANSPORTING LAYERS AND SURFACE LIGANDS ON INTERFACE ENERGETICS AND PHOTOVOLTAIC PERFORMANCE OF METHYLAMMONIUM LEAD IODIDE PEROVSKITES

By
So Min Park

Yang-Tse Cheng
Director of Dissertation

Matthew. J. Beck
Director of Graduate Studies

11/20/2020
Date

To my mother, father, and brother
who always has been supported my journey together

ACKNOWLEDGMENTS

I want to express my great appreciation to my research advisor Dr. Kenneth Graham, for his guidance and support past years during my graduate study. I have been always encouraged by his attitude to student with positive mind, kind heart, and patience. I would like to thank my academic advisor Dr. Yang-Tse Cheng, for his guidance and support as well. His enthusiastic and passionate attitude on work and warm caring on students made me always motivated to move forward. From both advisors, I have learnt not only the academic knowledge but also the more important values in my life.

My sincere thanks also go to my committee members Dr. Matthew Beck, and Dr. Jonathan Pham for their input and help on the research over past couple of years, and my collaborator Dr. John Anthony for providing the materials for the research.

I want to thank my group members especially Dr. Ashkan Abtahi, for his dedication to his effort and help on the almost every instruments set up and software for material characterization measurements in the lab, and surface coverage calculation for my project, and Dr. Alex Boehm, for his PES instruments set up and maintenance. I will not forget the time when we built the lab together from an empty room with the excitement as initial group members and all the memory on breaking and fixing stuff together. Thank you for your time and for your willingness to help. I also want to thank experimental help from Harindi Atapattu, and Dr. Aslam Uddin in the group, and other group members and my friend John Dunlap, Thuy Nguyen, Tuo Liu, Henry Pruett, Tareq Hossain, Joy Syed, and Kyle Baustert.

I want to thank all my friends back home in Korea, So Hee Kim, Eun Jung Kim, Hannah Lee, Hannah Lim, Kyeung Eun Kim, and Hyo Jung Jo, for their belief, support,

and friendship. Especially I also want to thank my friend who encouraged me a lot my new adventure life in America here, Lauren Hannemann and Laura Hoch. You and your family's warm heart really touched me, and I enjoyed a lot with you.

Most importantly, I want to thank my family and I want to say I love you the most my mother, father, and younger brother who always have been believed and supported me and encouraged the decision that I wanted to do even though that is sending your daughter to far from the family. However, we were always together every happy, sad, or struggle moments. I will join Dr. Ted Sargent group at University of Toronto, Canada as a postdoctoral fellow to do a further research after Ph.D. In 2020 pandemic, everything was pushed back, and I have not been home more than 2 years, but I believe I can go back home soon to see my family.

Finally, I would like to thank University of Kentucky and U.S Department of Energy, Office of Basic Energy Sciences, for the financial support to conduct a research from 2017 to 2020.

TABLE OF CONTENTS

LIST OF TABLES

LIST OF FIGURES

# CHAPTER 1. INTRODUCTION TO METAL HALIDE PEROVSKITES

## 1.1 Halide perovskite materials

Metal halide perovskites were first applied to dye-sensitized solar cells (DSSCs) by the Miyasaka group, where they demonstrated 3.8% power conversion efficiency (PCE) in 2009.[1] However, this initial work did not receive much attention due to the low PCE and instability of the liquid electrolyte. The PCE was increased significantly with optimized perovskite precursor solution and electrolyte composition to 6.5% in 2011,[2] and an all-solid-state perovskite thin film photovoltaic (PV) with 9% PCE was reported by the Park group in 2012.[3] Since then, perovskite solar cells (PSCs) have rapidly emerged as the most competitive third generation PV technology. PCEs of lead-based single junction perovskite devices over 25% have recently been demonstrated in small, laboratory-scale devices in 2020.[4] Considering the history of PV research since the 1960s, this PSC improvement is dramatic. Aside from PCE improvements, these perovskite PV cells have attracted significant research efforts due to the use of inexpensive materials and low processing cost combined with the ability to make ultralight weight devices. These advantages hold great promise for a wide variety of optoelectronic devices such as light emitting diodes (LEDs), PVs, photodetectors, lasers, etc.

### 1.1.1 Perovskite crystal structure

Perovskite refers to a class of compounds that share a similar crystal structure and stoichiometry, such as metal oxide perovskites $SrTiO_3$ and $BaTiO_3$. Most recent efforts on PVs have focused primarily on three dimensional (3D) organic lead-based metal halide perovskites, $APbX_3$. Methylammonium lead iodide ($MAPbI_3$) consists of

methylammonium ($CH_3NH_3^+$, MA) for the A site organic cation, lead (Pb) for the B site metal cation, and iodide (I) as X site halides as shown in Figure 1.1. With $ABX_3$ stoichiometry, charges of the cation must satisfy the values A = +1, and B = +2, and anion must satisfy X = -1 for charge neutrality.

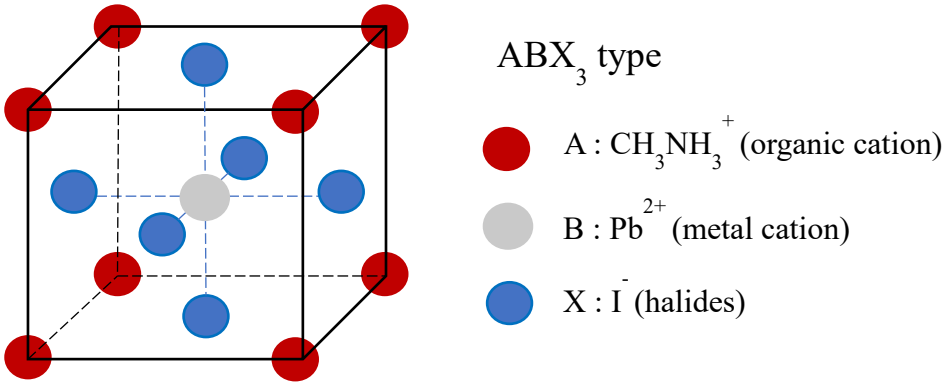


Figure 1.1 Perovskite crystal structure of methylammonium lead iodide ($MAPbI_3$)

Typically, three dimensional halide perovskites (HPs) are composed of A-site organic cations such as methylammonium ($CH_3NH_3^+$, MA), formamidinium ($CH(NH_2)_2^+$, FA), or cesium (Cs), B-site metals such as lead (Pb) or tin (Sn), and X-site halides including iodide (I), bromide (Br), or chloride (Cl). Recently, mixed cation and mixed halide PSCs have attracted a lot of research attention due to their improved PV performance and long-term stability. The Goldschmidt tolerance factor (t) is important to determine if a 3D perovskite structure will form and predict the stability of the crystal structure as given by equation (1), where $r_A$ is the radius of the A cation, $r_B$ is the radius of the B cation, and $r_X$ is the radius of the anions.

$$t = \frac{r_A + r_X}{\sqrt{2}(r_B + r_X)} \qquad (1)$$

Generally, HP materials have a cubic black phase with the value of $0.8 < t < 1$. The closer the $t$ value is to 1, the more stable the cubic black phase.[5–7] In case of $t < 0.8$, this material tends to form a yellow phase, as the $BX_6$ octahedral structure becomes less stable, which leads to tetragonal and orthorhombic phases rather than cubic structure.

### 1.1.2 Perovskite optical and electronic properties

The absorption coefficient is a vital parameter for photovoltaic materials, as it determines how much sunlight can be absorbed by a given material thickness. The absorption spectra of $MAPbI_3$ have very sharp band edges nearly close to gallium arsenide (GaAs) as shown in Figure 1.2.[8] The slope of this exponential part of the curve can be fit to extract the Urbach energy[9] and this slope is partly due to the absorption of tail states within the film. This sharp onset suggests that no optically detectable deep states exist within the bandgap of the perovskite film, which is beneficial for high performance PSCs. High absorption coefficient of $MAPbI_3$ means this perovskite material can absorb light more effectively with thinner layers compared to other inorganic materials.

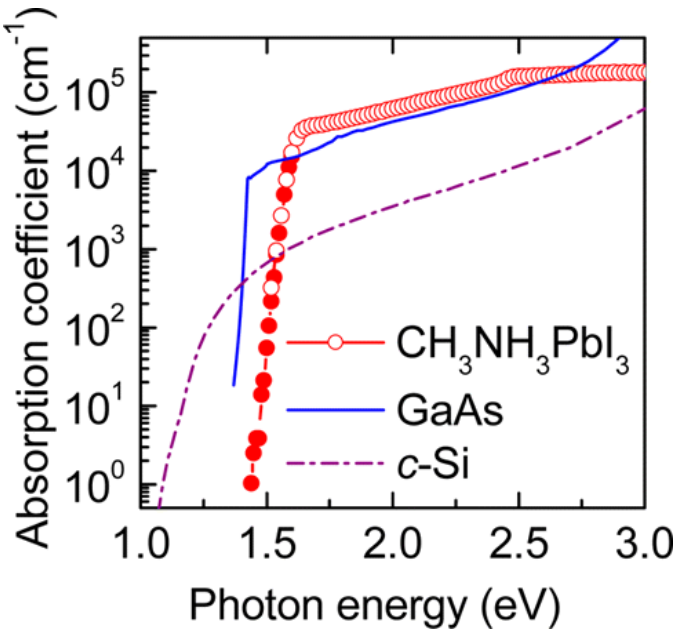


Figure 1.2 Absorption coefficient comparison between $MAPbI_3$ and other inorganic PV materials. Reprinted with permission from "Wolf, S. D.; Holovsky, J.; Moon, S. J.; Loper, P.; Niesen, B.; Ledinsky, M.; Haug, F. J.; Yum, J. H.; Ballif, C. Organometallic Halide Perovskites: Sharp Optical Absorption Edge and Its Relation to Photovoltaic Performance. The Journal of Physical Chemistry Letters 2014, 5, 1035-1039" Copyright (2014) American Chemical Society.

Following the Pauli exclusion principle that multiple electrons are not allowed to occupy the same state, for solid with many nearby atoms an energy band of electrons will be formed. In semiconductors the bandgap ($E_G$) is the difference between valence band (VB) edge and the conduction band (CB) edge, as shown in Figure 1.3a. The Fermi level ($E_F$) is the energy of the electronic state that has a 50% of probability of being occupied at any given time. In semiconductors without any impurities or defects, $E_F$ falls in the middle of the bandgap versus metals where $E_F$ is located within the CB. The work function (WF) is the energy required to remove an electron from the Fermi level to vacuum. The energy required to remove an electron from the valence band maximum (VBM) to the vacuum level is called the ionization energy (IE), and the energy gained by adding an electron to

the conduction band minimum (CBM) is called the electron affinity (EA). In a PV cell, $E_G$ is an important parameter to understand physical properties of the material that enable prediction of the wavelength of light that will be absorbed by the material. By changing and mixing the cation and anions in the perovskite structure, $E_G$ can be tuned.

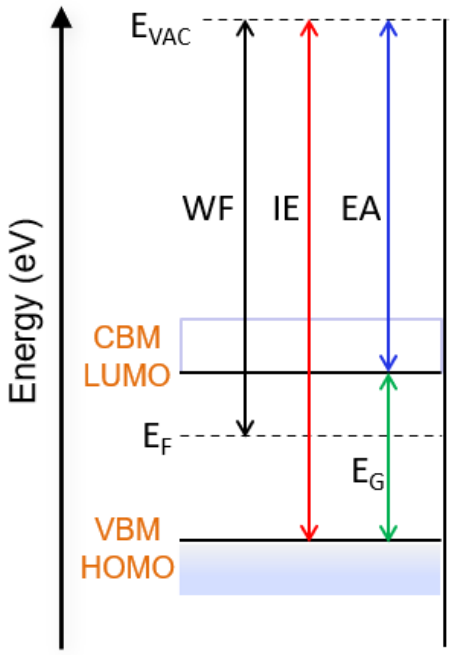


Figure 1.3 Energy level diagram showing VBM, CBM, WF, IE, EA, $E_F$, and $E_G$.

## 1.2 Solar cell device operation

A PV cell is a device that converts light into electrical energy. The schematic of a PSC showing the operating process is depicted in Figure 1.4. First, when sun light shines on the PV device the perovskite material will absorb the light and can generate electron and hole pairs. These excitons are generated in a PV cell when incident photons have energy greater than the bandgap and are absorbed by the perovskite. These excitons are separated into holes and electrons, which diffuse to the interface with the electron transport

layer (ETL) or hole transport layer (HTL). Charges are collected at the electrodes. To obtain efficient charge extraction without loss from charge recombination, well-aligned energetic offsets are essential for the device. For example, the optimum CBM of ETL is about 0.0~0.3 eV lower than the CBM of the light absorber layer.[10] If CBM of ETL becomes higher than the CBM of the perovskite layer, electron transfer path will be energetically unfavorable, and this will result in charge recombination at the interface.

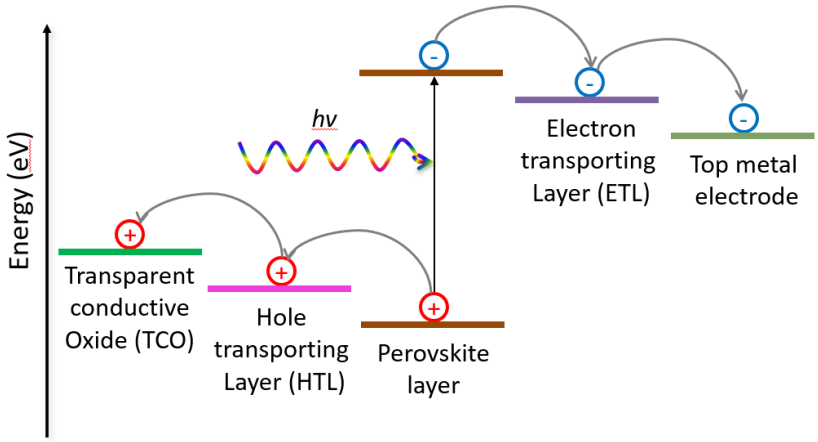


Figure 1.4 Schematic of operating processes within a PSC

The PCE of the PV device is calculated by equation (2), which is determined by the ratio of maximum output power to the incident light power ($P_{in}$).

$$\text{PCE}\ (\%) = \frac{\text{FF x } J_{sc} \text{ x } V_{oc}}{P_{in}} \text{ x } 100 \qquad (2)$$

The PCE of a device can be characterized from current-voltage (IV) measurements recorded while the solar cell is under illumination. All these PV parameters are shown in the IV curve in Figure 1.5. Voltage is applied in a range across the PV device and the current is measured. The open circuit voltage ($V_{oc}$) is defined as the maximum voltage that

can be generated across the device under illumination when there is zero current. Short circuit current density ($J_{sc}$) is defined as the maximum current that can be extracted from the solar cell when there is zero voltage between the electrodes. The $J_{sc}$ depends on the generation and collection of light-generated carriers, absorption coefficient and thickness of the light absorber and carrier lifetime. Fill factor (FF) is the ratio of the maximum power generated by the cell to the product of the $V_{oc}$ and $J_{sc}$ as described in equation (3).

$$FF = \frac{V_{max}J_{max}}{V_{oc}J_{sc}} \qquad (3)$$

Therefore, maximizing these parameters is key to obtaining highly efficient devices.

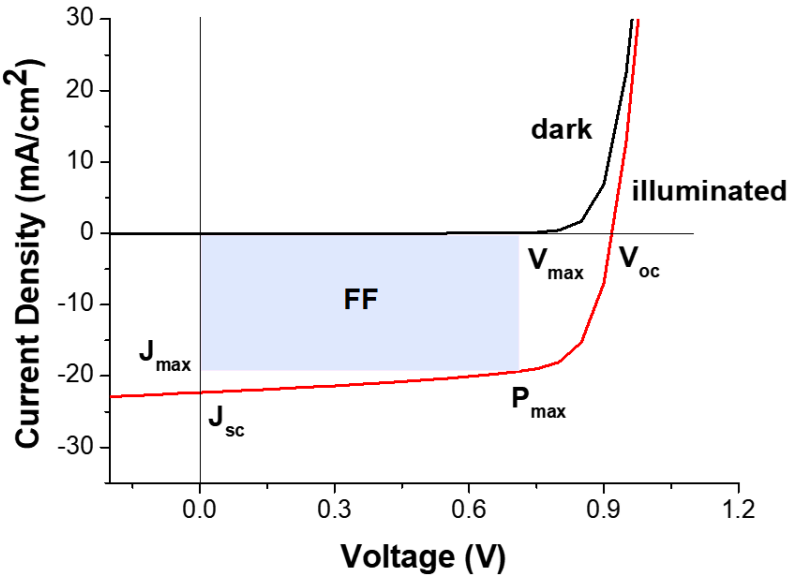


Figure 1.5 IV curve showing PV parameters of PV cell

## 1.3 Challenges facing halide perovskite research field

There are multiple challenges that need to be solved to enable the commercial development of PSCs. One of the major challenges is the environmental stability. PSC materials easily degrade in the presence of moisture, resulting in decreased device

performance. It has been shown that water molecules form weak hydrogen bonds with the MA cation[11,12] and this decomposes the perovskite crystal structure. With enough moisture, $MAPbI_3$ can decompose to aqueous MAPbI and $PbI_2$ phase and this aqueous MAPbI is further separated to methylamine and hydroiodic acid.[13–15] In direct contact with perovskite and top metal electrode used in device, Zhao et al. have also shown that $MAPbI_3$ completely decompose through the redox reaction between Al and $MAPbI_3$ in which $Pb^{2+}$ is reduced to $Pb^0$.[16] Methylammonium iodide (MAI) tends to evaporate while thermal annealing the film due to high volatility and instability of MAI, thus perovskite film forms $PbI_2$ rich surface and lose the original PV performance. The thermal degradation of $MAPbI_3$ and MAI releases $NH_3$ and $CH_3I$ as degradation products as low as 80 °C according to reports based on thermal gravimetric and differential thermal analysis (TG-DTA) coupled with quadrupole mass spectrometry (MS) instrumentation.[17] Additionally, all the most efficient perovskite PVs contain Pb. There are legitimate concerns about toxicity of Pb in large scale utilization that contaminates soil and water. Researchers are aware of these possible health problems and raising concerns, but these arguments are still under debate because many researchers think that the minimal amounts of lead are safe enough to use. Also, the environmental regulation limits vary between countries.

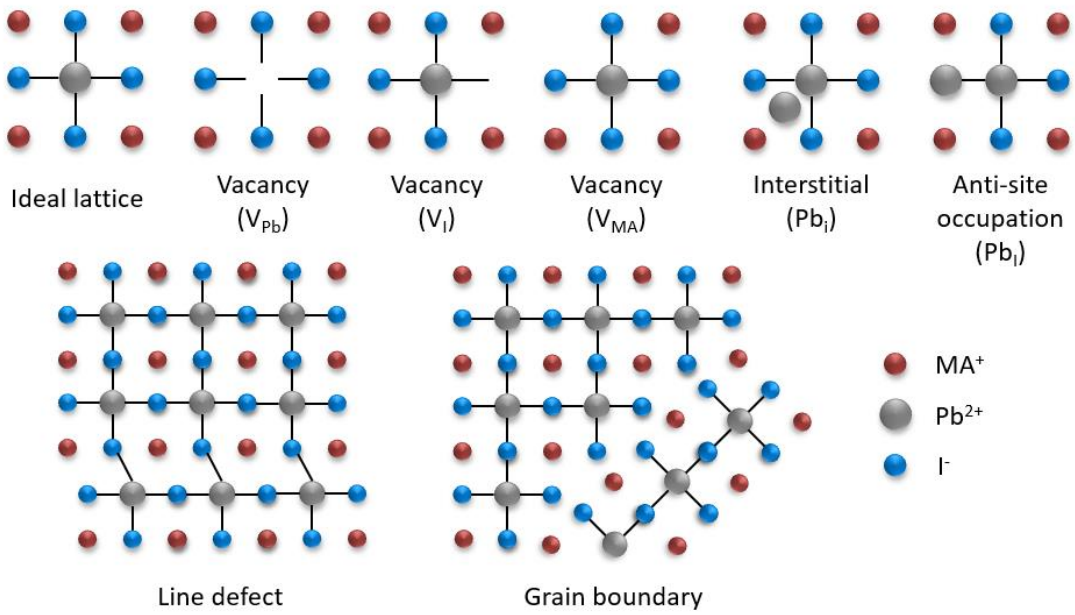


Figure 1.6 Schematics of defect types in $MAPbI_3$ crystal structure. The red circle represents methylammonium ($MA^+$), grey circle represents lead ($Pb^{2+}$), and blue circle represents iodide ($I^-$)

Interfaces and grain boundaries can cause shallow or deep trap states that facilitate charge recombination. They are easily exposed to moisture or oxygen which eventually lead to lower performance of the device. In case of $MAPbI_3$, possible trap states include vacancies such as methylammonium ($MA^+$) vacancy ($V'_{MA}$), lead vacancy ($V''_{Pb}$), and iodide vacancy ($V_I^{\bullet}$) with Kroger-Vink notation. Loss of $MA^+$ due to its low thermal stability will cause A-site MA vacancies ($V'_{MA}$). These A-site vacancies leave negatively charged sites, which attract positive charges due to coulombic force. These negative charges will therefore act as trap states for positive charges, which leads to charge recombination. In terms of interstitials, these three can again be $MA_i$, $Pb_i$, $I_i$. For anti-site occupation, examples are $MA_{Pb}$, $MA_I$, $Pb_{MA}$, $Pb_I$, $I_{MA}$, $I_{Pb}$. Among those, the most common surface defect is under-coordinated $Pb^{2+}$ metal cations because $I^-$ ions move out under electric field. These positive

charges of $Pb^{2+}$ will act as trap states for negative charge in a similar way. This iodide vacancy ($V_I$) will generate sub gap states within the band gap that induce non-radiative recombination, which lead to a decrease of photoluminescence quantum yield (PLQY). These trap states and induced ion migration can cause the thermal and light degradation of the device, which affects the device operational mechanisms and eventually lead to the failure of the device.

## 1.4 Hole transport layers (HTLs) and material energetics

In a typical PV device architecture, the perovskite light absorber layer with a thickness of 200-300 nanometers is sandwiched between HTL and ETL. To improve charge extraction and minimize charge recombination, charge transfer processes between interlayers are very important. Each transport layer needs to have good charge carrier mobility, as well as well-aligned energy levels with other layers to help charge transfer efficiently and without energy losses. Especially in PSC research area, HTL plays an essential role in determining the device performance. A wide range of materials have been used for the HTL, including inorganic materials such as nickel oxide ($NiO_x$), and copper iodide (CuI), organic small molecules, and conjugated polymers like poly(3,4-ethylenedioxythiophene):polystyrene sulfonate (PEDOT:PSS) and poly[bis(4-phenyl)(2,4,6-trimethylphenyl)amine] (PTAA). 2,2',7,7'-Tetrakis[N,N-di(4-methoxyphenyl)amino]-9,9'-spirobifluorene (Spiro-OMeTAD) is the small molecule that has been most commonly used as an HTL in PSCs. Spiro-OMeTAD usually requires additional doping to increase the conductivity, such as can be achieved by introducing 4-

tert-butylpyridine (TBP) and/or lithium bis(trifluoromethanesulfonyl)imide (Li-TFSI). Even though using doped Spiro-OMeTAD for HTL showed high-efficient device, this material has tedious synthesis steps and low stability that eventually lower the device performance. Recently, many efforts have been introduced to replace Spiro-OMeTAD while keeping the high PCE. The VBM of HTL is expected to be slightly higher than the perovskite layer which provides the driving force for charge transfer process. Additionally, HTL can act as electron blocking layer that prevents electrons from reaching the anode.

## 1.5 Surface modification of halide perovskites

Interfaces and grain boundaries are more prone to trap state formation and degradation processes, thus recent work has focused on using surface ligands to passivate these surface states and grain boundaries. Interfaces and boundaries of multi crystalline grains can cause trap states which will induce charge recombination, decrease film quality, and decrease efficiency of the devices. Non-stoichiometric defect surfaces often contain multiple point defects such as vacancies, interstitial, and anti-sites. As mentioned previously, MA vacancies are one type of surface defects. These A-site vacancies leave negatively charged sites, which attract positive charge due to coulombic force.

Recently, surface modifications of perovskite layer have been studied to understand how they passivate the surface trap states and influence interfacial energetics, optical properties, device performance, and stability. There are two primary classes of surface ligands that can be applied to modify perovskite thin films. One is ammonium containing ligands, and the other is ligands that can act as Lewis bases and coordinate with Pb.

Ammonium containing ligands are not directly passivating electronically harmful defect states, but they can protect the perovskite layer from harmful degradation reactions with oxygen, water, or top metal electrodes. On the other hand, coordination of Lewis bases can eliminate the shallow defect states and reduce the level of non-radiative recombination. These ligands on the surface also influence the electronic structure of $MAPbI_3$ at the surface by changing the surface states which effect the charge transfer at the interface. However, systematic studies on the mechanism of how the surface ligands bind the perovskite sites and how interfacial energetics impact on optical, electrical, and PV properties are not fully understood in the community.[18–20]

## 1.6 Outline of dissertation

### Chapter 2 EXPERIMENTAL TECHNIQUES AND DEVICE OPTIMIZATION

This chapter discusses the materials and perovskite thin film device fabrication used throughout this dissertation. The chapter discusses the device architecture for PSC and further experimental optimizations to obtain uniform morphology and high-quality perovskite thin film. Furthermore, various measurement techniques to characterize the optical and electrical properties of the perovskite thin films are discussed in this chapter.

### Chapter 3 EFFECTS OF HOLE TRANSPORT LAYER IONIZATION ENERGY ON PEROVSKITE PVS

The performance and stability of PSC can be greatly improved through the understanding of each layer of the whole PSC device. The hole transport layer (HTL) influences charge extraction and recombination processes. The ionization energy (IE) of

the HTL is one important material property that will determine the open-circuit voltage, fill factor, and short-circuit current. This chapter discusses the influence of the HTL IE on the PV performance of $MAPbI_3$. We introduce a new family of triarylaminoethynylsilane molecules with adjustable IEs as efficient HTL materials for $MAPbI_3$ perovskite-based device. We further study how two different $MAPbI_3$ processing methods effect the PV performance of $MAPbI_3$ based perovskite devices with a series of 11 different HTL materials, with IEs ranging from 4.74 to 5.84 eV.

Chapter 4 SURFACE LIGANDS FOR PEROVSKITE THIN FILMS: SURFACE COVERAGE, ENERGETICS, AND PV PERFORMANCE

Interfaces in PSCs exert a massive influence over the PV performance, as these interfaces dominate charge-carrier recombination and are often where degradation processes begin. A promising means of reducing interfacial recombination and improving material and device stability is through appending surface ligands to perovskite layers. Surface ligand treatment provides an approach to passivate defect states, improve material and device stability, manipulate interfacial energetics, and increase the performance of PSCs. To facilitate targeted selection and design of surface ligands for PSCs, it is necessary to establish relationships between ligand structure and perovskite surface properties. This chapter discusses the extent of surface coverage of surface ligands with different binding groups, whether they form a surface monolayer or penetrate the perovskite, how these surface ligands effect material energetics and PL, and how this combination of factors influences PV performance.

Chapter 5 DESIGNING AMMONIUM CONTAINING SURFACE LIGANDS TO FORM SURFACE SEGREGATED MONOLAYERS

To investigate whether surface ligands prefer to remain on the surface or penetrate into $MAPbI_3$, we studied ammonium functionalized surface ligands designed with bulky substituents and varying extents of fluorination. We vary the surface energy by changing the extent of fluorination and the positions of fluorine in anilinium iodide derivatives, while the size is varied through introducing branched alkyl groups, adamantane, cyclohexanemethyl, or tert-butyl substituted aromatic units to the ammonium cation. Through a combination of XRD and angle-dependent XPS we clearly establish the extent to which the varying ligands penetrate into the perovskite; thereby, providing helpful guidelines for the design of surface ligands.

# CHAPTER 2. EXPERIMENTAL TECHNIQUES AND DEVICE OPTIMIZATION

## 2.1 Materials and perovskite thin film fabrication

The materials used for perovskite device processing is particularly important because even small amounts of impurities can have a significant effect on the device performance. Especially for perovskite thin film fabrication, the purity of the chemical, solvents, and environment, such as vapor of solvents around, temperature, and humidity are all important factors to make good quality films. It is hard to keep the exact identical environment for the device fabrication and this relatively sensitive system brings reproducibility issues. Researchers in the community are aware of these problems and there are significant efforts to understand the relation between atmosphere and the device performance.

The most popular form of halide perovskite is fabricated by mixing organic precursor methylammonium iodide (MAI) and inorganic precursor lead iodide ($PbI_2$) to form methylammonium iodide ($MAPbI_3$).

$$CH_3NH_3I + PbI_2 \rightarrow CH_3NH_3PbI_3$$

There are two major perovskite thin film fabrication techniques. The first one is solution processed spin coating method, which can be divided to one-step and two-step spin coating. Perovskite precursor solution was usually stirred over 1 h at room temperature before use. In this process, MAI and $PbI_2$ are both dissolved in an organic solvent like dimethyl formamide (DMF), and/or dimethyl sulfoxide (DMSO). After spin coating, the substrate is placed directly on an already heated hot plate and annealed for 10 minutes at 100 °C to induce crystallization of the perovskite. In two-step spin coating, $PbI_2$ solution

is coated first and then separate MAI solution is coated on top sequentially. The second film fabrication method is a vapor process. Both organic source of MAI and inorganic source of $PbI_2$ are thermally deposited in the thermal evaporator at the same time with a constant rate.

Perovskite thin film is usually fabricated in the nitrogen filled glovebox as it degrades under the presence of moisture. Figure 2.1 shows the degradation process of $MAPbI_3$ film under 150 °C heating and 50% humidity from black phase of $MAPbI_3$ to yellow phase of $PbI_2$. HPs also show self-degradation in an inert environment as well due to the ionic bonding character of the perovskite material. Chen et al. have shown partial substitution of MA cation with dimethylammonium (DMA) can inhibit the ion migration and enhance the moisture stability.[21] Encapsulation of the device showed promising result to eliminate the effect of moisture and enhanced moisture stability.[22,23]


Figure 2.1 Pictures of $MAPbI_3$ sample degradation process under 150 °C heating

Generally, solvents were purchased from Sigma-Aldrich or Alfa Aeser anhydrous grade and used without further purification and chemicals were used with high purity grade as well >98%. Vapor deposited materials including charge transporting layer and top metal electrodes were fabricated in the thermal evaporator at a pressure of ca. $1 \times 10^{-7}$ mbar. Indium tin oxide (ITO) substrates were purchased from Tinwell Tech and the sheet

resistance was around 15 Ω/□. Pre-patterned ITO substrate was used for PV device fabrication and non-patterned ITO was selected for characterization usage.

ITO substrates were cleaned with a sodium dodecyl sulfate (SDS) solution, deionized water, acetone, and isopropanol for 10 minutes each sequentially by the sonication. After isopropanol cleaning, substrates were removed from solution and blown with nitrogen to remove the residual solvents. The substrates were then exposed to UV-ozone treatment for 10 minutes to remove organic contaminants. The cleaning process was kept as similar as possible for each device set.

Perovskite thin film spin coating was conducted with two different atmospheres even though precursor solution was always prepared in the nitrogen filled glovebox (<0.1 ppm $O_2$ and $H_2O$). For ambient environment processing, already 1 h stirred precursor was taken out from the glovebox and transferred to the fume hood for further spin coating process. The humidity was around 45±5% for summer and 20±5% for the winter. However, the other fabrication method was conducted in the nitrogen filled glovebox. Prior to using the glovebox, 20 minutes of nitrogen purging was performed to remove unwanted solvent vapors and bring down the oxygen and water level to the desired point.

## 2.2 Device architecture

Generally, for a typical PSC, active perovskite absorber layer is sandwiched between two charge transporting layers and a cathode and anode. When the device is illuminated with sun, this light will pass through transparent conductive oxide (TCO) such as ITO, and fluorine-doped tin oxide (FTO). According to the charge flow direction, the PSC device architecture can be categorized as one of two types. One type is the n-i-p

conventional structure, in which ETL is deposited on TCO and HTL is deposited on light absorber layer. The other type is the p-i-n inverted structure, where HTL is located on TCO and ETL is deposited on perovskite layer as shown in Figure 2.2.

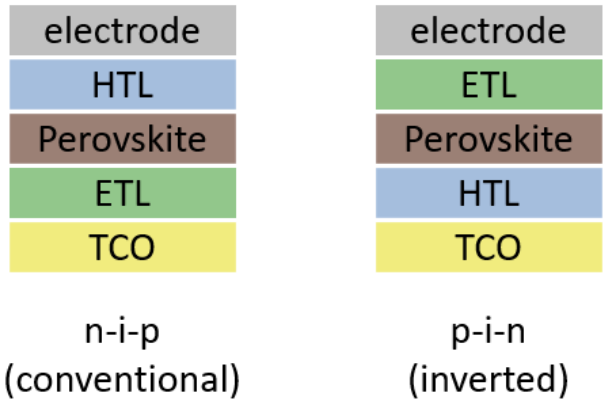


Figure 2.2 Schematic of two typical layered perovskite device architectures

In conventional device architecture, planar and/or mesoporous layer is used as ETL to facilitate efficient electron collection and transport. In the early generation of the PSC device, titanium dioxide ($TiO_2$)-based ETL was commonly applied. The high PCEs were obtained especially with mesoporous $TiO_2$ layer by providing larger contact area between the ETL and perovskite active layer which can allow for more efficient charge transfer. The reduced hysteresis was reported in 2014 with mesoporous structure which often occurs in the planar configuration of the device.[24] More recently, zinc oxide (ZnO)[25,26] or tin oxide ($SnO_2$)[27,28] was also applied for ETL due to their efficient charge transport ability from well-aligned EA of ETL and CBM of perovskite layer, high optical transparency, and stability in ambient air.

The last part of the device is the top metal electrode that collects the charge. This metal electrode layer requires good conductivity, good charge extraction ability, and proper energy level alignment with neighboring layers. For example, gold (Au), aluminum (Al), silver (Ag), or copper (Cu) are standard metal top electrodes because of their suitable work function in PSC.

## 2.3 Device optimization

As mentioned previously in the challenges of the perovskite device fabrication section, it takes a lot of effort to obtain uniform film morphologies and efficient working devices. This requires not only the detailed experimental techniques but also the reproducible environment as much as possible, such as temperature, humidity, solvent vapor residue in the air, pressure, and treatment time needs to be controlled precisely. It has been reported some amount of water in the precursor helps to form a dense perovskite crystal.[29,30] Wu group introduced post $H_2O$ treatment that can be used to enlarge the perovskite grains, which results in improved reproducibility, less hysteresis, and enhanced PV performance.[31] Furthermore, purity of the chemical is important to determine the quality of the film. Johnston group monitored the impurities of MAI after synthesis since chemical impurities can vary batch to batch showing proton Nuclear Magnetic Resonance ($^1$H NMR) peak shift due to rich in $MAH_2PO_3$, thus they suggested controlled vapor deposition technique.[32] Solvent selection should be considered carefully as they can participate in the perovskite crystal formation as intermediate phase,[33,34] and converted into a uniform and pin-hole free perovskite film.

## 2.4 Measurement techniques

### 2.4.1 Photoelectron spectroscopy (PES)

X-ray photoelectron spectroscopy (XPS) is a surface sensitive technique used to characterize the surface composition, including surface stoichiometry and the various oxidation and binding states present in the sample.

The probing depth of XPS is 1 to 10 nm, depending on the sample and electron take-off angle. XPS is initiated by irradiating the sample with a high-energy X-ray source, generally 1253.6 eV for Mg Kα and 1486.6 eV for Al Kα emission. After irradiating the sample, high energy electrons will be ejected with the kinetic energy (*KE*) equal to the difference between the X-ray source ($h\nu_{Xray}$) and the binding energy (*BE*) of the electron as shown in equation (4).

$$KE = h\nu_{Xray} - BE - \Phi \quad (4)$$

XPS is a powerful measurement technique because it gives information on the elements in the sample and their bonding state. The strength of the XPS technique comes from probing core level electrons, the energies of which depend on the specific element and the bonding state of that element. The shift of binding energy allows us to determine the bonding state of an analyzed element. In case of carbon, C-C (284.8 eV), C-O-C (~286 eV), O-C=O (~288.5 eV), and C-F (~292 eV) all show different values even though they are all for the C 1s electron.

XPS analysis was performed with a PHI 5600 system equipped with a hemispherical electron energy analyzer. The substrate was normally angled at 45° relative to normal of the sample and the detector. For angle dependent measurement, three different

electron take-off angles were measured, 0°, 45°, and 75° by rotating the sample stage to vary the probing depth. Because the mean free paths of photoelectrons are typically 2−4 nm at kinetic energies near 1000 eV, the probing depth is varied from approximately 6−8 nm at 0° to only 1.5−2 nm at 75°.

Ultraviolet photoelectron spectroscopy (UPS) is a surface analysis technique that examines the energy of valence electronic states and work functions of materials. Photon energies of UPS are typically 10 – 45 eV to excite the electrons located in the outer shell in the valence orbitals. Similarly, UPS is based on the photoelectric effect, as is XPS, in which an incident photon with energy (*hv)* generates a free electron with kinetic energy (*KE*) shown in equation (5).

$$KE = h\nu_{UV} - BE - \Phi \quad (5)$$

$\Phi$ is the work function (WF) of the material and *BE* is the binding energy of the electrons within the solid. In most laboratories, He discharge lamp is commonly selected for UPS light source such as He Iα at 58.43 nm (21.22 eV) and He IIα at 30.38 nm (40.81 eV). However, the background emission from these high energy sources limits the analysis of band edges such as defect states and tail states of the material and they have shown significant sample degradation under irradiation on organic materials. In our system a H Lyman-α lamp with 10.2 eV photon energy is used as the excitation source.[35]

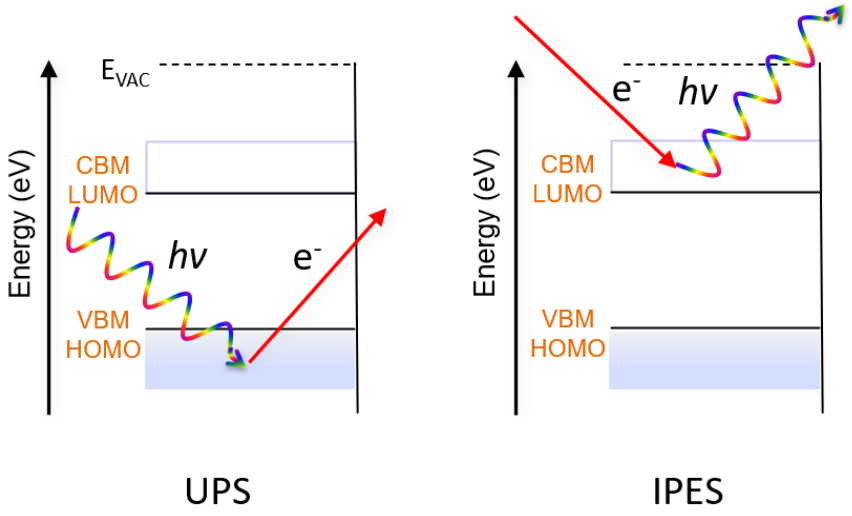


Figure 2.3 Energy schematics of UPS and IPES

Inverse photoelectron spectroscopy (IPES) is a technique that measures the unoccupied orbitals or conduction band of solid materials. IPES is the inverse of UPS and XPS measurements, electrons are injected with an electron gun into unoccupied orbitals and photons are emitted and analyzed in this technique. In our system a low energy IPES system was designed that employs low energy electrons to generate photons in the near-ultraviolet range (NUV, 200-400 nm) with electron kinetic energies below 5 eV to minimize sample degradation. Emitted photons were collected with a bandpass photon detector consisting of an optical bandpass filter (254 nm wavelength) and a photomultiplier tube. All photoelectron spectroscopy (PES) measurements including XPS, UPS, and IPES were performed in a PHI 5600 ultra-high vacuum (UHV) system at a pressure around $5\times10^{-10}$ mbar.

### 2.4.2 Morphology characterization

Due to the sensitivity of perovskite-based film fabrication, high quality films with controlled uniform morphology, high surface coverage, and minimum pinholes are key requirements to obtain high performance of the device.

Scanning electron microscopy (SEM) is a measurement in which images of a sample are produced by scanning the surface with a focused beam of electrons. SEM is one of the most versatile instruments that is available for the analysis of the sample morphology. The electron beam acceleration takes place through the high voltage system (2 - 20 kV), and secondary and backscattered electrons are used to produce an image. The SEM images allow us to determine the different particle shapes, surface morphology, and size distributions from micro ($10^{-6}$) to nano ($10^{-9}$) meter scales. The images presented in this dissertation are generally from a Hitachi S-4300 SEM with an accelerating voltage of 10 kV. This instrument can be used in conjunction with other related techniques of energy-dispersive X-ray spectroscopy (EDX) for the determination of the chemical compositions.

### 2.4.3 Crystal structure characterization

X-ray diffraction (XRD) measurement are based on the ability of crystals to diffract X-rays allowing a precise study of the structure of crystalline phases. XRD is widely used in material research to identify crystal structure, phase, orientation, crystallinity, and defects. XRD patterns are presented by constructive interference of a monochromatic beam of X-rays diffracted at the specific angles from each set of lattice planes in a sample. XRD is based on Bragg's law as follows in equation (X).

$$n\lambda = 2dsin\theta \qquad \text{(X)}$$

From peak position, shift, intensity, broadening, and FWHM, you can get information about the crystal structure. In here, XRD spectra were collected with a Bruker-AXS D8 advance diffractometer with Cu Kα radiation (λ = 1.5418 Å) operating at 40 kV and 40 mA.

# CHAPTER 3. EFFECTS OF HOLE TRANSPORT LAYER IONIZATION ENERGY ON PEROVSKITE PVS



## 3.1 Summary

Perovskite solar cells (PSCs) typically contain both electron and hole transport layers, both of which influence charge extraction and recombination. The ionization energy (IE) of the hole transport layer (HTL) is one important material property that will influence the open-circuit voltage, fill factor, and short-circuit current. Herein, we introduce a new series of triarylaminoethynylsilanes with adjustable IEs as efficient HTL materials for methylammonium lead iodide ($MAPbI_3$) perovskite-based photovoltaics. The three triarylaminoethynylsilanes investigated can all be used as HTLs to yield PV performance on par with the commonly used HTLs PEDOT:PSS and Spiro-OMeTAD in inverted architectures (i.e., HTL deposited prior to the perovskite layer). We further investigate the influence of the HTL IE on the photovoltaic performance of $MAPbI_3$ based inverted devices using two different $MAPbI_3$ processing methods with a series of 11 different HTL materials, with IEs ranging from 4.74 to 5.84 eV. The requirements for the HTL IE change based on whether $MAPbI_3$ is formed from lead acetate, $Pb(OAc)_2$, or $PbI_2$ as the Pb source. The ideal HTL IE range is between 4.8 and 5.3 eV for $MAPbI_3$ processed from $Pb(OAc)_2$,

while with $PbI_2$ the PV performance is relatively insensitive to variations in the HTL IE between 4.8 and 5.8 eV. Our results suggest that contradictory findings in the literature on the effect of the HTL IE in perovskite photovoltaics stem partly from the different processing methods employed.

## 3.2 Introduction

Organometal and metal halide perovskites have rapidly emerged as the most competitive third-generation PV technology, with record PCEs of lead based perovskites increasing from 3.8% in 2009 to 22% in 2017.[1,36,37] With these high PCEs, perovskite PVs are of increasing interest for commercialization. This push for commercialization and the development of alternative perovskites, e.g., lead-free perovskites, requires the generation of robust PV cell architectures and materials that can be processed using inexpensive solution based methods with inexpensive and stable materials for every component of the device. One important aspect in meeting the demands for the further development of perovskite PVs is the development of solution processable, stable, easily prepared charge transport layers that yield high-performing PV devices. Targeted design of these transport layers requires an understanding of the properties necessary to yield such PVs.

The most efficient perovskite PV cells to date, based either on methylammonium lead iodide ($MAPbI_3$) or similar perovskites (e.g., formamidinium lead iodide), rely on the use of both hole and electron transport layers.[36–38] These transport layers typically result in selective extraction of holes or electrons at the appropriate electrodes. Modifications to various properties of these transport layers are predicted to lead to improved PV device performance and are currently a subject of research interest. These transport layer

modifications include enhancing the ability of the transport layer to passivate interfacial defect states in the perovskites,[39,40] optimizing the energy level alignment between transport states in the perovskite and charge transport layer,[41,42] enhancing the charge carrier mobility or electronic conductivity of the transport layer,[43–45] and increasing the stability of the layer under PV cell operating conditions.[46–48]

The majority of hole transport layers (HTLs) are based on organic materials,[4243474950] with PEDOT:PSS and Spiro-OMeTAD being the most widely used, but inorganic layers such as $NiO_x$ have also demonstrated high performance.[51,52] All the commonly used HTLs have their drawbacks. For example, PEDOT:PSS and Spiro-OMeTAD can lead to unstable PV cells and many of the organic HTLs are expensive due to complicated synthetic routes or intensive purification procedures.[53–55] Furthermore, optimizing the electronic properties of the HTL is likely to lead to higher PV performance, further motivating the need to develop new HTLs. A wide range of these materials are being investigated, including small molecules such as triarylamine derivatives, carbazole derivatives, and porphyrins[56–60] and polymers such as polytriarlyamines and polyelectrolytes.[61–65] More extensive reviews of HTLs can be found in the literature.[50,66]

One parameter of the HTL that is predicted to affect the performance of $MAPbI_3$ based PV cells is the ionization energy (IE). For example, if the IE of the HTL is significantly higher than the IE of $MAPbI_3$, then a barrier to hole transfer from the perovskite to HTL may exist. Alternatively, if the IE of the HTL is significantly lower than the IE of the active layer, then the achievable open-circuit voltage ($V_{OC}$) of the PV cell may be reduced due to a pinning of the quasi-Fermi level of holes to the HTL HOMO energy. A recent literature review, which compiles results from over 50 HTL materials

used in $MAPbI_3$ PV cells, shows that efficient PV devices are generally obtained when the IE or HOMO of the HTL is between 5.0 and 5.35 eV. These results are consistent with work by Belisle, et al. and Ishida, et al. where HTLs with varying IEs were examined.[67,68] In these reports high PV performance was observed with HTL IEs between 5.0 and 5.35 eV, and significant performance drops were observed when the IE exceeded 5.4 eV. Other reports suggest a narrower range of IEs is acceptable.[41,42,69,70] For example, Polander et al. show that perovskite PV performance drops when the HTL IE is lower than 5.1 eV or higher than 5.3 eV,[41] Cho et al. show a drop in PV performance as the IE changes from 5.19 to 5.32 eV,[42] and Rakstys et al. show higher PV performance for HTLs with IEs of 5.22 and 5.14 than for IEs of 5.09 and 4.96.[70] The different reported acceptable HTL IE ranges found in the literature may arise due to variations in $MAPbI_3$ processing methods, different device architectures, different techniques for measuring IEs or HOMO energies (e.g., photoelectron spectroscopy or electrochemistry), differences in the perovskite layer, or other factors (such as the charge-carrier mobility) of the HTL that may influence PV performance.

In this work we introduce a novel family of triarylaminoethynylsilyl (TAAES) derivatives as HTL materials for perovskite PVs and investigate the influence of the HTL IE, as measured with ultraviolet photoelectron spectroscopy (UPS), on the performance of $MAPbI_3$-based PV cells. We expand our investigation of HTL materials from the TAAES derivatives to a variety of HTL materials with IEs spanning a 1.1 eV range. We find that the $V_{OC}$ is surprisingly high for HTL IEs down to 4.74 eV, and with $Pb(OAc)_2$ as the source of lead the PCE values are maximized for HTL IEs of 4.8 to 5.3 eV due primarily to changes in the fill factor (FF) and short-circuit current density ($J_{SC}$). With a different

processing procedure using $PbI_2$ as the source of lead the PCE is less sensitive to HTL IE, with champion PCEs over 10% for a nearly 1 eV range in the HTL IE.

## 3.3 Experimental section

### 3.3.1 Materials

Lead acetate trihydrate ($Pb(OAc)_2 \cdot 3H_2O$, 99.0-103.0%) and lead iodide ($PbI_2$, 99.9985%) were purchased from Alfa Aesar. Methylammonium bromide (MABr) was purchased from Lumtec. Methylammonium iodide (MAI) was bought from Dyesol and used after recrystallizing twice in ethanol and drying in a vacuum oven overnight at 60 ºC. N,N-dimethylformamide (anhydrous, 99.8%), dimethylsulfoxide (anhydrous, 99.8%), and ethyl ether (anhydrous, 99.0%) were purchased from EMD Millipore Corp. Chlorobenzene (anhydrous, 99.8%) was bought from Sigma-Aldrich. Hole transport materials include Spiro-OMeTAD (Jilin OLED), rubrene (TCI, >99.9%), α-sexithiophene (6T, TCI), N,N′-di(1-naphthyl)-N,N′-diphenyl-(1,1′-biphenyl)-4,4′-diamine (NPD, Sigma-Aldrich, 99%), and tris-(8-hydroxyquinoline)aluminum ($Alq_3$, TCI, 98%) .The electron transporting layers and electrodes include [6,6]-phenyl C61-butyric acid methyl ester ($PC_{61}BM$, Nano-C), $C_{60}$ (Nano-C, 99.5%), 2,9-dimethyl-4,7-diphenyl-1,10-phenanthroline (BCP, TCI, >99.0%), Al (99.99%, Angstrom Engineering), Ag (99.99%, Angstrom Engineering), and $MoO_3$ (Alfa Aesar, 99.998%).

Synthesis and purification of methylammonium iodide: Methylamine (27.8 mL, 40 wt%, Alfa Aesar) and hydriodic acid (30 mL, 57 wt%, Alfa Aesar) were combined and allowed to react in an ice bath for 2 h with stirring. The solution was then evaporated at 60 ºC with a rotary evaporator, leaving only methylammonium iodide (MAI). The precipitate

was washed with diethyl ether several times until the color of precipitate was white. The obtained precipitate was dried under vacuum for 24 h and stored in a nitrogen-filled glove box (<0.3 ppm $H_2O$ and $O_2$) until use. Both house synthesized MAI and recrystallized MAI from Dyesol showed similar performance in photovoltaic devices.

### 3.3.2 Materials characterization

X-ray diffraction data were collected for the TAAES crystals using either a NoniusKappa CCD (Mo Kα) or a Bruker X8 Proteum (Cu Kα) diffractometer. UV−vis absorbance measurements were recorded on thin films in a nitrogen-filled glovebox using an Ocean Optics fiber-optic spectrometer with a thermoelectric cooled CCD detector coupled with an integrating sphere. Films for UV−vis measurements were prepared on clean glass slides. Thin films for ultraviolet photoelectron spectroscopy (UPS) were prepared with thicknesses of 15−25 nm for the HTLs and ca. 200 nm for the perovskite by thermal evaporation or spin-coating on nonpatterned ITO-coated glass substrates (Tinwell Tech., 15 Ω/□), using similar procedures as those reported for the PV device fabrication. Devices for SCLC measurements were fabricated with the structure ITO/PEDOT:PSS/HTL/$MoO_3$/Ag. Prior to spincasting the HTL, ITO-coated glass substrates were cleaned and coated with PEDOT:PSS as detailed in the PV Device Fabrication section. Films of the TAAES derivatives (30 mg/mL in chlorobenzene) were prepared by spin-casting at 4000 rpm for 30 s in the nitrogen-filled glovebox without further annealing. $MoO_3$ (7 nm) and Ag (100 nm) were thermally evaporated through shadow masks to define 8 independently addressable pixels per substrate. Differential scanning calorimetry (DSC) measurements were measured with a TA Instruments Q20,

with a heating ramp of 20 °C/min rate under a nitrogen atmosphere. UPS measurements were taken with an Excitech H Lyman-α photon source (10.2 eV) coupled with a PHI 5600 ultrahigh vacuum system with a hemispherical electron energy analyzer, as detailed in our previous publication.[35] A sample bias of −5 V and a pass energy of 5.85 eV were used for the UPS measurements. Uncertainties in IEs are typically ±0.05 eV based on sample-to-sample and spot-to-spot variation. X-ray photoelectron spectroscopy (XPS) measurements were performed with the same PHI 5600 system and analyzer using a Mg Kα source (1253.6 eV, PHI 04-548 dual anode X-ray source) for excitation and a pass energy of 23.5 eV. The samples for HTL and ITO reactivity studies using XPS were prepared by depositing the HTL on ITO, as detailed in the PV Device Fabrication section, probing the HTL with XPS, depositing the perovskite (as detailed in the PV device fabrication section) onto the HTL or ITO, and rinsing the perovskite off with dimethylformamide. Following perovskite removal, the HTL or ITO was again probed with XPS. Samples for scanning electron microscopy (SEM) were prepared on ITO-coated glass and probed with a Hitachi S-4300 SEM with an accelerating voltage of 2 or 10 kV.

PV device fabrication and characterization: Patterned ITO-coated glass substrates (Tinwell Tech., 15 Ω/□) were sequentially sonicated in aqueous detergent (sodium dodecyl sulfate, Sigma-Aldrich), deionized water, acetone, and 2-propanol each for 10 min. After drying with nitrogen the substrates were exposed to UV-ozone treatment for 10 min to remove organic contaminants. PEDOT:PSS (Clevios P VP AI 4083) was spun cast at 5000 rpm for 30 s and then annealed on a hotplate at 130 ºC for 15 min in air. Rubrene, NPD, 6T, H-ADT, Cl-ADT, and $Alq_3$ (25 nm) were deposited by thermal evaporation to a thickness of 25 nm with rates of 0.5 or 1 Å/s at a typical pressure of 1 x $10^{-7}$ mbar. Spiro-

OMeTAD and the TAAES derivatives (30 mg/mL chlorobenzene) were spun cast at 4000 rpm for 30s and annealed at 70 ºC for 5 min. With the exception of PEDOT:PSS, all HTLs were prepared inside a $N_2$-purged glove box (<0.1 ppm $O_2$ and $H_2O$). All further processing was also done in this glovebox for the $Pb(OAc)_2$ procedure, whereas in the $PbI_2$ procedure the perovskite films were cast in air.

$Pb(OAc)_2$ based $MAPbI_3$ preparation: MAI and $Pb(OAc)_2{\cdot}3H_2O$ were dissolved in anhydrous DMF at 3:1 molar ratio. The final concentration of solution was 46 wt% before adding 1 mol% MABr to $Pb(OAc)_2{\cdot}3H_2O$ in DMF. This solution was spun cast at 4000 rpm for 30 s on top of the different HTLs and then allowed to dry for 15 s. During this 15 s delay the perovskite film started to change from transparent to light brown. Then, the substrates were put on a hotplate at 70 ºC for 10 min. Substrate appearance changed rapidly to a mirror-like dark brown upon putting on the hotplate. The $MAPbI_3$ film on Cl-ADT was inhomogeneous, resulting in few working cells. To improve $MAPbI_3$ film formation, 80 µL of 1-butanol was dripped on the Cl-ADT coated substrate and spun cast at 4000 rpm for 30 s immediately before coating the perovskite layer. The yield of working devices improved significantly with 1-butanol, but the PV performance with and without 1-butanol was similar.

$PbI_2$ based $MAPbI_3$ preparation: For the perovskites processed using a $PbI_2$ precursor solution, 461 mg of $PbI_2$, 159 mg of MAI, and 78 mg of DMSO (1:1:1 molar ratio) were added to 600 mg of DMF solution and stirred at room temperature for 1 h before use in the glovebox. This solution and the HTL coated substrates were transferred from the glovebox to a fume hood in ambient atmosphere (humidity 47±3%) immediately prior to spin coating. The perovskite precursor solution was spun cast at 4000 rpm for 25 s with a

2 s ramp and 0.5 mL of diethyl ether was rapidly injected onto the substrate 5 s into the spin coating process. Immediately following spin coating the substrates were heated at 65 ºC for 1 min and 100 ºC for 5 min. After annealing the films were brought back into the nitrogen-filled glovebox for further processing.

$PC_{61}BM$ (20 mg/mL chlorobenzene) was spun cast on top of the perovskite thin films at 4000 rpm for 30 s. The films were transferred to the thermal evaporator without air exposure and $C_{60}$ (20 nm) and BCP (10 nm) were deposited sequentially with a rate of 1 Å/s at a pressure of ca. $1 \times 10^{-7}$ mbar. Finally, aluminum (100 nm) electrodes were evaporated through a shadow mask that defined 4 cells of 0.1 $cm^2$ area and 4 cells of 0.2 $cm^2$ area per substrate. Solar cell performance was measured using a solar simulator (ABET technologies, 11002) at 100 $mW/cm^2$ illumination (AM 1.5G). The intensity was adjusted to (100 $mW/cm^2$) using a photodiode calibrated with a KG5 filter (ABET technologies). The PV cell data reported is typically an average of 16 or more cells, with error bars representing ±1 standard deviation.

## 3.4 Results and discussions

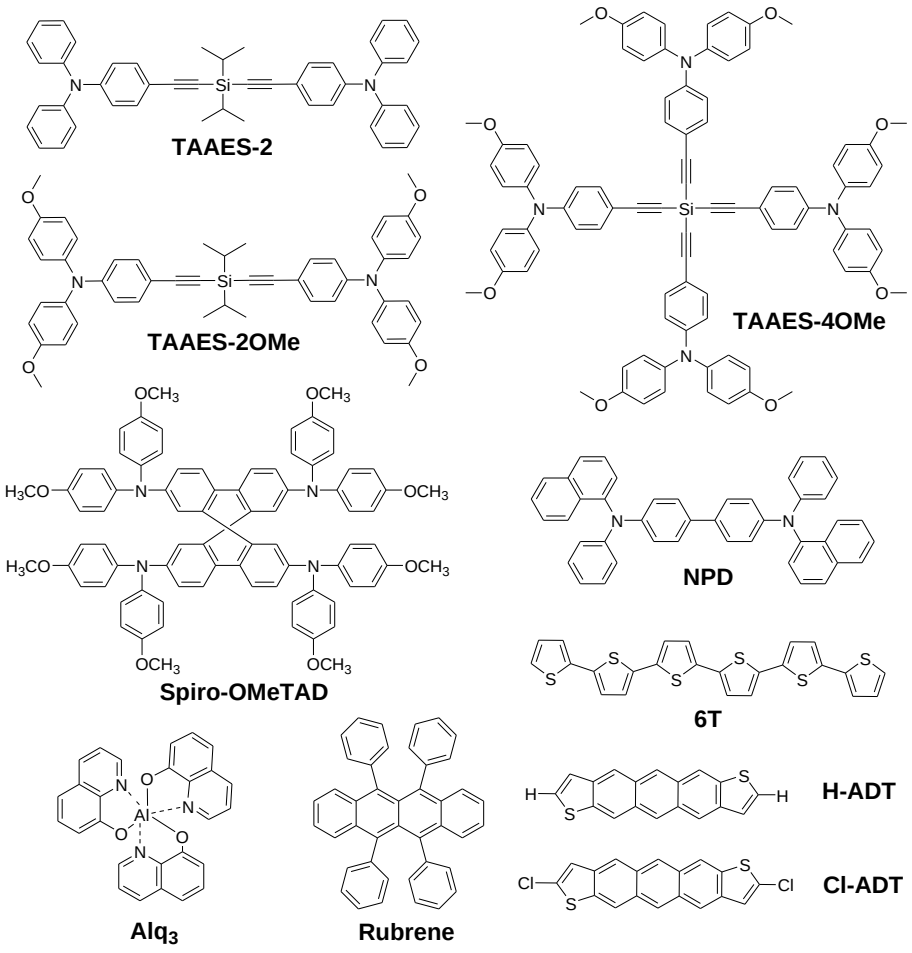


Figure 3.1 Chemical structures of the molecules utilized as HTLs in this work

The molecular structures of the HTLs utilized in this work are depicted in Figure 3.1. These molecules include the solution processed TAAES derivatives, the commonly used PEDOT:PSS (not shown) and Spiro-OMeTAD materials, and a series of thermally evaporated small organic molecules that were selected to span a wide range of IEs. Within these materials, there are multiple sets that show similar structural characteristics and thus are more directly comparable. These include the TAAES family, where the IE is varied by introducing methoxy groups on the phenyl rings and increasing the number of triarylamine

groups bound to the central silicon atom. In part, this TAAES family was inspired by dimeric versions of ethynyl triarylamines, which show reasonable efficiencies when used as hole transport layers in dye sensitized PVs.[71] By building off of a tetrahedral silane-based scaffolding, we are able to vary both the solubility and geometry of the HTL material by simple chemistry. The ADT derivatives are also structurally similar molecules with widely differing IEs. Here, substitution of the reactive thiophene ends with chlorines is used to alter the IE.

The UV-Vis absorbance measurements for thin films of these TAAES derivatives, as shown in Figure 3.2, show that these derivatives absorb at wavelengths shorter than *ca*. 400 nm, thus allowing most visible light to be absorbed by $MAPbI_3$ in the PV cells.

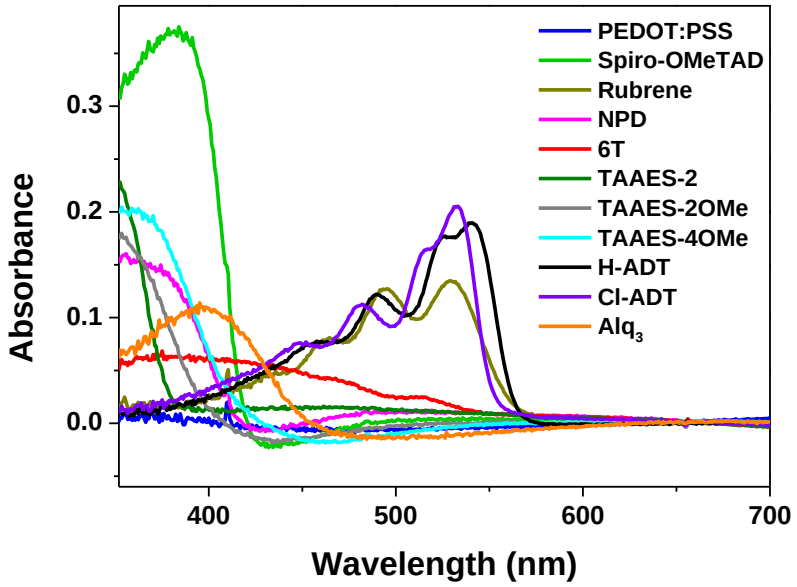


Figure 3.2 UV-Vis absorbance measurements for thin films of the HTLs. Thicknesses are indicated in parenthesis. PEDOT:PSS (35 nm), Spiro-OMeTAD (35 nm), TAAES-2 (25 nm), TAAES-2OMe (35 nm), and TAAES-4OMe (35 nm); and the vapor deposited HTLs 6T, rubrene, NPD, $Alq_3$, H-ADT and Cl-ADT are all at 25 nm thickness. The measurements were recorded with a CCD based spectrometer using an integrating sphere and the dip in absorbance for some materials following their absorbance band is due to photoluminescence

### 3.4.1 Ultraviolet photoelectron spectroscopy

Films of the $MAPbI_3$ perovskite and varying HTLs were prepared on ITO coated glass substrates using two different processing methods and examined with UPS to determine the work functions (WFs) and IEs. Reported IEs (or valence band maxima energies) for $MAPbI_3$ measured with UPS range from 5.2 to 6.6 eV.[72–79] This massive variation in reported values may stem from the sample preparation method, an excess of Pb or MAI, underlying substrate work function, sample damage during measurement, and the method used to define the IE. Endres, et al. combined DFT calculations with UPS data and suggested that the most appropriate way to define the IE (or valence band position) of

$MAPbI_3$ is based on the valence band onset as determined from a semi-log plot.[75] Using a linear fit to the VB edge on a semi-log plot we measure an IE of 5.80±0.07 eV for $MAPbI_3$ processed using $Pb(OAc)_2$ and 5.56±0.06 eV for $MAPbI_3$ processed using $PbI_2$, as shown in Figure 3.3. These IE values are averages (± standard deviations) from three or four separately prepared films for each processing method, with all measured IE values and work functions listed beneath Figure 3.3.

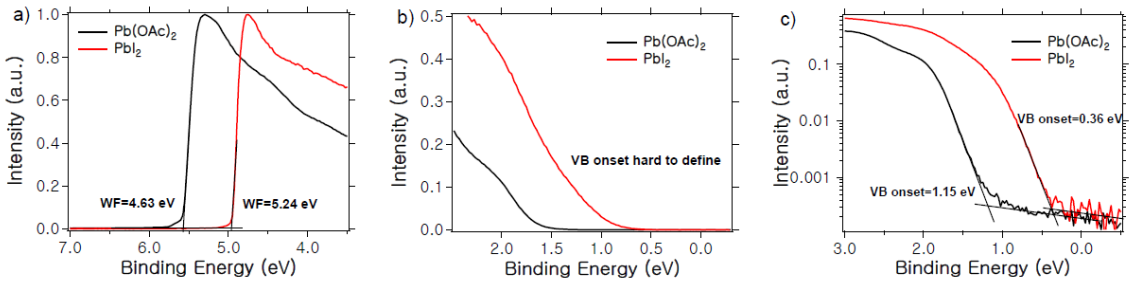


Figure 3.3 UPS spectra of $MAPbI_3$ showing the secondary electron cut-off region (a) and the valence band onset region plotted on a linear (b) and logarithmic (c) scale for $MAPbI_3$ films processed from $Pb(OAc)_2$ and $PbI_2$. The IE (work function) values measured for separate $MAPbI_3$ films processed from $Pb(OAc)_2$ were 5.88 (4.66), 5.78 (4.63), and 5.75 (4.42) eV, while separate $MAPbI_3$ films processed from $PbI_2$ yielded IE (work function) values of 5.61 (5.26), 5.53 (5.10), 5.60 (5.07), and 5.49 (4.99) eV

Ultraviolet photoelectron spectra measured for the various HTLs are shown in Figure 3.4. The photon source for the UPS measurements emits from the H Lyman-α transition at 10.2 eV and we previously demonstrated that this lower energy source reduces sample damage.[35] Here, the intersection of a tangent to either the final 50% of the secondary electron cut-off edge or HOMO edge and the background is used to extract the work function (WF) and HOMO onset, respectively. The IEs are calculated by adding the difference between the HOMO onset and Fermi energy ($E_{Fermi}$ is at 0 eV) to the WF. Since

PEDOT:PSS is a highly doped material, the WF is used in place of the IE. These measured IEs are depicted schematically in Figure 3.5 along with a simplified device energy diagram.

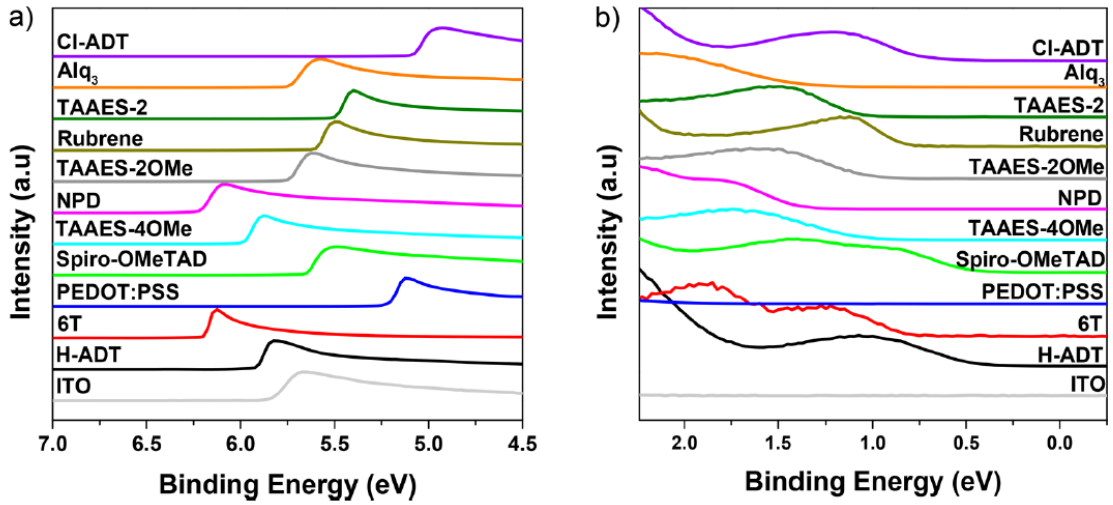


Figure 3.4 UPS spectra showing the secondary electron cut-off (a) and HOMO onset (b) regions for the HTLs applied in this work

The UPS measurements of the TAAES derivatives show IEs ranging from 5.26 to 5.76 eV. For these TAAES derivatives, the addition of methoxy groups to TAAES-2 results in a 0.34 eV decrease in the IE. This trend is explained by the π-electron donating nature of the methoxy groups, and is consistent with the 0.31 eV decrease in IE observed by Planells, et al.[71] upon adding methoxy groups to similar triarylaminoethynes. Adding two more triarylamine groups to the central silicon atom further lowers the IE by 0.16 eV to 5.26 eV, which is in the range of other HTL materials that show high performance in $MAPbI_3$ PV cells.[50] For the ADT derivatives, substitution of the two terminal hydrogens with chlorines results in a massive increase in the IE of 1.1 eV, from 4.74 eV for H-ADT to 5.84 eV for Cl-ADT. The IEs of the other materials are in agreement with previously reported values.[67,72,80–82]

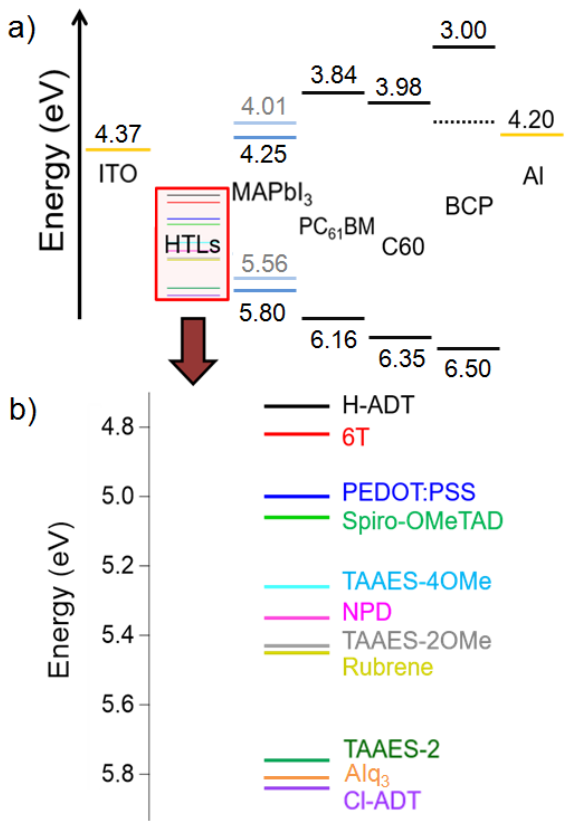


Figure 3.5 Simplified device energy level schematic showing the electrodes, HTLs, $MAPbI_3$, and ETLs (a) and the measured IEs of the various HTLs used in this work (b). The IEs, electron affinities, and/or work functions for $PC_{61}BM$, $C_{60}$, BCP, and Al are taken from the literature

### 3.4.2 TAAES derivatives as HTLs in PV devices

Photovoltaic devices were initially fabricated based on previously reported methods that use lead acetate and methylammonium iodide as precursors in a one-step perovskite film formation process,[83] as detailed in the experimental section. The TAAES derivatives and Spiro-OMeTAD layers were solution processed in a nitrogen-filled glovebox, while PEDOT:PSS was processed in air. Spiro-OMeTAD was not doped, thus permitting a more direct comparison to the other undoped HTLs investigated in this manuscript. Illuminated and dark current-voltage characteristics are displayed for the solution processed HTL layers in Figure 3.6.

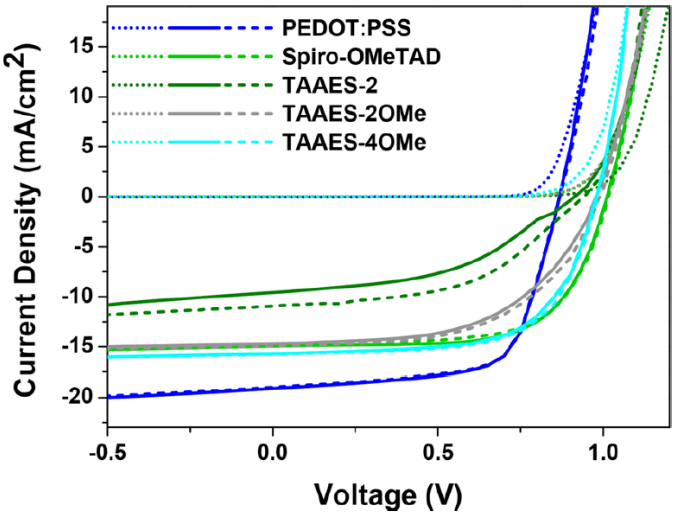


Figure 3.6 Illuminated and dark current−voltage characteristics for the solution-processed HTLs with $Pb(OAc)_2$ as the Pb source precursor. Dotted lines are in the dark, solid lines are forward scans, and dashed lines are reverse scans

The highest performing TAAES derivative is TAAES-4OMe, which shows slightly lower PV performance than PEDOT:PSS and on par performance with Spiro-OMeTAD. Here, the $V_{OC}$ of TAAES-4OMe (0.98±0.01 V) is similar to Spiro-OMeTAD (1.00±0.01 V) and greater than PEDOT:PSS (0.90±0.02 V). The HTLs all show similar fill factors of 0.62 to 0.66 and short circuit current densities ($J_{SC}$) of 15 to 18 mA/cm$^2$. As a result, the average PCEs for these three devices are 9.45±0.48, 9.50±0.51, and 10.66±0.28 % for TAAES-4OMe, Spiro-OMeTAD, and PEDOT:PSS, respectively. Additionally, there is minimal hysteresis in the J-V curves, with TAAES-4OMe and Spiro-OMeTAD showing almost none. This data indicates that TAAES-4OMe is a suitable alternative to the more commonly used Spiro-OMeTAD and PEDOT:PSS transport layers. The simple and scalable route to these TAAES derivatives, although not optimized for this report, make them attractive as lower-cost replacements for Spiro-OMeTAD. Further, the ease of synthetic tunability of both the core and periphery of these systems makes them a versatile

platform for determining structure-function relationships that govern the performance of HTL materials used in perovskite photovoltaics. Figure 3.6 shows that TAAES-2OMe and TAAES-2 exhibit lower performance than TAAES-4OMe, with PCE values of 7.83±0.34 and 4.42±0.74 %, respectively. Multiple properties of the HTL may influence the PV performance, including the IE, charge-carrier mobility,[84,85] and its influence on the morphology of the perovskite film.[62]

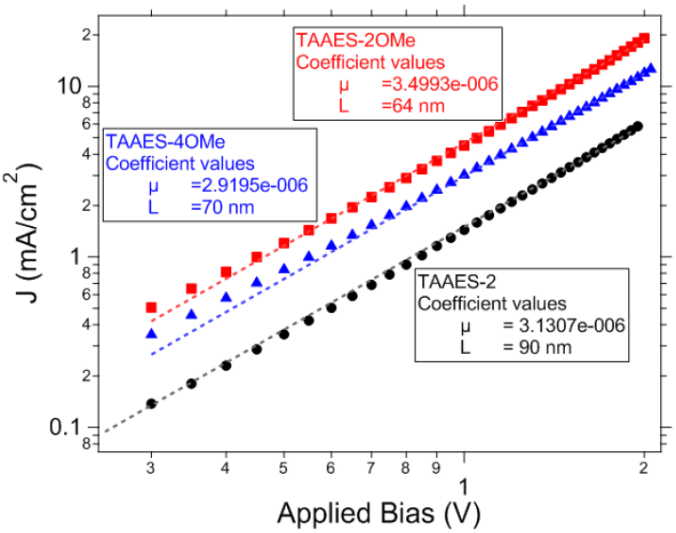


Figure 3.7 Representative J-V data for SCLC devices (filled symbols), fits to equation (6) (dashed lines), and extracted mobility values through fitting with equation (6). *L* is the film thickness and ε is the dielectric constant (ε = 3.1 × $10^{-11}$ $C^1V^{-1}m^{-1}$ through assuming a relative permittivity of 3.5 for the TAAES derivatives)

$$J = \frac{9\varepsilon\mu V^2}{8L^3} \qquad (6)$$

The hole mobilities of the TAAES derivatives were extracted from space-charge limited current (SCLC) measurements fit with the Mott-Gurney equation, as shown in Figure 3.7. These hole mobilities are all similar with average values of 4 × $10^{-6}$, 5 × $10^{-6}$, and 2 × $10^{-6}$ $cm^2V^{-1}s^{-1}$ for TAAES-2, TAAES-2OMe, and TAAES-4OMe, respectively. These similar hole mobilities suggest that the mobility of the HTL materials are not

responsible for the observed performance differences. Scanning electron microscopy images show that the $MAPbI_3$ morphologies are similar on all the TAAES derivatives, with average grain sizes falling between 108 and 119 nm, as shown in Figures 3.8 and 3.9 and Table 3.1.

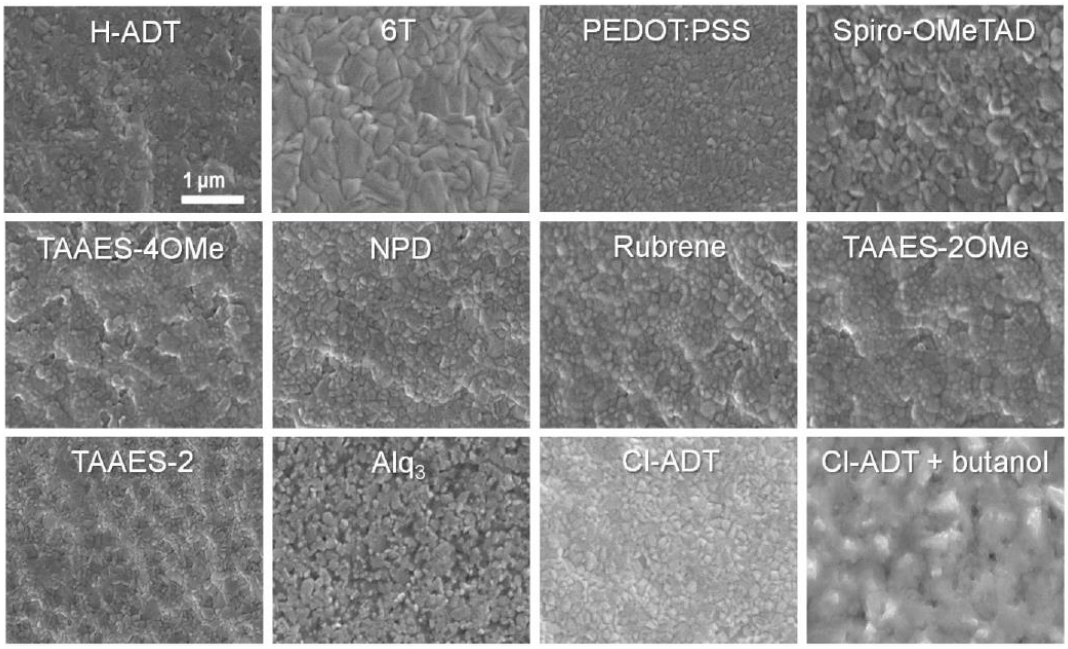


Figure 3.8 Scanning electron microscope images of $MAPbI_3$ films on the various HTLs with $Pb(OAc)_2$ lead source. All scale bars are 1 µm

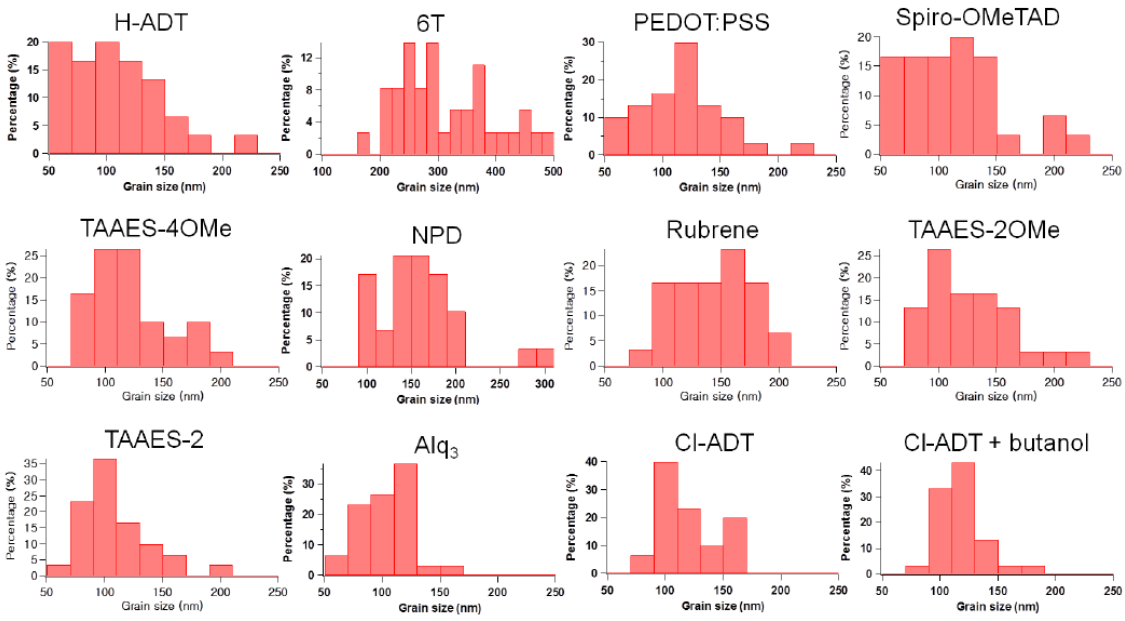


Figure 3.9 Histograms of $MAPbI_3$ films grain size on the various HTLs with $Pb(OAc)_2$ lead source

Table 3.1 Average grain size and standard deviation of $MAPbI_3$ films on the various HTLs with $Pb(OAc)_2$ lead source

| HTLs | Average grain size (nm) | Standard deviation |
|---|---|---|
| H-ADT | 107 | 35.95 |
| 6T | 314 | 82.25 |
| PEDOT:PSS | 117 | 35.42 |
| Spiro-OMeTAD | 126 | 37.15 |
| TAAES-4OMe | 119 | 32.51 |
| NPD | 158 | 47.80 |
| Rubrene | 143 | 31.17 |
| TAAES-2OMe | 112 | 42.76 |
| TAAES-2 | 108 | 30.33 |
| $Alq_3$ | 102 | 22.82 |
| Cl-ADT | 116 | 26.05 |
| Cl-ADT + butanol | 117 | 19.84 |

Furthermore, the TAAES derivatives all have glass transition temperatures ($T_g$s) of 80±2 °C, as shown by the DSC data presented in Figure 3.10. These $T_g$s are below the

annealing temperature of the $MAPbI_3$ film, and thus we do not expect significant differences in the degree of perovskite precursor diffusion within the HTLs during thermal annealing. With similar hole mobility and perovskite morphology, the most apparent difference in the measured and expected physical properties of the three TAAES derivatives is the IE, which varies from 5.26 to 5.76 eV. Neglecting changes in material energetics at the interface, TAAES-2 has an IE that is nearly identical to that of the perovskite, whereas TAAES-2OMe and TAAES-4OMe have IEs that are 0.34 and 0.50 eV lower than that of the perovskite. However, TAAES-2 shows the lowest performance. To determine whether these differences in IEs are a major reason for the variation in PV performance, we extended our HTL study to include six more materials spanning a larger range of IEs.

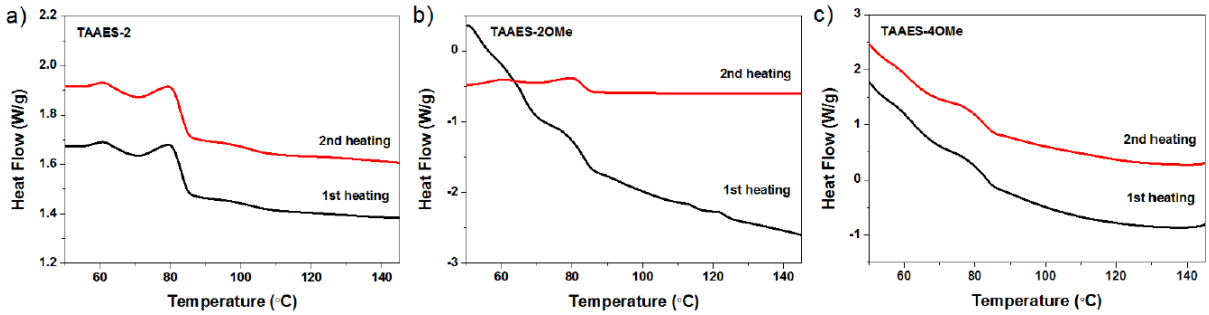


Figure 3.10 Differential scanning calorimetry data of TAAES-2 (a, $T_g$ 80 °C), TAAES-2OMe (b, $T_g$ 80 °C), and TAAES-4OMe (c, $T_g$ 78 °C)

### 3.4.3 HTL IE influence on PV performance

The additional HTL materials selected to further probe how the IE effects the PV performance of $MAPbI_3$ devices include H-ADT (IE=4.74 eV), 6T (IE=4.82 eV), NPD (IE=5.35 eV), rubrene (IE=5.44 eV), $Alq_3$ (IE=5.81 eV), and Cl-ADT (IE=5.84 eV). One

of the goals is to determine if HTLs with low IEs (i.e. 6T and H-ADT) result in $V_{OC}$ losses, as has been previously observed and suggested to account for lower $V_{OC}$ values in perovskite PVs. Another goal is to determine if HTLs with higher IEs result in $V_{OC}$, FF, or $J_{SC}$ losses due to a barrier to hole extraction.

Figure 3.11 shows the average PV performance parameters for the $MAPbI_3$ PV cells as a function of HTL IE. First, we analyse the trends with $Pb(OAc)_2$ as the Pb source. Surprisingly, the $V_{OC}$ remains high (>0.92 V) even when the HTL IE drops to 4.74 eV. The $J_{SC}$ plateaus at ca. 15 $mA/cm^2$ when the IE is between 5.06 and 5.41, but drops off as the IE ventures outside of this range. The FF stays above 0.62 with HTL IEs of 4.74 to 5.26 eV, and decreases steadily as the IE climbs above 5.26 eV. As a result, the PCE is greatest for HTL materials with IEs between 4.82 and 5.26 eV with $Pb(OAc)_2$.

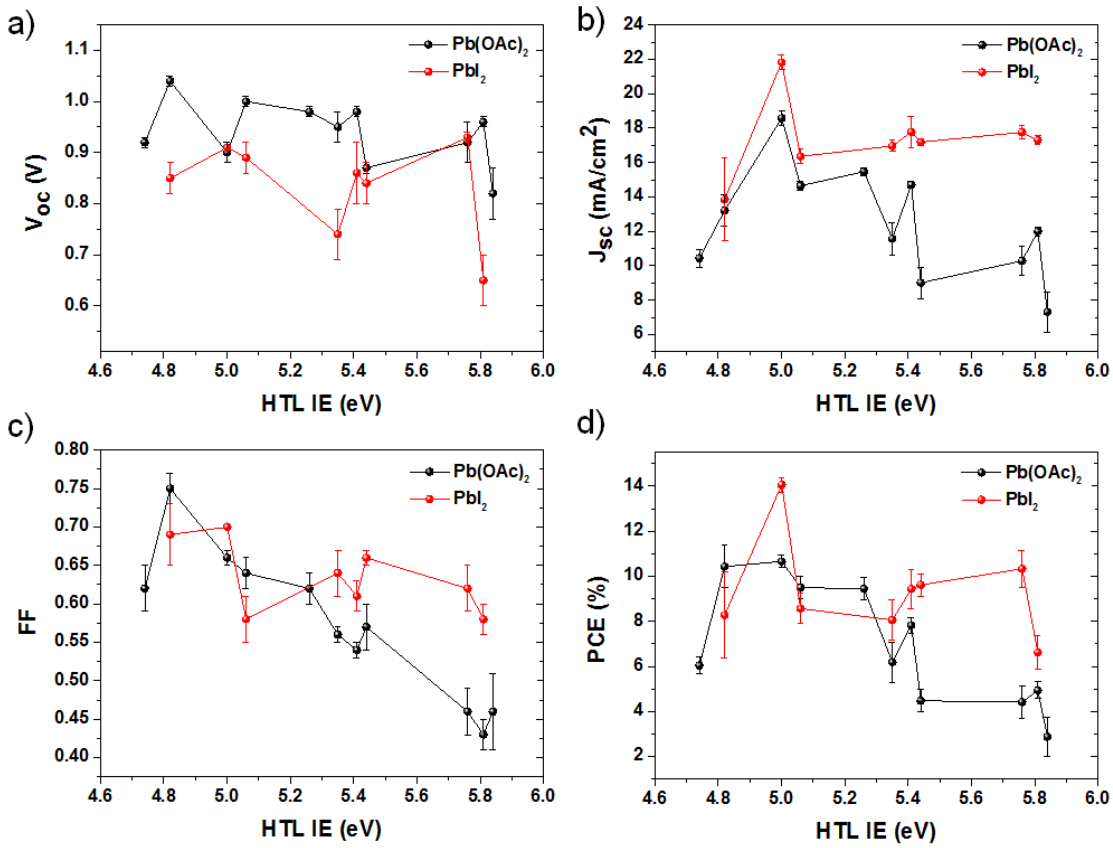


Figure 3.11 Average $V_{oc}$ (a), $J_{sc}$ (b), FF (c), and PCE (d) for $MAPbI_3$ PV cells as a function of HTL IE. The error bars correspond to ± the standard deviations from typically 16 or more individual PV cells for each HTL

To determine if these trends were generally applicable, we tested many of the HTLs using a different method to process the $MAPbI_3$ films. When the processing method is altered to include $PbI_2$ as the Pb source, as shown in Figure 3.6, the $J_{SC}$, FF, and PCE become less sensitive to the HTL IE, as indicated by champion PCEs of above 10% for HTL IEs at 4.82 and 5.76. The reduced sensitivity of the HTL IE using this $PbI_2$ processing method may potentially arise due to the dependence of the interfacial chemistry and associated energetics on the lead precursor and processing environment. Additionally, the significantly lower concentrations of MAI needed with the $PbI_2$ source (a 1:1 MAI:$PbI_2$ molar ratio, as opposed to a 3:1 MAI:$Pb(OAc)_2$ ratio) may influence material and interface

energetics. These hypotheses are in part supported by the processing method dependent IE and work function for $MAPbI_3$, as well as the IE dependence on the MAI:Pb ratio used in the precursor solution, as reported in the literature and evidenced by our UPS data in Figure 3.3.

Both $MAPbI_3$ processing methods show that the $V_{OC}$ does not correlate with the HTL IE for materials with IEs below 5.8 eV. This trend indicates that the quasi Fermi level of holes is not primarily limited by the HTL IE, as some previous observations suggested. Our observation is consistent with previous reports that show a nearly constant $V_{OC}$ over the 5.0 to 5.35 eV IE range, but to the best of our knowledge this is the first report of high $V_{OC}$ values extending to HTLs with IEs significantly outside of this range. Notably, the $V_{OC}$ does fluctuate within a 0.15 V window for HTLs with IEs less than 5.8 eV for devices processed with either Pb precursor. However, these fluctuations in $V_{OC}$ do not correspond with the HTL IE.

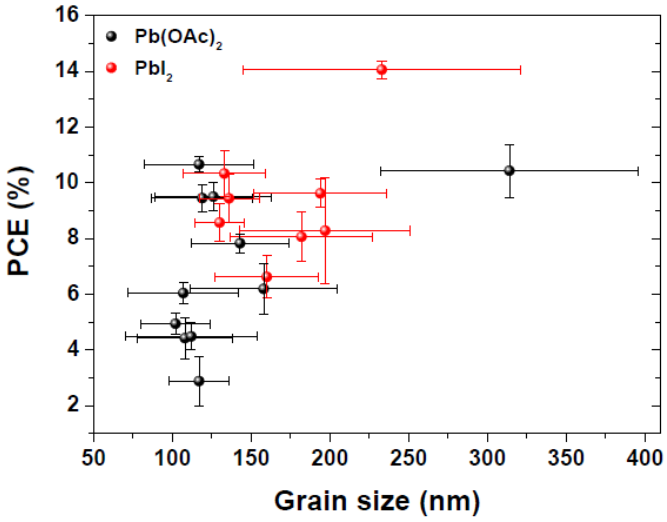


Figure 3.12 Average grain size vs PCE of both $Pb(OAc)_2$ and $PbI_2$ lead source cells

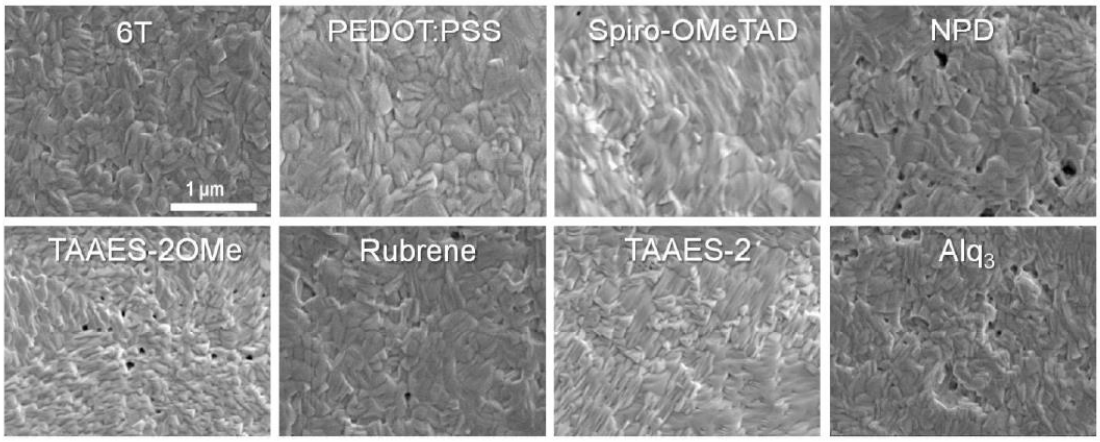


Figure 3.13 Scanning electron microscope images of $MAPbI_3$ films on the various HTLs with $PbI_2$ lead source. All scale bars are 1 µm

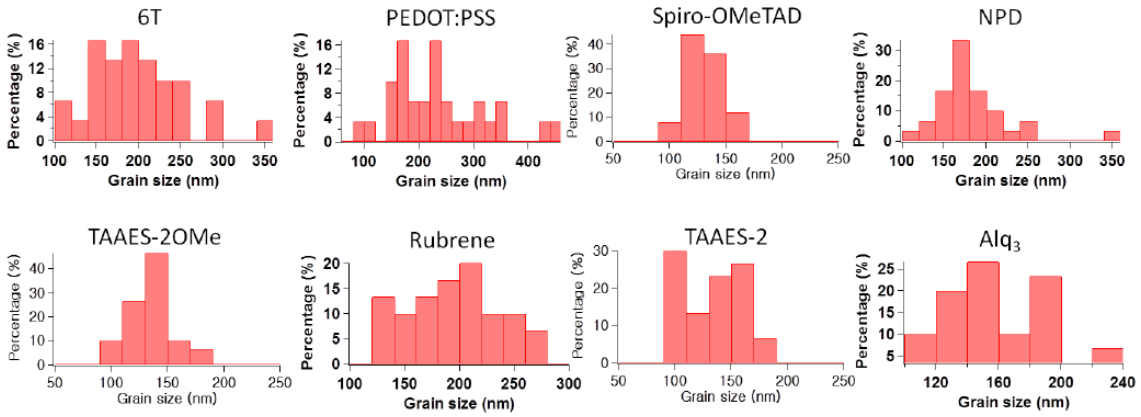


Figure 3.14 Histograms of $MAPbI_3$ films grain size on the various HTLs with $PbI_2$ lead source

Table 3.2 Average grain size and standard deviation of $MAPbI_3$ films on the various $PbI_2$ lead source

| HTLs | Average grain size (nm) | Standard deviation |
|---|---|---|
| 6T | 197 | 54.92 |
| PEDOT:PSS | 233 | 88.12 |
| Spiro-OMeTAD | 130 | 16.08 |
| NPD | 182 | 45.63 |
| TAAES-2OMe | 136 | 19.87 |
| Rubrene | 194 | 42.78 |
| TAAES-2 | 133 | 26.89 |
| $Alq_3$ | 160 | 33.21 |

Other properties of the HTL, such as the charge-carrier mobility, are also likely to influence the PV performance. However, it does not appear that there is a large correlation with the HTL mobility over this series. For example, the charge-carrier mobilities in these HTLs span over two orders of magnitude, with no correlation with the IE. Furthermore, the low-mobility material Spiro-OMeTAD is one of the best performing HTLs. Differences in $MAPbI_3$ film morphology brought about by processing on the different HTLs may also contribute to the observed PV performance differences. For the $Pb(OAc)_2$ procedure, scanning electron microscopy (SEM) images indicate that the morphologies of $MAPbI_3$ are similar on all the HTLs with the exception of 6T, as shown in Figures 3.8 and 3.9. For most HTLs the average grain size ranges from 100 to 160 nm, and these differences in grain size do not correlate with device performance as evident in Figure 3.12. 6T shows an average grain size of 300 nm, which likely explains the larger fill factor. For the $PbI_2$ procedure, the grain sizes are slightly larger with averages between 130 and 230 nm, as shown in Figures 3.13 and 3.14. Again, over this range of grain sizes there does not appear to be a strong correlation with PCE, as shown in Figure 3.12. Overall, the minimal

correlation between grain size and PCE for the observed grain sizes, combined with a lack of correlation between PCE and mobility, leads us to conclude that much of the observed performance differences are due to the IE and the range of acceptable HTL IEs is strongly dependent on the $MAPbI_3$ processing method.

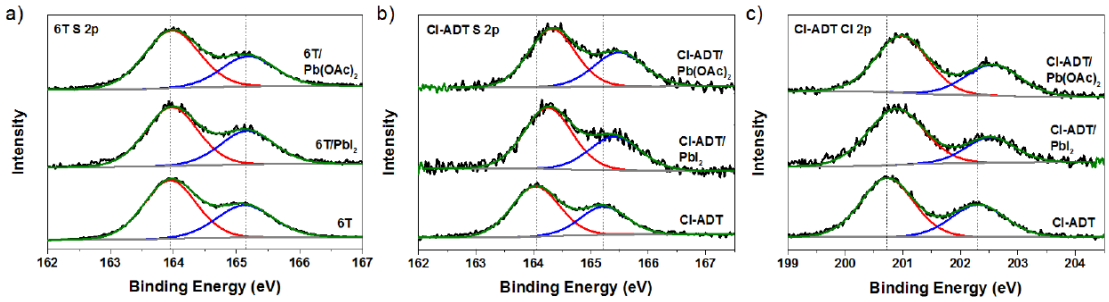


Figure 3.15 XPS spectra showing the S 2p region for 6T (a), S 2p region for Cl-ADT (b), and Cl 2p region for Cl-ADT (c). The bottom traces are the HTL materials prior to perovskite deposition, and the middle and top traces are of the HTL after $MAPbI_3$ was deposited and rinsed off with DMF for films processed from $PbI_2$ and $Pb(OAc)_2$, respectively. The black lines are the measured data and the colored lines are fits to the individual components

Recently it was observed that diffusion of perovskite precursors into or through organic transport layers can lead to degradation of the HTL or to chemical reactions with metal electrodes. It is also possible that diffusion of the perovskite precursors through these HTLs may lead to reactions with the indium tin oxide bottom electrode or the HTLs themselves; which may alter the energetics, introduce trap states, and influence recombination dynamics. To probe whether reactions with ITO or the HTL are influencing the PV performance, we recorded XPS spectra of the ITO, 6T, and Cl-ADT films prior to perovskite deposition and after perovskite deposition and removal (i.e., after the perovskite film was rinsed off of the HTL). XPS analysis of the sulfur 2p and chlorine 2p regions of

the HTLs shows no evidence of reactions between either HTL and the perovskite for perovskites processed with $Pb(OAc)_2$ or $PbI_2$ as the Pb source, as shown in Figure 3.15.

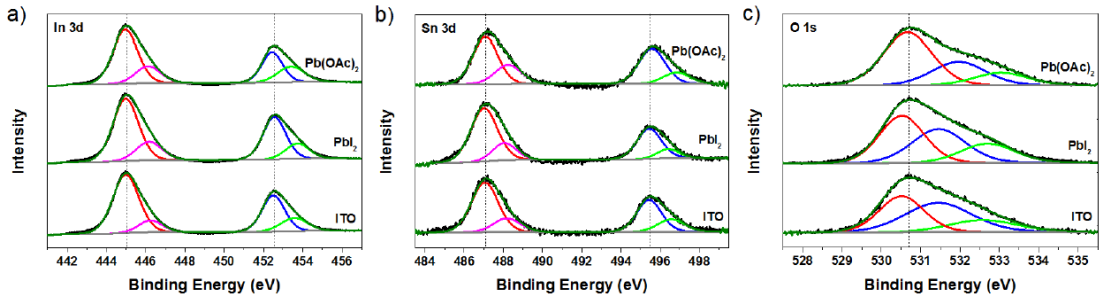


Figure 3.16 XPS spectra showing the In 3d (a), Sn 3d (b), and O 1s (c) regions. Bottom traces are from ITO prior to perovskite deposition, and middle and top traces are from ITO after $MAPbI_3$ was deposited and rinsed off with DMF for films processed from $PbI_2$ and $Pb(OAc)_2$, respectively. The black lines are the measured data and the colored lines are fits to the individual components

Furthermore, the S 2p peaks from 6T do not change after perovskite deposition and removal for either Pb source. Both the Cl 2p and S 2p peaks for Cl-ADT shift by ca. 0.25 eV after perovskite deposition and removal from $Pb(OAc)_2$ and $PbI_2$, but the similarity for both precursors indicates that the energetic shifts are equivalent for the perovskites processed from both precursors. Additionally, to probe if the different perovskite precursor solutions lead to reactions with ITO, we recorded XPS measurements of ITO before perovskite coating and after perovskite coating and removal, as shown in Figure 3.16. All XPS peaks from ITO fall at nearly identical positions before and after perovskite exposure and removal. Thus, our data suggests that the observed differences in device performance for the different HTLs are not due to various extents of HTL degradation or reactions between the perovskite precursors and ITO.

## 3.5 Conclusions

With appropriate IEs, the TAAES derivatives investigated as HTLs show comparable PV performance to the state-of-the art HTLs PEDOT:PSS and Spiro-OMeTAD. Further investigations into the stability of these derivatives will determine if they may provide suitable replacements for PEDOT:PSS or Spiro-OMeTAD. It is well known that the performance of $MAPbI_3$ perovskite photovoltaics are highly sensitive to $MAPbI_3$ processing conditions, and our work demonstrates that these processing conditions even influence the optimum IE range of the HTL materials. Moving forward it will be important to identify why this range depends on $MAPbI_3$ processing conditions, and why the IE of $MAPbI_3$ varies with processing conditions.

# CHAPTER 4. SURFACE LIGANDS FOR PEROVSKITE THIN FILMS: SURFACE COVERAGE, ENERGETICS, AND PV PERFORMANCE



## 4.1 Summary

Surface ligand treatment provides a promising approach to passivate defect states, improve material and device stability, manipulate interfacial energetics, and increase the performance of perovskite solar cells (PSCs). To facilitate targeted selection and design of surface ligands for PSCs, it is necessary to establish relationships between ligand structure and perovskite surface properties. Herein, surface ligands with different binding groups are investigated to determine their extent of surface coverage, whether they form a surface monolayer or penetrate the perovskite, how they influence material energetics and photoluminescence, and how this combination of factors affects PSC performance. Ultraviolet and inverse photoelectron spectroscopy measurements show that surface ligands can significantly shift the ionization energy and electron affinity. These changes in surface energetics substantially impact PSC performance, with the performance decreasing for ligands that create less favorable energy landscapes for electron transfer from $MAPbI_3$ to the electron transport layer, $C_{60}$.

## 4.2 Introduction

Interfaces and grain boundaries are major focal points for improving PV performance and stability, as these areas are more prone to trap state formation and are typically where degradation processes begin.[86,87] Furthermore, recombination in PSCs predominantly occurs at interfaces.[88–90] To reduce interfacial recombination and improve material and device stability, surface ligands are increasingly being applied to halide perovskites (HPs).[91,92] These surface ligands have been applied through both direct incorporation into the precursor solution[93,94] and through post-synthetic treatment of HP films.[18,95] Although many surface ligands have been observed to improve PSC performance and stability, it is not yet clear how different surface ligands interact with the HPs to influence material and interfacial properties. Particularly in the case of incorporation into the HP precursor solution, these surface ligands can influence the film morphology,[96] crystalline structure and orientation,[97] defect density,[98] and material and interface energetics.[99] Even in the more controlled method of post-synthesis modification, many critical parameters are not commonly measured, including the extent of surface ligand coverage or whether the surface ligands remain confined to the surface.

Surface ligands that have been applied to PSCs can be lumped into two primary classes, ammonium containing ligands and ligands[97,100] that can act as Lewis bases and coordinate with Pb.[101–103] Lewis base passivation was first demonstrated by the Snaith group, where thiophene was applied to passivate under-coordinated Pb.[104] Following this initial publication, later reports have examined Lewis bases such as pyridine,[105] dimethyl sulfoxide (DMSO),[106] and N-methyl-2-pyrrolidone (NMP),[33] with this treatment typically increasing the photoluminescence lifetime and improving PV performance. Coordination

of these Lewis bases eliminates the shallow defect states previously present from under-coordinated Pb atoms, i.e., iodide vacancies, and helps to reduce non-radiative recombination.[92,107] On the other hand, ammonium containing ligands are not directly passivating electronically harmful defect states. However, these ammonium ligands can stabilize the surface by protecting the underlying PSC from harmful degradation reactions with oxygen, water, or the metal electrodes in a device,[108] and impact the electronic properties through disruption of the 3D perovskite structure.[18,109] In a best-of-both-worlds approach, bifunctional additives including a group that can act as a Lewis base and an ammonium group have been incorporated into HPs to result in defect state passivation and improved stability.[97,107,110,111] From the perspective of defect state passivation, Lewis base treatment of $MAPbI_3$ films with tri-n-octylphosphine oxide was shown to increase the photoluminescence (PL) lifetime of $MAPbI_3$ to several microseconds,[112] while thiocyanate treatment of $CsPbBr_3$ nanocrystals was shown to increase the PL quantum yield to nearly 100%.[113] In both cases, these surface ligands are filling halide vacancies through coordinating with Pb. In the nanocrystal literature a host of surface ligands that can fill surface halide vacancies have been applied and shown to result in drastic increases in the PL quantum yield, including alkyltrichlorosilanes,[114] trialkylphosphines,[115] thiols,[116] tetrafluoroborates,[117] phosphonates,[118] and carboxylates.[119] From the aspect of stability, surface ligands with hydrophobic tails and carboxylic acids (CAs),[120,121] thiols,[91,102] and ammonium salts[97,122] as binding groups have all been shown to improve the stability of HPs and PSCs. However, it is not known whether these ligands form a thick surface layer, a surface monolayer, sparsely decorate the film surface, or penetrate the HP crystal. Furthermore, it is not yet known how different surface ligands influence the ionization

energy (IE) and electron affinity (EA) of HPs, where the IE and EA can be equated with the valence band maximum and the conduction band minima, respectively. These energetic effects are important to understand, as interfacial energetics can have a large impact on electronic processes within PV devices.[20,90]

In this work we use x-ray photoelectron spectroscopy (XPS) to probe the adsorption of various surface ligands on $MAPbI_3$ as a function of ligand binding group and ligand tail, with angle dependent XPS measurements used to determine whether the ligands remain on the surface or penetrate the $MAPbI_3$ films. Ultraviolet and inverse photoelectron spectroscopy (UPS and IPES, respectively) are then applied to determine how the varying surface ligands influence the IE and EA of the $MAPbI_3$ films. Additionally, we show how these surface ligands influence the optical properties and PV performance of $MAPbI_3$ thin films and devices. Both phosphonic acids (PAs) and ammonium containing ligands are shown to penetrate into the $MAPbI_3$ film, resulting in large changes in surface energetics with certain ligands. Carboxylic acids (CAs) and thiols show lower surface coverage and do not penetrate into $MAPbI_3$, yet both lead to increased PL intensity and improved $MAPbI_3$ stability. Additionally, CAs lead to the most reproducible improvements in PV device performance. Overall, we show that changes in the IE and EA of $MAPbI_3$ play a major role in determining how surface ligands influence PV performance.

## 4.3 Experimental section

### 4.3.1 Materials

Methylammonium iodide (MAI) was purchased from Great Cell Solar and used after recrystallizing twice in ethanol and drying in a vacuum oven overnight at 60 °C. Lead

iodide ($PbI_2$, 99.99%, TCI), poly(triaryl amine) (PTAA, Sigma Aldrich), PEDOT:PSS (Clevios P VP AI 4083), $C_{60}$ (Nano-C, 99.5%), bathocuproine (BCP, TCI, >99%), aluminum (Al, 99.99%, Angstrom Engineering) were used as received. Anhydrous solvents including N,N-dimethylformamide (DMF, Drisolv, anhydrous, 99.8%), dimethyl sulfoxide (DMSO, Millipore SeccoSolv, 99.9%), 2-propanol (IPA, Alfa Aesar, 99.5%), and toluene (Alfa Aesar, 99.8%) were used as received. The surface ligands phenyltrichlorosilane (TCI, 98%), phenylphosphonic acid (Sigma-Aldrich, 98%), 4-bromobenzoic acid (Alfa Aesar, 98%), p-toluic acid (TCI, 98%), trimethylphenylammonium chloride (TCI, 98%), anilinium chloride (Alfa Aesar, 99%), phenylethylammonium iodide (Great Cell Solar), hydroiodic acid (Alfa Aesar, 55-58%), thiophenol (Alfa Aesar, 99%), 1-octylphosphonic acid (Alfa Aesar, 99%), octanoic acid (Alfa Aesar, 98%), 1-octanethiol (TCI, 95%), (1H,1H,2H,2H-tridecafluorooct-1-yl)phosphonic acid (FOPA, SynQuest Labs, Inc, 98%), 4,4,5,5,6,6,7,7,8,8,9,9,9-tridecafluorononanoic acid (FNCA, Sigma-Adrich, 96%), and 3,3,4,4,5,5,6,6,7,7,8,8,9,9,10,10,10-heptadecafluoro-1-decanethiol (FDT, Sigma-Aldrich, 96%) were used as received.

Octylammonium iodide (OAI): OAI was synthesized by reacting octylamine (12.6 mL, 0.076 mol, Alfa Aesar, 99%) and hydroiodic acid (10 mL, 0.076 mol) in 20 mL of ethanol at 0 °C for 2 h with stirring. The resulting solution was dried at 50 °C with a rotary evaporator to remove the solvents. The product was dissolved in ethanol and recrystallized from diethyl ether. The product was rinsed three times with diethyl ether and dried in a vacuum oven at 60 °C overnight before use.

### 4.3.2 Materials characterization

X-ray photoelectron spectroscopy (XPS) measurements were performed with a PHI 5600 ultrahigh vacuum system (UHV) with a hemispherical electron energy analyzer. Al Kα source (1486.6 eV, PHI 04-548 dual anode X-ray source) for excitation and a pass energy of 23.5 eV were used for XPS acquisition. For XPS analysis of the samples that were prepared with the toluene solution soaking method, the Mg anode (1253.6 eV) was used to avoid a satellite peak in the C region that appears with the Al Kα source. Ultraviolet photoelectron spectroscopy (UPS) measurements were taken with an Excitech H Lyman-α photon source (10.2 eV) with an oxygen-filled beam path coupled with the same PHI 5600 UHV and analyzer system. A sample bias of -5 V and a pass energy of 5.85 eV were used for UPS acquisition. IPES measurements were performed in the Bremsstrahlung isochromat mode with electron kinetic energies below 5 eV and an emission current of 2 μA to minimize sample damage. A Kimball Physics ELG-2 electron gun with a BaO cathode was used to generate the electron beam. Emitted photons were collected with a bandpass photon detector consisting of an optical bandpass filter (254 nm, Semrock) and a photomultiplier tube (R585, Hamamatsu Photonics). Samples were held at a -20 V bias during all IPES measurements and the UHV chamber was blacked-out to exclude external light.

Samples for scanning electron microscopy (SEM) were prepared on ITO-coated glass substrates in an identical manner as the PV cells (through surface ligand treatment) and probed with a Hitachi S-4300 SEM with an accelerating voltage of 10 kV. UV-Vis absorbance and PL measurements were recorded on thin films in a nitrogen-filled glovebox using an Ocean Optics fiber-optic spectrometer with a thermoelectric cooled CCD detector.

Films for UV-Vis, PL, and XRD measurements were prepared directly on ITO substrates without either PEDOT:PSS or PTAA. XRD spectra were collected with a Bruker-AXS D8 advance diffractometer with Cu Kα radiation (λ = 1.5418 Å) operating at 40 kV and 40 mA. External quantum efficiency (EQE) measurements were conducted as detailed previously.[123]

$MAPbI_3$ film preparation: Non-patterned ITO coated glass substrates (15 Ω/□) were sequentially sonicated in aqueous detergent (sodium dodecyl sulfate, Sigma-Aldrich), deionized water, acetone, and 2-propanol each for 10 min. After drying with nitrogen the substrates were exposed to UV-ozone treatment for 10 min to remove organic contaminants. PEDOT:PSS or PTAA was the spun cast. PEDOT:PSS was spun cast at 5000 rpm for 30 s and then annealed on a hotplate at 130 °C for 15 min in air, with these PEDOT:PSS coated substrates being used for the toluene soaking surface ligand treatment process. In the case of the IPA spin-coating procedure, 100 µL of PTAA (2.5 mg/mL in toluene) was spun-cast at 4000 rpm for 35 s with a 2 s ramp inside the nitrogen-filled glovebox (<0.1 ppm of $O_2$ and $H_2O$). For the $MAPbI_3$ films, 461 mg of $PbI_2$, 159 mg of MAI, and 78 mg of DMSO (1:1:1 molar ratio) were dissolved in 600 mg of DMF and stirred at room temperature for 1 h before use in the nitrogen-filled glovebox.

$MAPbI_3$ film preparation for toluene solution soaking method: After the PEDOT:PSS coated substrates cooled back to room temperature, 100 µL of filtered (0.45 µm Nylon membrane filter) HP solution was spin-coated on top of the PEDOT:PSS layer in ambient atmosphere (humidity 25 ± 3%). The $MAPbI_3$ precursor solution was spun-cast at 4000 rpm for 25 s with a 2 s ramp, and 0.5 mL of diethyl ether was rapidly injected onto the substrate 5 s into the spin-coating process. Immediately following spin-coating, the

substrates were heated at 65 °C for 1 min and 100 °C for 5 min. After annealing, the films were brought into the nitrogen-filled glovebox for further processing.

For surface modification, $MAPbI_3$ films were submerged in 1 mg/mL solutions of the surface ligands in toluene in covered petri dishes for 1 hour at room temperature inside of the nitrogen-filled glovebox. After 1 hour, the substrates were dried through spin coating off the remaining solution at 4000 rpm for 30 s with a 2 s ramp. To remove excess unbound surface ligands, 200 μL of toluene was dripped three times in the beginning stage of spin-coating. No additional heating was applied.

$MAPbI_3$ film preparation for IPA spin-coating method: Following PTAA coating, 80 μL of $MAPbI_3$ solution (prepared as detailed above) was deposited and spun-cast at 1000 rpm for 5 s followed by 3000 rpm for 80 s. 100 μL of toluene was dropped on the spinning substrate after 10 s of reaching 3000 rpm, resulting in the formation of transparent films that were then annealed on a hot plate at 100 °C for 10 min. 100 μL of surface ligand solution in IPA was then deposited on the dark $MAPbI_3$ films and left to sit for 10 s before spinning at 4000 rpm for 30 s with a 2 s ramp. To remove excess unbound ligands, the substrates were rinsed with toluene (3 x 200 μL aliquots during spinning).

PV device fabrication and characterization: $MAPbI_3$ films were prepared on patterned ITO coated glass substrates (15 Ω/□) and treated with surface ligands following the above procedure for the IPA spin-coating method. The treated films were then transferred to the thermal evaporator without air exposure and $C_{60}$ (30 nm) and BCP (8 nm) were deposited sequentially with a rate of 1 Å/s and 0.5 Å/s, respectively, at a pressure of ca. $2 \times 10^{-6}$ mbar. Finally, aluminum (100 nm) electrodes were evaporated through a shadow mask that defined 12 cells of 0.1 $cm^2$ area per substrate. Solar cell performance

was measured using a solar simulator (ABET technologies, 11002) at 100 mW/cm$^2$ illumination (AM 1.5G). The intensity was adjusted to (100 mW/cm$^2$) using a photodiode calibrated with a KG5 filter (ABET technologies).

## 4.4 Results and discussions

### 4.4.1 Surface modification of $MAPbI_3$ films

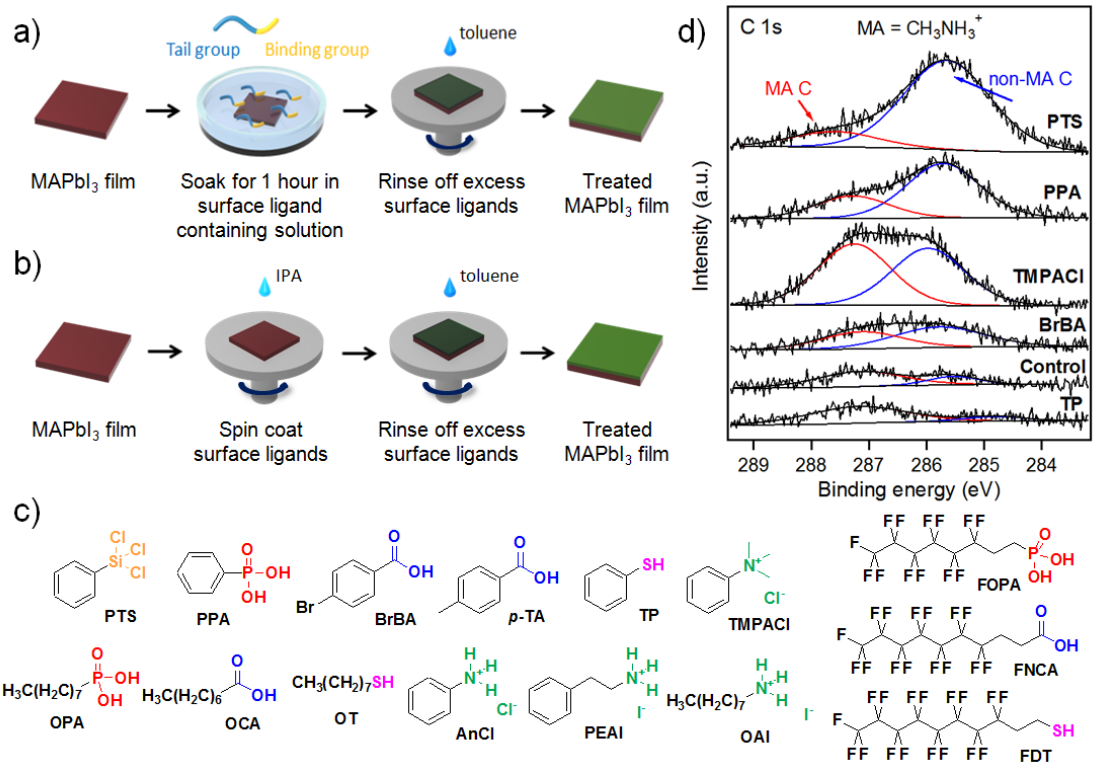


Figure 4.1 Schematic illustration of the toluene solution soaking (a) and IPA solution spin coating (b) surface modification processes. Surface ligands used to treat the $MAPbI_3$ films (c) and XPS of the C 1s region highlighting the MA C (red) and the non-MA C (blue) peaks (d) for $MAPbI_3$ films treated with ligand solutions using the toluene solution soaking method

The $MAPbI_3$ thin films were treated with the surface ligands shown in Figure 4.1 to determine the relative binding ability of the different functional groups. As illustrated in

Figure 4.1a, surface treatment was initially performed through soaking $MAPbI_3$ films in a toluene solution of the surface ligand followed by rinsing to remove unbound ligands. A control $MAPbI_3$ film was treated in the same way without any surface ligand in the toluene solution. Following this initial investigation of surface ligand adsorption, the treatment method was modified to consist of spin coating surface ligand solutions on the $MAPbI_3$ films from an isopropanol (IPA) solution, as shown in Figure 4.1b. The modified procedure was adopted because all surface ligands examined display adequate solubility in IPA, whereas only some are soluble in toluene. Both treatment procedures yield similar results with respect to surface ligand binding. The use of IPA as a solvent for post-synthetic treatment of HP films is comparable with previous reports, where IPA and 2-butanol have been used.[18,124,125] The surface ligand treatment based on spin coating an IPA solution containing the surface ligand of interest was not found to influence the morphology of the underlying $MAPbI_3$ film, as indicated in the scanning electron microscope (SEM) images shown in Figure 4.2.

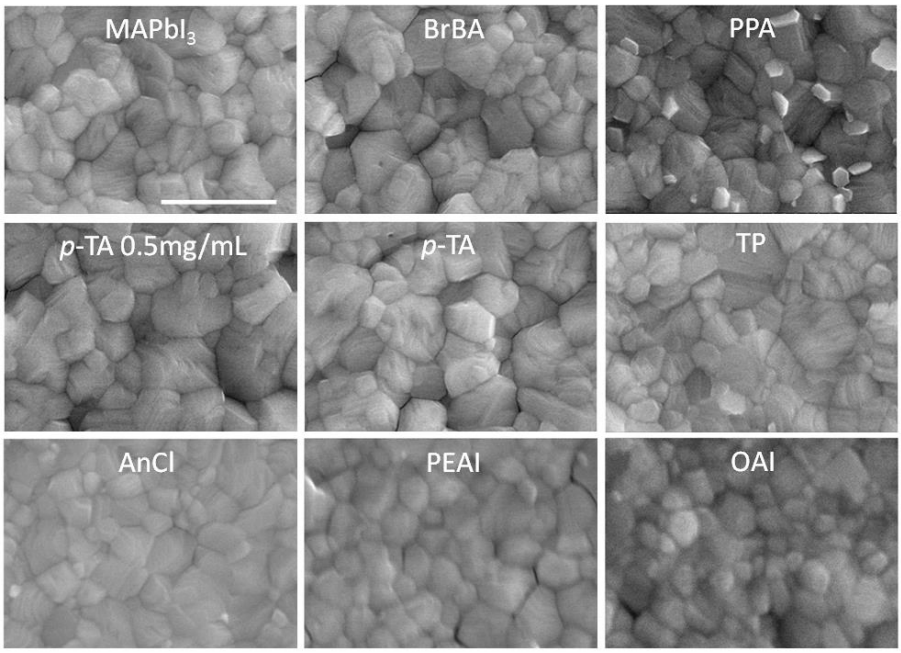


Figure 4.2 Scanning electron microscope images of control and surface ligand treated $MAPbI_3$ films on PTAA hole transport layers. Surface ligand treatment was applied through spin coating solutions of the surface ligands in isopropanol. The scale bar is 1μm and applies to all images

The surface ligands shown in Figure 4.1c were selected for this work to allow for common binding groups to be analyzed, while also enabling the influence of the ligand tail to be probed. The binding groups are expected to bind to the HP surface either through occupying the A-site position or binding to Pb in the X-site position. Previous literature contains reports of each of these binding groups being used to improve the performance of Pb-based PSCs.[97,101,103,121] The tails selected consist of phenyl groups, alkyl groups, and flourinated alkyl groups. The idea being that the aromatic tail groups favor charge transport due to the π-electrons and compact size, while the alkyl and fluorinated alkyl groups are hydrophobic and can therefore potentially enhance stability. Additionally, the differing ligand tails may also alter the adsorption of the ligands through electronic (e.g., pKa or halide-π interactions)[126,127] and steric effects.[128] The series of phenyl derivatives include

phenyltrichlorosilane (PTS), phenyl phosphonic acid (PPA), 4-bromobenzoic acid (BrBA), p-toluic acid (*p*-TA), thiophenol (TP), trimethylphenylammonium chloride (TMPACl), anilinium chloride (AnCl), phenylethylammonium iodide (PEAI), while the octyl derivatives include octylphosphonic acid (OPA), octanoic acid (OCA), octanethiol (OT), and octylammonium iodide (OAI), and fluorinated alkyl derivatives include (1H,1H,2H,2H-tridecafluorooct-1-yl)phosphonic acid (FOPA), 4,4,5,5,6,6,7,7,8,8,9,9,9-tridecafluorononanoic acid (FNCA), and 3,3,4,4,5,5,6,6,7,7,8,8,9,9,10,10,10-heptadecafluoro-1-decanethiol (FDT).

To identify the extent of ligand binding, the ratio of the C 1s peak area from non-MA carbon to MA carbon was probed with XPS for the phenyl substituted ligands, as sho wn in Figure 4.1d. As methylammonium is positively charged, the MA C appears at a bin ding energy of ca. 287 eV, whereas non-MA C appears at ca. 285.5 eV. The XPS data pre sented in Figure 4.1d show that all phenyl substituted ligands, except for TP, adsorb to the $MAPbI_3$ surface to varying extents. Following TP, BrBA shows the weakest adsorption, b oth TMPACl and PPA show moderate adsorption, and PTS forms the thickest surface lay er. Although some ligands may serve their intended function of forming a surface layer, th ey can also introduce potential complications. For example, PTS adsorption can be difficu lt to control, commonly leading to thick surface layers. Here, PTS is likely reacting with t race amounts of water in the glovebox atmosphere and nominally anhydrous solvents to f orm a siloxane layer,[114] as supported by the 17% O and 8% Si elemental composition that we measured with XPS following PTS treatment of $MAPbI_3$. On the other hand, TMPACl can disrupt the crystalline structure of $MAPbI_3$ over longer exposure times, as evident in t he SEM images shown in Figure 4.3. For ligands that are not limited to a surface monolay

er, such as PTS and TMPACl, ligand deposition conditions are likely to have a larger effe ct on surface properties.

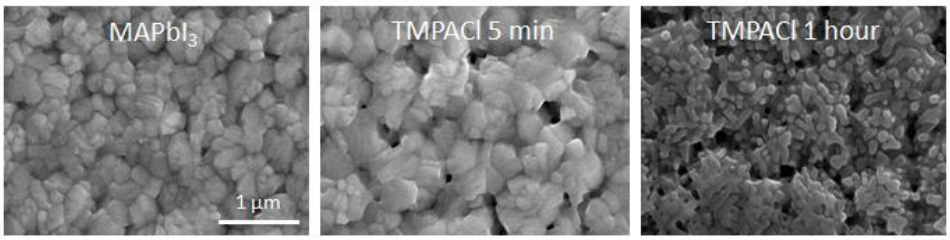


Figure 4.3 Scanning electron microscope images of control and TMPACl treated $MAPbI_3$ films with varying soaking times (toluene soaking surface ligand treatment procedure). All scale bars are 1µm

The influence of surface ligands on optical, electronic, and PV properties is determined in part by the extent of surface coverage and whether the ligands remain on the surface or penetrate the HP. We performed angle dependent XPS measurements, as illustrated in Figure 4.4a, to quantify the degree of surface coverage and probe ligand penetration. Three different electron take-off angles were measured, 0, 45, and 75°, to vary the probing depth. Since the mean free path of photoelectrons are typically two to four nanometers at kinetic energies of near 1000 eV,[129–131] the probing depth is varied from approximately 6 to 8 nm at 0° to only 1.5 to 2 nm at 75°. The surface coverage of the ligands on the $MAPbI_3$ films are calculated based on work by Gao, et al.[132] and Carl, et al.[133] Briefly, the substrate overlayer model is used to convert peak area ratios measured with XPS (e.g., the O 1s peak) to a fractional monolayer coverage based upon the surface ligand structure.[134–136] As shown in equation (7), the ratio of XPS peak areas arising from the overlayer ($I_{OV}^{x}$) and the substrate ($I_{Sub}^{y}$) are related to the fractional coverage (Φ) of the overlayer, where the overlayer is the surface ligand layer and the substrate is $MAPbI_3$.

Here, $I_{OV}^{x}$ and $I_{Sub}^{y}$ correspond to XPS peaks from elements that are unique to the overlayer or substrate, respectively.

$$\frac{I_{OV}^{x}}{I_{Sub}^{y}} = \frac{SF^{x}}{SF^{y}} \frac{\rho_{a,OV}^{x}}{\rho_{a,Sub}^{y}} \frac{\lambda_{OV}^{x}}{\lambda_{Sub}^{y}} \frac{\phi\,(1-\exp\left[-\frac{d_{OV}}{\lambda_{OV,self}^{x}Cos(\theta)}\right])}{1-\phi+\phi\,\exp\left[-\frac{d_{OV}+D}{\lambda_{Sub,OV}^{y}Cos(\theta)}\right]} \qquad (7)$$

In equation (2), $\rho_{a,i}^{x}$ is the atomic density of an element (x or y) from the overlayer (ov) or substrate (Sub), λix is the attenuation length of an element x in an infinitely thick layer i, $SF^{x}$ is the sensitivity factor of an element x, $d_{OV}$ is the thickness of the layer from which photoelectrons of element x are passing, *D* is the thickness of the region where the photoemitted electrons of interest from the overlayer are emitted from, $\lambda_{OV,self}^{x}$ is the attenuation length of element $x$ passing through the overlayer itself, $\lambda_{Sub,OV}^{y}$ is the attenuation length of element y passing through the surface ligand layer with length of $d_{OV}+D$, and the electron takeoff angle ($\theta$) is the angle between the detector and the substrate surface normal. These parameters are shown for PPA in Figure 4.4b and have been substituted as shown in equation (8). Here, $\beta$ indicates the tilt angle of the ligand with respect to the surface normal, which shortens $d_{OV}$ and *D* by their product with Cos($\beta$). In our calculations of the PAs and CAs we examined the intensity ratio between oxygen (O) and iodide (I), where O is from the surface ligand and I is from $MAPbI_3$.

$$\frac{I_{PA}^{O}}{I_{MAPbI_3}^{I}} = \frac{SF^{O}}{SF^{I}} \frac{\rho_{a,PA}^{O}}{\rho_{a,MAPbI_3}^{I}} \frac{\lambda_{PA}^{O}}{\lambda_{MAPbI_3}^{I}} \frac{\phi\left(1-\exp\left[-\frac{d_{\mathrm{Phenyl}}\,Cos(\beta)}{\lambda_{\mathrm{Phenyl}}^{O}\,Cos(\theta)}\right]\right)}{1-\phi+\phi\,\exp\left[-\frac{d_{PPA}Cos(\beta)}{\lambda_{PPA}^{I}Cos(\theta)}\right]} \qquad (8)$$

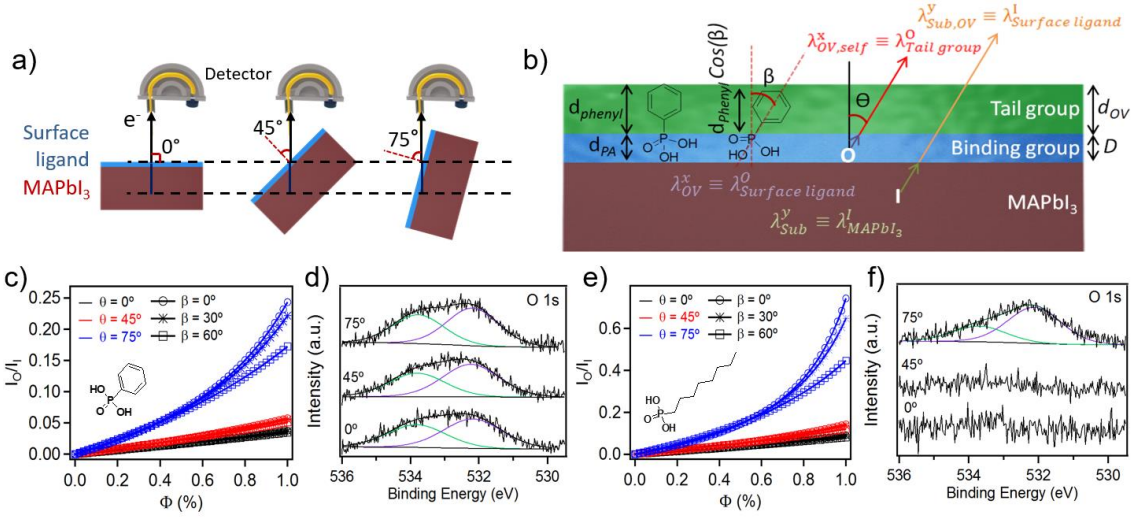


Figure 4.4 Schematics of the a) angle-dependent XPS measurements with dashed lines indicating the relative photoelectron probing depth and b) PPA binding showing the parameters in equations (7) and (8). Calculated $I_0/I_I$ vs surface coverage (Φ) for varying tilt angles ($\beta$) and takeoff angles ($\theta$) for c) PPA and e) OPA. O 1s region of the XPS spectra of d) PPA- and f) OPA- treated $MAPbI_3$ films at three different takeoff angles. The peak fitting represents O in different binding states (e.g., P-O and P=O)

Figure 4.4c shows the calculated O:I ratio as a function of PPA surface coverage on $MAPbI_3$ at three different $\theta$ and $\beta$ values. The experimentally measured O 1s intensity for the PPA-modified $MAPbI_3$ film shows only a small change with $\theta$, as shown in Figure 4.4d, and results in O:I ratios ranging from 0.52 to 0.78. The minimal dependence of the O:I ratio on $\theta$ indicates that PPA is likely penetrating into $MAPbI_3$ as opposed to forming a surface layer. In contrast with PPA modification, Figure 4.4f illustrates that the OPA-modified $MAPbI_3$ film does show the predicted variation in the O 1s region with $\theta$ for an overlayer that remains above the $MAPbI_3$ surface. At a 75° takeoff angle, the O:I ratio is 0.6±0.1, which indicates that the surface coverage is 96 ± 4% with a $\beta$ between 0° and 30° (Figure 4.4e). At small θ values of 0° and 45°, the O:I ratio should be ~0.1, which is below our limit of detection. These measurements show that the tail group attached to the PA

binding group significantly influences whether the ligand is confined to the surface or penetrates the $MAPbI_3$ film.

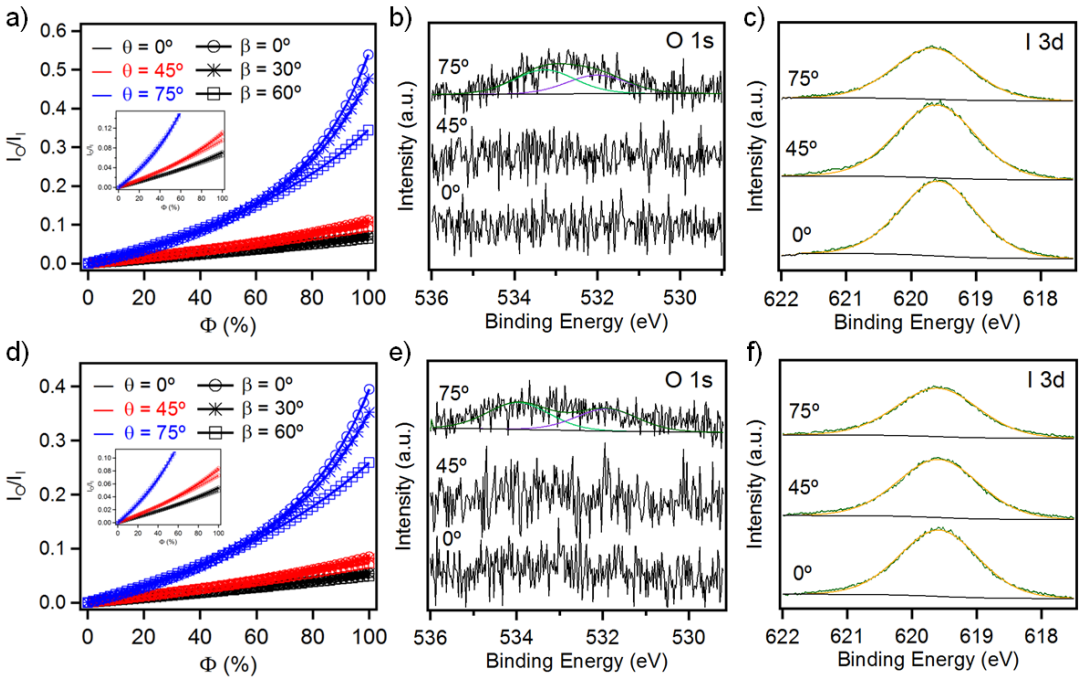


Figure 4.5 Calculated ratios of O 1s and I $3d_{5/2}$ signal intensity vs. surface coverage for OCA (a) and BrBA (d) at 3 different angles between sample and detector (0°, 45° and 75°) and 3 different molecular tilt angles (0°, 30° and 60°). Angle dependent XPS of the O 1s (b) and I $3d_{5/2}$ (c) regions at θ= 0°, 45° and 75° for OCA (b,c) and BrBA (e,f) treated $MAPbI_3$

Surface ligands containing CAs as the binding group were investigated with both phenyl and heptyl tails. The XPS O 1s region for BrBA- and OCA-modified $MAPbI_3$, as well as the calculated O:I ratios, is shown for three different angles in Figures 4.5. The experimental results indicate that these CA- containing surface ligands are both confined to the surface. Comparison between the measured and calculated O to I ratios indicate incomplete surface coverages of 71 ± 10% for OCA and 69 ± 10% for BrBA.

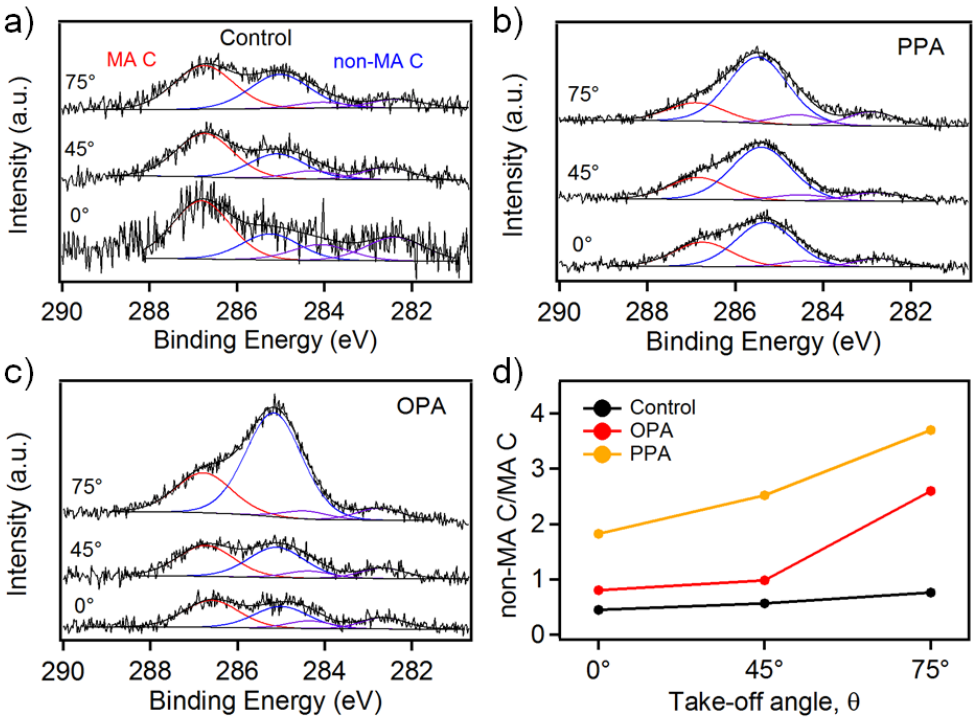


Figure 4.6 Angle dependent XPS of the C 1s region at θ= 0°, 45° and 75° for (a) untreated $MAPbI_3$, (b) with PPA treatment and (c) and with OPA treatment. The red peak is fit to the MA carbon and the blue peak is fit to the non-MA carbon. (d) Ratio of Non-MA carbon to MA carbon for all the films at all measured angles

Ammonium containing ligands, which have been shown to result in improved performance and stability in PSCs, were also investigated with varying tail groups. Since the ammonium containing surface ligands do not have unique elements to detect in XPS, we compare the MA C and non-MA C in the C 1s region. As shown in Figure 4.7, AnCl shows the smallest amount of additional non-MA C, with ratios ranging from 1.5 to 3.0 as the takeoff angle is varied. These ratios at varying takeoff angles are similar to those of PPA-modified $MAPbI_3$, as shown in Figure 4.7d, which supports the idea that AnCl also penetrates into the $MAPbI_3$ film. The other ammonium containing surface ligands, PEAI and OAI, show further increased non-MA C:MA C ratios at all angles. This data indicates that all ammonium-containing ligands penetrate the $MAPbI_3$ films, which is consistent with

previous X-ray diffraction (XRD) data that show the formation of a two-dimensional (2D) perovskite phase upon treatment of $FA_{1-x}MA_xPbI_3$ with PEAI.[18] Notably, based on previous results,[18] the penetration of ammonium groups into the $MAPbI_3$ film can have a positive influence on PV performance in conventional architecture (n-i-p) devices and improve material and device stability.

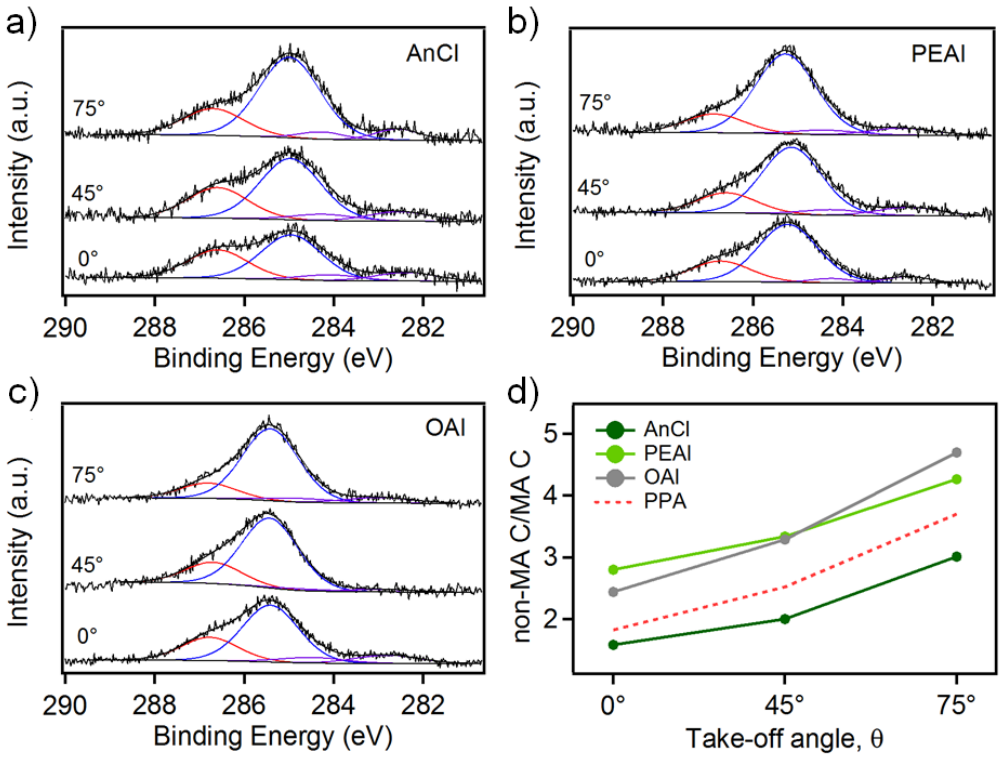


Figure 4.7 Angle dependent XPS of the C 1s region at θ= 0°, 45° and 75° for (a) AnCl, (b) treated film with PEAI and (c) treated film with OAI. The red peak is fit to the MA carbon and blue is the fit to the non-MA carbon. (d) Ratio of non-MA C to MA C for the films as a function of the electron take-off angle

The I:Pb ratio as determined by XPS for the ammonium-treated films indicates that the region near the surface consists of a perovskite phase that is closer to the 3D perovskite than the n = 1 2D perovskite, i.e., $Am_2MA_{n-1}Pb_nI_{3n+1}$, where Am is the ammonium-functionalized ligand. Here, the I:Pb ratio is between 2.8 and 3.0 for the control film and

between 2.9 and 3.2 for the AnCl- and OAI-treated films at all measured electron takeoff angles. Considering that an I:Pb ratio of 3.2 corresponds with n = 5, we can conclude that the average n value in the near surface region is >5 for the $MAPbI_3$ films treated with the ammonium-containing surface ligands.

### 4.4.2 Surface energetics

Surface energetics are known to vary based upon surface modification,[137,138] with the addition of a surface ligand typically resulting in a shift in the work function based on the orientation and magnitude of the dipole moment of the surface ligand and the bond dipole with the underlying material.[138–140] Furthermore, the surface ligand may also perturb the electronic structure of $MAPbI_3$ near the film surface, e.g., by distorting the $MAPbI_3$ crystalline lattice through the penetration of bulky ligands into the film or though altering the surface states and the electrostatic environment.[109,141,142] Thereby, it is important to understand how the different surface ligands impact the energetics of $MAPbI_3$ in the region near the surface. The UPS and IPES measurements reported herein were collected with lower photon and electron energies than typical UPS and IPES systems,[143,144] which has been shown to minimize sample damage. All IE and EA values are assigned based on a Gaussian fit to the UPS and IPES onset region performed on a logarithmic scale.[75]

Ultraviolet and inverse photoelectron spectroscopy measurements, as displayed in Figure 4.8, show that treatment with PAs results in the largest changes to the spectral shape, EA, and IE; the CAs result in minimal changes to the IE and EA; and the ammonium-substituted ligands result in changes that are highly dependent on the tail group. Both PPA and OPA lead to broader onsets to the occupied and unoccupied states, decreased EAs, and

decreased IEs. As Figure 4.8 shows, PPA and OPA treatment result in decreases of 0.45-0.69 eV in the EA and 0.57-0.39 eV in the IE. On the other hand, both *p*-TA and OCA show IEs that are within 0.16 eV of the control film and EAs that are within 0.02 eV of the control. AnCl also results in more minimal changes to the UPS and IPES spectra, as shown in Figure 4.8c, with only small shifts of 0.13 and 0.17 eV in the EA and IE, respectively. However, OAI treatment results in larger shifts in both the EA and IE of 0.37 and 0.27, respectively. Treatment with AnCl results in a minimal increase in the transport gap as compared to the control film, while treatment with OAI results in a small increase of 0.10 eV, which is consistent with the formation of a high n phase of $OA_2MA_{n-1}Pb_nI_{3n+1}$ near the interface. These UPS and IPES results show that the $MAPbI_3$ surface energetics are sensitive to both the ligand binding group and the ligand tail.

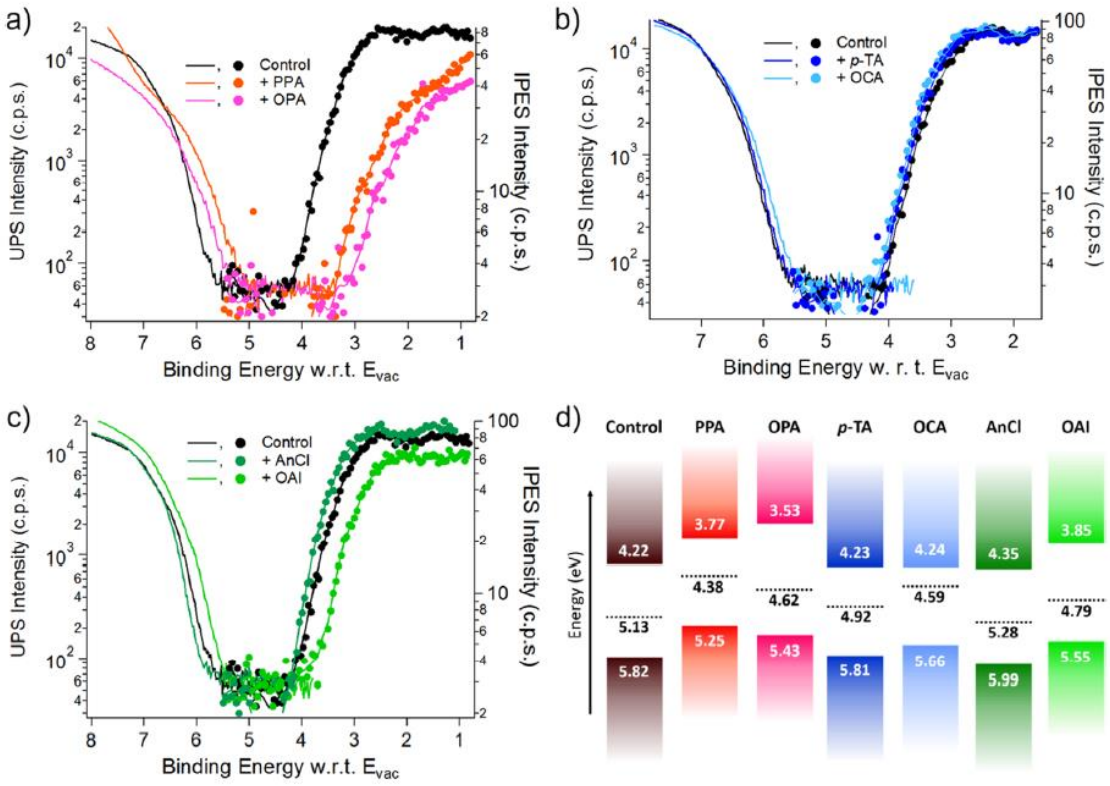


Figure 4.8 Ultraviolet and Inverse photoelectron spectroscopy spectra of $MAPbI_3$ films treated with PA containing ligands, PPA and OPA (a), carboxylic acid (CA) containing ligands, *p*-TA and OCA (b), and ammonium containing ligands, AnCl and OAI (c). Energy level diagrams determined from the UPS and IPES spectra of the $MAPbI_3$ films (d)

The photoelectron spectroscopy data can in part be rationalized by considering how the surface ligands interact with the $MAPbI_3$ films. The CAs result in only partial surface coverage and do not penetrate into $MAPbI_3$, and thereby, minimal changes in the IE and EA are observed. On the other hand, the PA- and ammonium-containing ligands form near complete surface coverage or penetrate into the $MAPbI_3$, thus resulting in more drastic changes to the $MAPbI_3$ electronic structure and the EA and IE. Furthermore, the ammonium ligands can change the surface stoichiometry from being iodide rich to ammonium rich, which has previously been demonstrated to result in changes to the IE.[109,142] We suspect that the larger changes upon OAI treatment as compared to AnCl

treatment may result from the increased amount of OAI incorporated into the $MAPbI_3$ film in the near-surface region, as indicated by the XPS data in Figure 4.7. Additionally, the larger size of OAI and the different interactions between $MAPbI_3$ and the alkyl group on OAI as compared to the phenyl group on AnCl may also be contributing to the observed differences between the two ammonium-containing surface ligands.

### 4.4.3 Photoluminescence and photovoltaic characteristics

The PL intensity of $MAPbI_3$ thin films are one indicator of the potential PV performance.[94,95,103] Figure 4.9a displays the PL spectra of surface ligand treated $MAPbI_3$ films recorded within 2 hours of surface ligand treatment in a nitrogen filled glovebox with <0.1 ppm $O_2$ and $H_2O$. The CA substituted ligands show the greatest increase in PL intensity, with both *p*-TA and BrBA showing a doubling of the PL intensity relative to the untreated film. Surprisingly, even though thiols are not observed to bind to the surface at a concentration that can be detected in the XPS measurements, they result in the second highest PL intensity. This is likely due to limited adsorption of thiols to under-coordinated Pb atoms at the surface that can serve to passivate the shallow traps that result from iodide vacancies.[102,104] The ammonium and PA-containing surface ligands show less drastic changes to the PL intensity, with changes of ±30% relative to the untreated $MAPbI_3$ film.

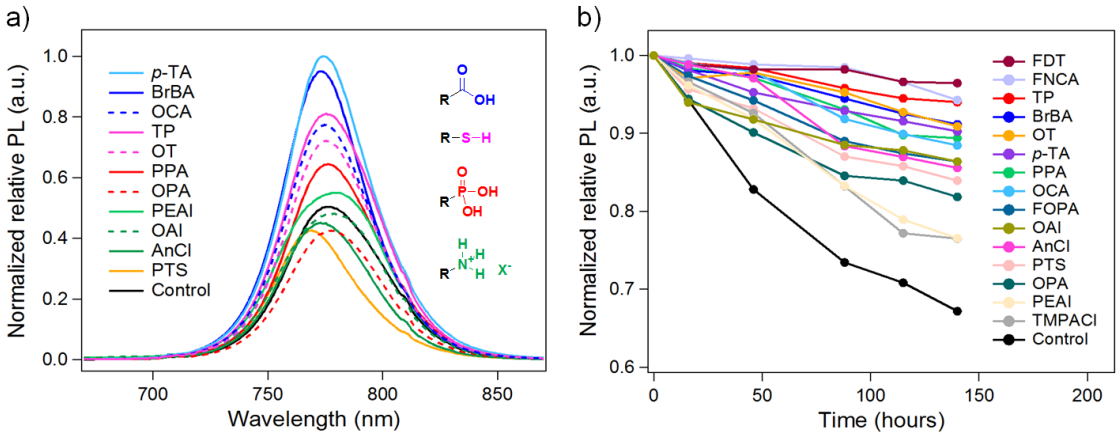


Figure 4.9 Photoluminescence spectra of $MAPbI_3$ films treated with varying surface ligands. Solid and dashed lines correspond with aryl and alkyl containing ligands (a). Relative PL intensity as a function of time after surface ligand treatment for untreated and surface ligand treated $MAPbI_3$ films (b)

All ligands improve the PL stability of $MAPbI_3$, with the stability depending both on the tail group and the binding group. Figure 4.9b shows that the fluorinated ligands with CA and thiol binding groups result in the highest stability, retaining over 95% of the original PL intensity after 6 days of storage in the glovebox. The phenyl substituted thiols and CAs show the next highest stability, followed by the PA and ammonium substituted ligands. The PL stability measurements shed light on degradation mechanisms, and interestingly ligands with lower surface coverage result in the greatest PL stability. We suspect that this trend arises as the CA and thiol containing ligands likely bind to under-coordinated Pb at the surface, thereby prohibiting degradation processes that begin at these sites, without disrupting the $MAPbI_3$ crystalline structure near the surface. The UV-vis absorbance, as shown in Figure 4.10, shows minimal change upon surface ligand treatment. X-ray diffraction data, as shown in Figure 4.11, also shows minimal change in $MAPbI_3$ crystalline structure upon surface ligand treatment. In general, the UV-Vis and XRD data

indicate that the ligands are primarily influencing the $MAPbI_3$ surface and near-surface region, with the properties of the bulk remaining largely unchanged.

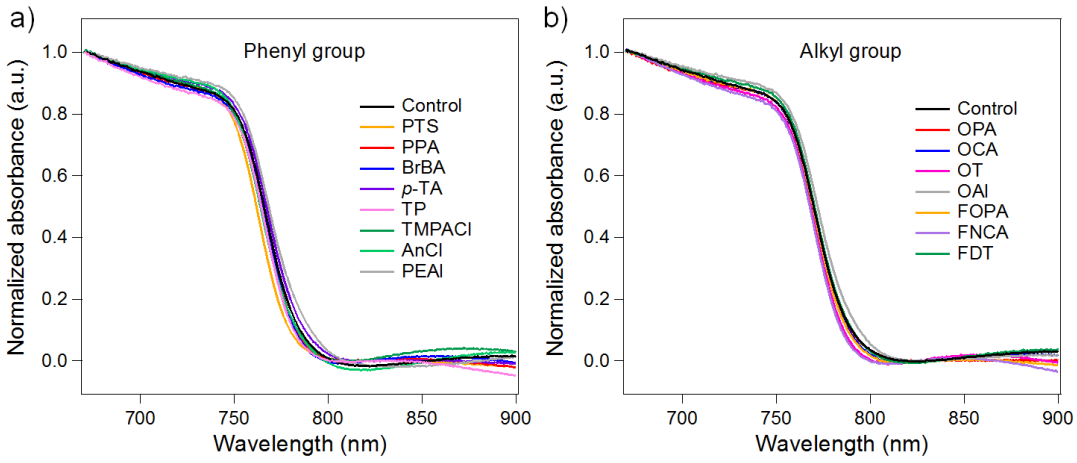


Figure 4.10 UV-Vis absorbance spectra of thin films of untreated and surface ligand treated $MAPbI_3$ films

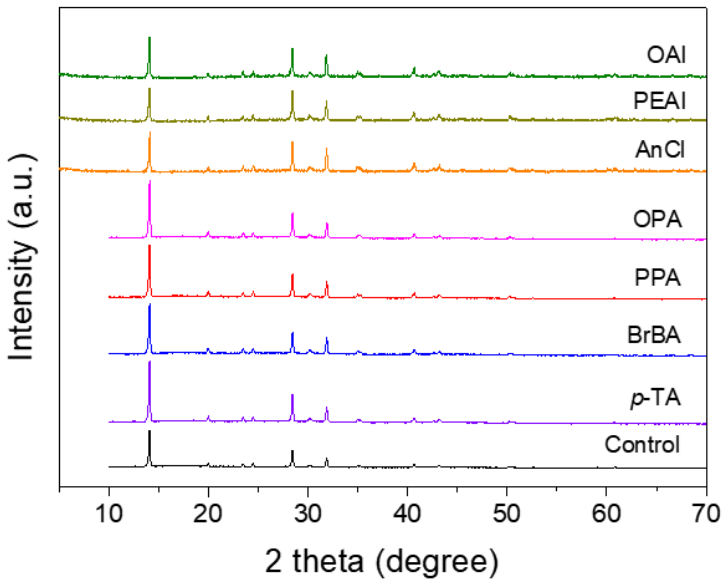


Figure 4.11 XRD spectra of untreated and surface ligand treated $MAPbI_3$ films

Inverted architecture (p-i-n) planar PSCs were used to examine the effect of surface ligands on the performance of $MAPbI_3$-based devices. The device architecture is

ITO/PTAA/$MAPbI_3$/surface ligand/$C_{60}$/BCP/Al, as shown in the inset in Figure 4.12, with the PV performance parameters summarized. Device fabrication was carried out with the surface ligands being spun-cast from IPA on top of the annealed $MAPbI_3$ film and rinsed with toluene. The control devices were treated the same way using pure IPA for comparison, which did not negatively influence the PV performance.

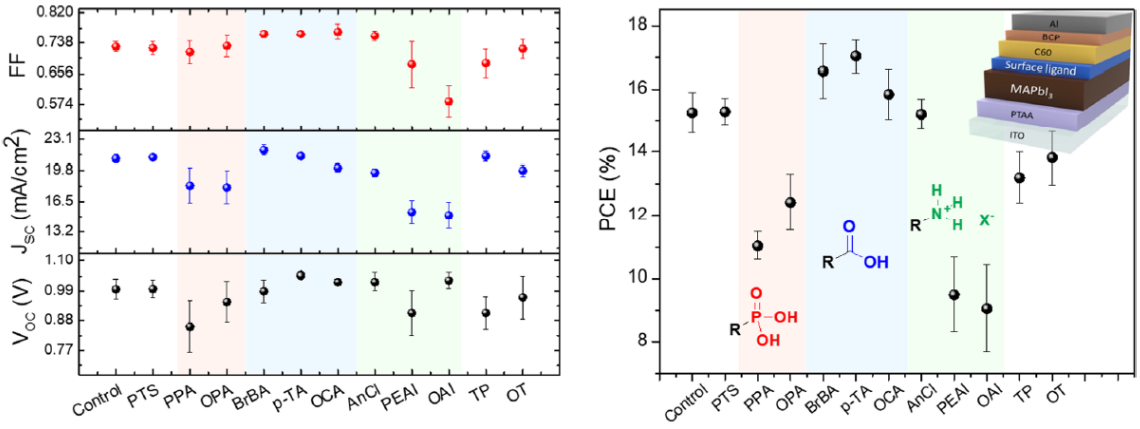


Figure 4.12 PV performance parameters as measured under exposure to AM 1.5 solar simulated irradiation

The control devices yield an average PCE of 15.3±0.7%, with these results compiled from 23 individual PV cells made on multiple days. Phenyltrichlorosilane (PTS), CAs, and thiols result in small changes in performance, with PTS showing no change in PCE, CAs showing increased PCEs, and thiols showing slightly decreased PCEs. The PV performance with the ammonium-containing ligands depends strongly on the tail group, with AnCl displaying a similar PCE as the control and both PEAI and OAI showing greatly reduced PCEs in the 9% range. Both PA containing ligands tested yield lower PCEs in the range of 11 and 12%. The predicted short circuit current density, $J_{SC}$, from the integrated EQE spectra recorded for selected ligands agree to within 6% of the $J_{SC}$ measured from the

illuminated current-voltage curves, as shown in Figure 4.14. Additionally, no devices showed significant hysteresis.

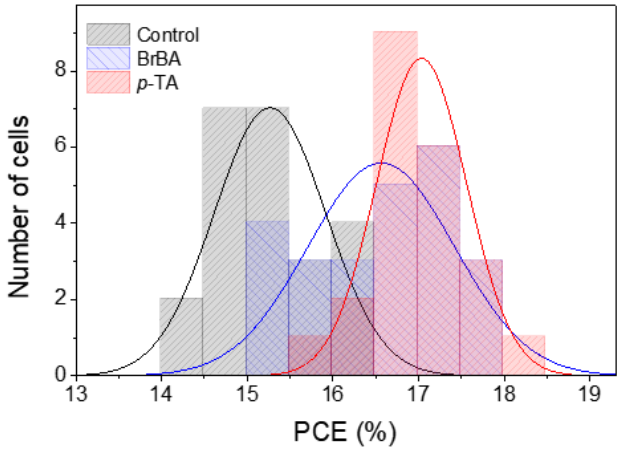


Figure 4.13 PCE distribution of PV devices with untreated, BrBA treated, and *p*-TA treated $MAPbI_3$

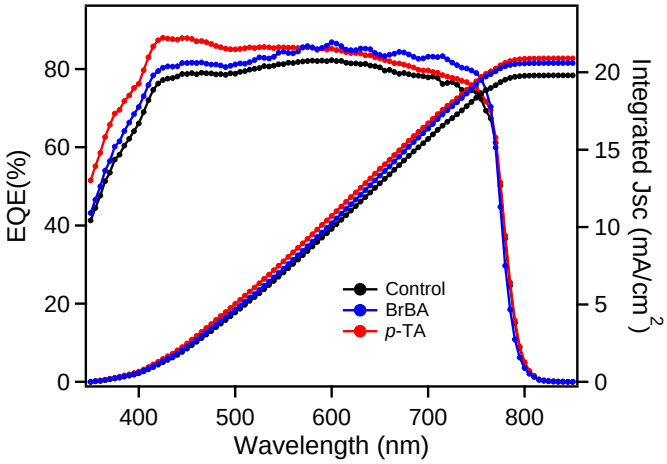


Figure 4.14 External quantum efficiency and integrated current densities for PV devices with untreated, BrBA treated, and *p*-TA treated $MAPbI_3$

The improvements in PV performance observed for the CA-containing ligands agree with the increased PL intensity in Figure 4.9a and indicate the CA-containing ligands are helping to passivate surface traps. On the other hand, the ammonium-containing ligands

yield similar PL intensities yet result in large differences in PV performance. To explain why the PV performance drops significantly for OAI and PEAI but remains at the same level as that of the control for AnCl, we turn to the surface energetics as measured with IPES and UPS. On the basis of the lack of change in the XRD spectra observed upon surface modification, we expect that the ammonium-containing ligands do not penetrate past the near surface region of the film. Thus, we expect that the energetics in the bulk of the $MAPbI_3$ films remain similar to those of the unmodified film and only the region near the surface displays the altered EA and IE, which leads to the energy diagrams displayed in Figure 4.15. Here, the OAI-treated film presents an energetic barrier for electron transfer from the bulk of $MAPbI_3$ through the surface region to $C_{60}$. Treatment with AnCl presents no such barrier.

The attribution of decreased PV performance to an unfavorable energetic landscape is supported through the observation that both phosphonic acid derivatives, which also result in an unfavorable energetic landscape for electron transfer to $C_{60}$ in Figures 4.8d and 4.15b, show significantly decreased PV performance. As with the ammonium salts, these PA-treated $MAPbI_3$ films show a PL intensity similar to that of the control $MAPbI_3$ films in Figure 4.9, and neither the SEM images nor the XRD spectra show significant differences with the control $MAPbI_3$ in Figure 4.2 and 4.11. Further support for the idea that surface energetics play a major role in determining the PV performance is offered by the *p*-TA and OCA-treated $MAPbI_3$ films. Both *p*-TA and OCA result in minimal shifts in the EA of the $MAPbI_3$ surface region, thereby maintaining a favorable energy landscape for electron transfer from the $MAPbI_3$ bulk to $C_{60}$, as depicted in Figure 4.15b, and yielding relatively high PV performance. Therefore, all ligands that result in a favorable energy

landscape for electron transfer to occur from the $MAPbI_3$ bulk through the $MAPbI_3$ surface region to $C_{60}$ result in PV performance that equals or exceeds that of the control device.

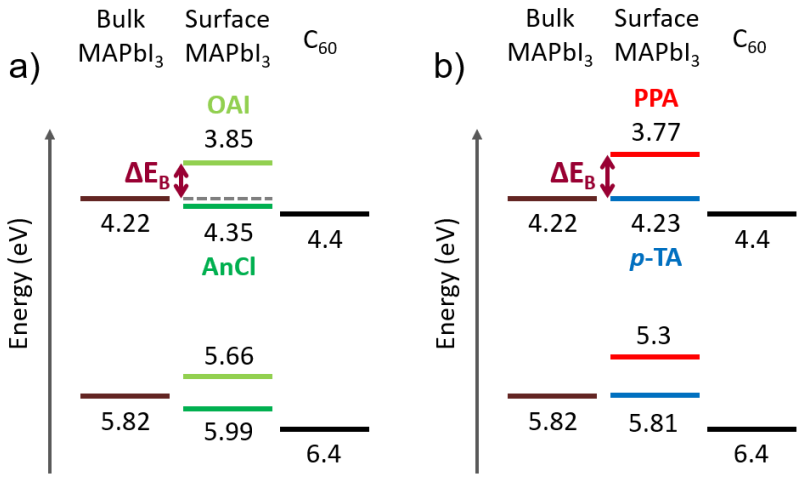


Figure 4.15 Energetic landscape of $MAPbI_3$ in the bulk of the film and at the interface with $C_{60}$ for AnCl and OAI treatment (a) and for PPA and *p*-TA treatment (b)

Notably, our results differ from some previous reports, as all these functional groups have been shown to yield increased PCEs.[91,96,97,107,121,145,146] However, we note that these differences are not unexpected and may arise due to differences in the method of ligand deposition, the surface of the $MAPbI_3$ films, the device architecture, ligand concentration,[18,109,147] or processing conditions. For example, PEAI has been used as a surface treatment in high performing PVs and applied through an IPA treatment;[18,147] however, in these examples, the devices were made in the conventional architecture with the HTL in contact with the top surface of the HP. Previous reports have indicated that PEAI treatment results in a decreased IE of $MAPbI_3$,[109] which agrees with the observation that PEAI treatment of the HP can improve PV performance through facilitating hole extraction when applied at the $MAPbI_3$/HTL interface in an n-i-p architecture.[18,147] By contrast, we are applying PEAI treatment to the $MAPbI_3$/ETL interface, this upward shift

in the IE and EA hinders electron transfer from $MAPbI_3$ to $C_{60}$ and decrease the performance in our p-i-n devices.

The improvements in PV performance observed for the CA containing ligands agree with the increased PL intensity and suggest that indeed the CA containing ligands are helping to passivate surface traps and reduce non-radiative recombination. On the other hand, the ammonium containing ligands yield similar PL intensities, yet result in large differences in PV performance. To explain why the PV performance drops significantly for OAI and PEAI, but remains at the same level as the control for AnCl, we turn to the surface energetics as measured with IPES and UPS. As we see no change in the XRD spectra upon surface modification, we expect that the ammonium containing ligands do not penetrate past the near surface region of the film. Thus, we expect that the energetics in the bulk of the $MAPbI_3$ films remain similar to the unmodified film and only the region near the surface displays the altered EA and IE. This assumption leads to the energy diagrams displayed in Figure 4.6a. Here, the OAI treated film presents an energetic barrier at the $MAPbI_3$ surface region (i.e., the electrons must pass through higher energy states), which is likely to impede electron transfer to $C_{60}$. Treatment with AnCl presents no such barrier. The presence of an energetic barrier for electron transfer to $C_{60}$ observed with OAI, and the lack of an energetic barrier with AnCl, is the most likely explanation for the significantly higher PV performance observed for the AnCl treated device.

## 4.5 Conclusions

This work clearly shows that many surface ligands will penetrate into $MAPbI_3$ when fully formed $MAPbI_3$ films are exposed to solutions of surface ligands for short

times, a finding that is often unaccounted for and which can have large implications on device performance. Ammonium containing ligands, which have been widely applied as surface ligands on HP films, are all shown to penetrate into the film with our deposition method. Importantly, the degree of ligand penetration into the HP depends on both the ligand tail group and binding group, both of which provide a useful handle for manipulating whether the ligand will remain confined to the surface. The observation that surface ligands greatly impact surface energetics has significant implications for PSC performance. These energetic changes upon ligand application are likely to result in a need to select different surface ligands based on whether the treatment will be carried out at the HP/ETL interface or HP/HTL interface. For example, ligand treatment may lead to a favorable energy landscape for hole transfer at the HP/HTL interface and an unfavorable energy landscape for electron transfer at the HP/ETL interface. Our work suggests that energetic changes upon surface ligand treatment are one of the primary reasons for the differences in PV performance observed with the different ligands. Moving forward, it will be important to identify how the ligand deposition method influences the resulting energetics, ligand penetration, optical properties and device performance. Furthermore, identifying how the ligand binding group and ligand tail work to influence the electronic structure of the treated films will help to enable more predictive control of interfacial energetics.

# CHAPTER 5. DESIGNING AMMONIUM CONTAINING SURFACE LIGANDS TO FORM SURFACE SEGREGATED MONOLAYERS

## 5.1 Introduction

Organic metal halide perovskite solar cells (PSCs) have developed significantly over the past decade, and now PSCs are the most competitive class of emerging materials for photovoltaics (PVs).[148] However, these materials have serious environmental stability issues that must be addressed, include phase separation in mixed halide perovskites,[149] light-induced degradation,[150] low tolerance to temperatures over 80 °C,[151] and halide ion migration.[152] Various strategies have been applied to improve the efficiency and stability of PSCs, such as including an additional antisolvent treatment step during processing,[153] applying nontoxic and bifunctional antisolvents,[154,155] including additives in the perovskite precursor solution,[103,156,157] and applying surface treatments to passivate defects and manipulate interface energetics.[99,158–160]

Surface passivation approaches have been applied widely to reduce defect states,[98,161] increase the charge-carrier recombination lifetime,[162,163] and improve stability.[164] Many types of surface passivating ligand layers have been introduced, including ionic liquids,[165,166] polymers,[167] small molecules,[164,168] and quantum dots (QDs).[169,170] Furthermore, these ligands have been applied using various methods, such as post-film formation treatment or incorporation of ligands into the antisolvent solution or perovskite precursor solution. Ammonium containing ligands are widely used to improve environmental stability, and numerous tail groups on the ammonium binding group have been investigated. Ammonium groups fill the A-site vacancies in the perovskite and stabilize the film surface by protecting the underlying perovskite layer from harmful

degradation reactions with oxygen, water, or the metal electrodes in the device.[16,145,171] For example, You group showed that phenylethylammonium iodide (PEAI) surface treatment reduced the surface defect density and suppressed non-radiative recombination to result in higher efficiency devices.[18] Hou group introduced *p*-phenyl dimethylammonium iodide (PDMAI) surface treatment to passivate crystallographic defects at the perovskite surface and the PDMAI treated perovskite film showed higher resistance to humidity and heat due to hydrophobic aryl core.[172]

Some reports have shown that ammonium containing surface ligands can penetrate into the perovskite, thereby converting the top layer of the 3D perovskite film into a 2D layer.[173,174] This 3D/2D hybrid perovskite structure can be more stable owing to the moisture and ionic diffusion barrier presented by the hydrophobic nature of the tail groups on the ammonium containing ligands.[173] In our previous work, we showed that all of the ammonium containing surface ligands tested penetrated into the $MAPbI_3$ thin films, albeit to varying extents.[168] Additionally, the Sargent group reported that surface treatment with ammonium containing ligands can change the dimensionality on the surface and alter the band alignment depending on the structure of the ligands.[109] The variables determining the extent of ligand penetration are important to understand to create controlled interfacial structures, for example with no, minimal, or significant ligand penetration into the perovskite. However, currently the variables impacting ligand penetration have not been thoroughly addressed. The ligand structure itself is likely to play the primary role in determining the extent of ligand penetration. For example, the size of the surface ligand and the surface energy of the ligand-capped films should help determine the extent of ligand penetration into the perovskite film. Highlighting the expected influence of ligand

size, the Gratzel group reported that bulky tert-butyl substitution on PEAI showed better device stability from moisture, and enhanced the charge extraction from the perovskite absorber to hole transport layer (HTL).[175] In addition, other variables are likely to influence ligand penetration, such as the surface roughness of the underneath film,[18] ligand concentrations,[163] solvent, exposure time, and different processing conditions. Despite the increased use of surface ligands, the degree of penetration into grain boundaries and crystalline grains, and the influence on surface energetics remain relatively unexplored and many questions remain.

In this work we show that ammonium functionalized surface ligands can be designed with bulky substituents and varying extents of fluorination to control whether they prefer to remain on the surface or penetrate into the perovskite. Namely, ammonium derivatives with bulky tails groups or fluorinated tail groups often form monolayers on $MAPbI_3$, as opposed to penetrating into the perovskite, due to size and surface energy effects, respectively. Here, we vary the surface energy by changing the extent of fluorination and the position(s) of fluorine in anilinium iodide derviatives, while the size is varied through introducing branched alkyl groups, adamantane, cyclohexanemethyl, or tert-butyl substituted aromatic units to the ammonium cation. Through a combination of XRD and angle-dependent XPS we clearly establish the extent to which the varying ligands penetrate into the perovskite; thereby, providing helpful guidelines for the design of surface ligands.

## 5.2 Experimental section

### 5.2.1 Materials

Methylammonium iodide (MAI) was purchased from Great Cell Solar and lead iodide ($PbI_2$, 99.99%) was purchased from TCI and both were used as received. Anhydrous solvents including N,N-dimethylformamide (DMF, Alfa Aesar, anhydrous, 99.8%), dimethyl sulfoxide (DMSO, Millipore SeccoSolv, 99.9%), 2-propanol (IPA, Alfa Aesar, 99.5%), and toluene (Alfa Aesar, 99.8%) were used as received.

All amines were converted to ammonium iodide form to further used as surface ligand for the perovskite layer except aniline hydride and butylamine hydroiodide. Aniline hydroiodide (TCI, 98%), 4-fluoroaniline (TCI, 98%), 2,6-difluoroaniline (TCI, 98%), 3,4,5-trifluoroaniline (TCI, 98%), butylamine hydroiodide (TCI, 97%), octylamine (Alfa Aeser, 99%), decylamine (Sigma-Aldrich, 95%), 1-adamantylamine (Sigma-Aldrich, 97%), cyclohexanemethylamine (Sigma-Aldrich, 98%), 4-tert-butylaniline (TCI, 98%), 3,5-di-tert-butylaniline (TCI, 98%) were selected as surface ligand.

Ammonium salt synthesis: the amine containing surface ligand and hydroiodic acid (1:1 mol) ratio were stirred in ethanol at 0 °C for 2h. The resulting solution was dried at 60 °C with a rotary evaporator to remove the solvents. The product was dissolved in ethanol and recrystallized from diethyl ether. The product was rinsed three times with diethyl ether and dried in a vacuum oven at 60 °C overnight before use.

### 5.2.2 Materials characterization

$MAPbI_3$ film preparation: Non-patterned ITO coated glass substrates (15 Ω/□) were sequentially sonicated in aqueous detergent (sodium dodecyl sulfate, Sigma-Aldrich), deionized water, acetone, and 2-propanol each for 10 min. After drying with nitrogen, the substrates were exposed to UV-ozone treatment for 10 min to remove organic contaminants and then transferred into the nitrogen-filled glovebox (<0.1 ppm of $O_2$ and $H_2O$). For the $MAPbI_3$ films, 461 mg of $PbI_2$, 159 mg of MAI, and 78 mg of DMSO (1:1:1 molar ratio) were dissolved in 600 mg of DMF and stirred at room temperature for 1 h before use in the nitrogen-filled glovebox. On the cleaned ITO substrate, 80 μL of $MAPbI_3$ solution was deposited and spun-cast at 1000 rpm for 5 s followed by 3000 rpm for 80 s. 100 μL of toluene was dropped on the spinning substrate after 10 s of reaching 3000 rpm, resulting in the formation of transparent films that were then annealed on a hot plate at 100 °C for 10 min. After cool down, 100 μL of surface ligand solution in IPA (2 mg/mL) was then deposited on the dark $MAPbI_3$ films and left to sit for 5 s before spinning at 4000 rpm for 30 s with a 2 s ramp. For time dependent measurement, ligand solution was kept longer before spinning. To remove excess unbound ligands, the substrates were rinsed with toluene (3 x 100 μL aliquots during spinning).

Material characterization measurements including XPS, UPS, IPES, XRD, UV-vis, and PL were used as mentioned in earlier chapters.

## 5.3 Results and discussion

### 5.3.1 Surface ligand penetration

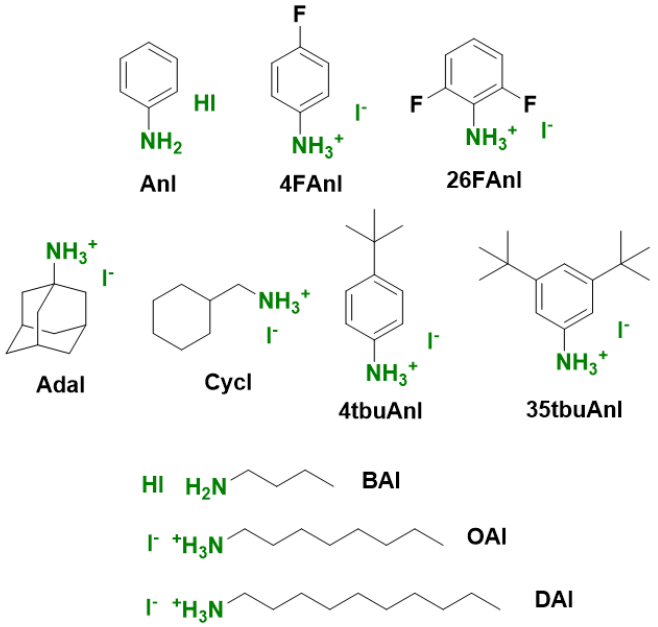


Figure 5.1 Surface ligands used to treat $MAPbI_3$ film

The $MAPbI_3$ thin films were treated with the surface ligands shown in Figure 5.1 to determine the relative ligand penetration with the different tail groups. Surface treatment was performed through coating method with IPA solution containing the surface ligands. After surface treatment, rinsing the substrates with toluene solution was performed to remove unbound ligands. A control $MAPbI_3$ film was treated in the same way without any surface ligand. Previously, we found all ammonium functional groups of surface ligands, AnCl, PEAI, and OAI penetrate the $MAPbI_3$ films, but showed significant different energetics and PV performance.[168] The surface ligands shown in Figure 5.1 can be categorized into 3 types of tail groups including three variations of tail groups including aryl groups with varying extents of fluorination, bulky groups of varying size, and linear

alkyl groups with varying length to probe how there variables influence the ligand penetration.

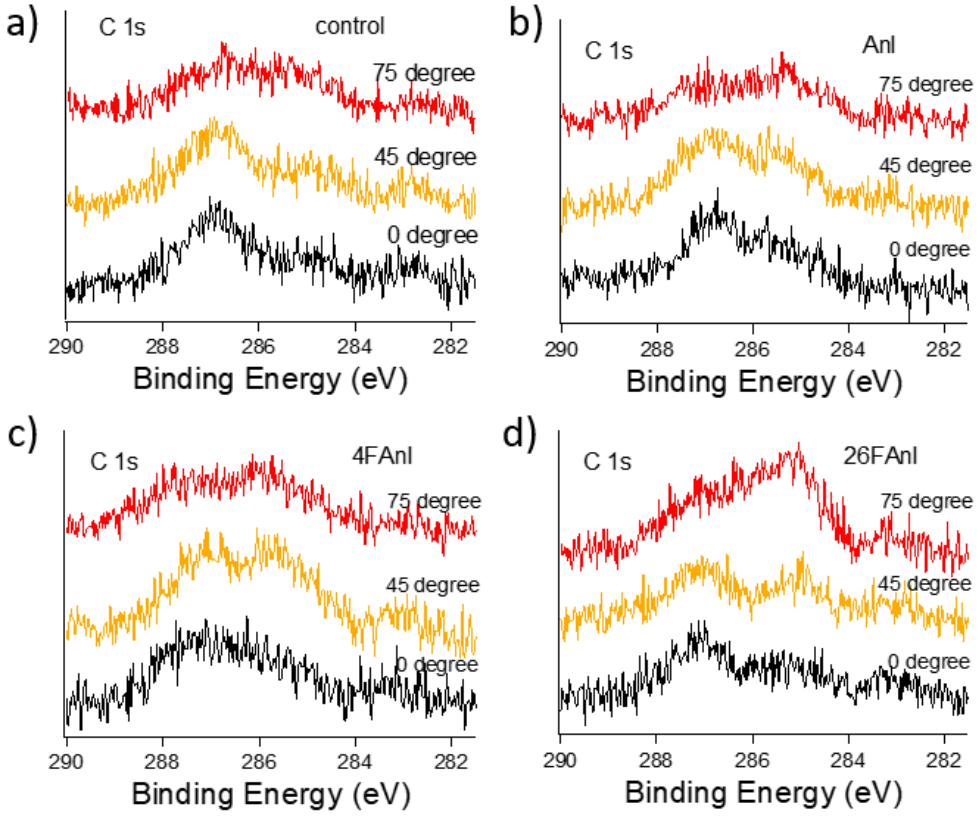


Figure 5.2 Angle dependent XPS of the C 1s region at 0, 45, and 75 ° for a) untreated $MAPbI_3$, b) AnI, c) 4FAnI, and d) 26FAnI

Ammonium group can fill the A-site vacancies on the surface of the perovskite crystal or displace surface MA molecules as mentioned earlier in the chapter. To probe the ligand penetration we conducted angle dependent XPS measurements. To vary the probing depth we changed the angles between the normal of the sample and the analyzer by rotating the sample stage. Three different electron take-off angles were measured, 0, 45 and 75 °

and the probing depth is varied from approximately 6 to 8 nm at 0 ° to only 1.5 to 2 nm at 75 °.

Figure 5.2 shows the C 1s intensity for $MAPbI_3$ films modified with aryl ammonium group ligands and control $MAPbI_3$. Ammonium group surface ligands used in this work do not have a unique element, i.e., an element that is in the ligand and not in $MAPbI_3$, other than fluorine and the F peaks are typically below our limit of detection, thus we compared C 1s intensity between the takeoff angles. In control $MAPbI_3$ films, MA C appears at a binding energy around 287 eV, whereas non-MA C appears at around 285.5 eV. This shift is because MA is positively charged as discussed in chapter 4. According to the spectra, AnI showed minimal intensity ratio change between MA C to non-MA C compared to the control, as shown in Figure 5.2b.

In our earlier work, phenylphosphonic acid (PPA) modified $MAPbI_3$ showed only small change of O 1s peaks throughout all three electron take-off angles indicating penetrate $MAPbI_3$ film as opposed to forming a surface layer.[168] On the other hand, octylphosphonic acid (OPA) modified $MAPbI_3$ showed increased O 1s peaks at 75 ° suggesting OPA is more surface localized. Based on our earlier result, we hypothesized that the halide-π interaction may be responsible for the greater penetration of PPA as compared to OPA. However, compare to AnI in Figure 5.2b and BAI in Figure 5.4a, larger non-MA C for BAI is observed at all angles, which indicate halide-π interaction may not the major source to determine the surface ligand penetrate perovskite film. However, difference surface environment like terminal group or the roughness of the film and individual processing conditions such as solvents, and ligand exposure time may influence the ligand penetration.

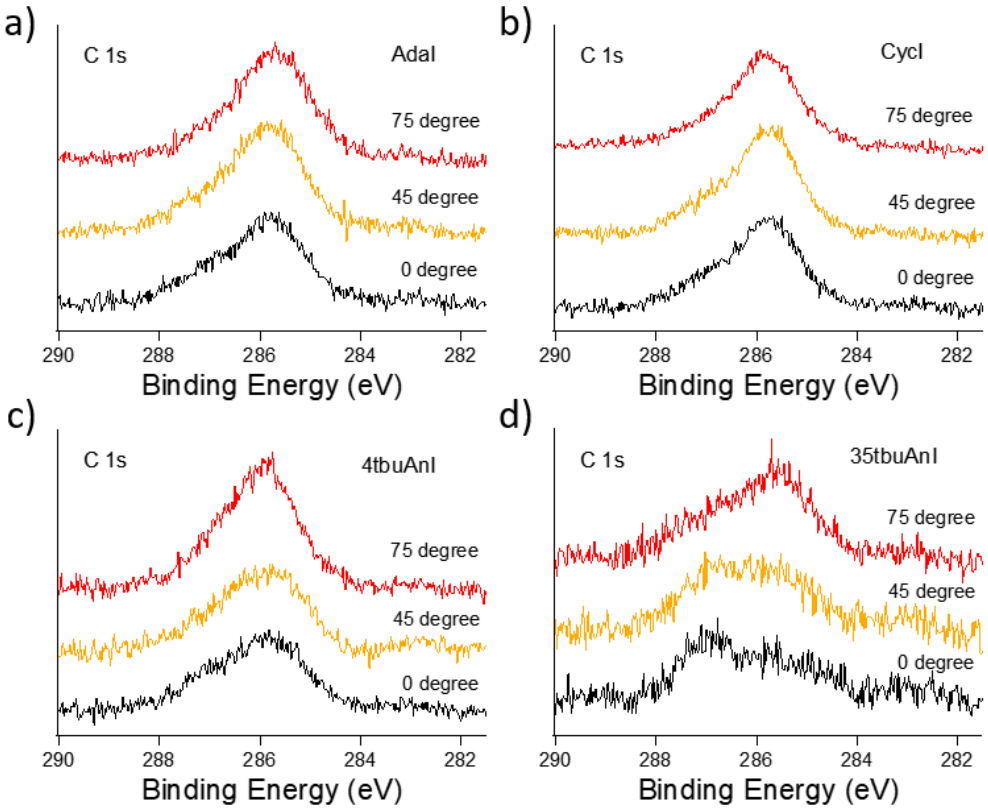


Figure 5.3 Angle dependent XPS of the C 1s region at 0, 45, and 75 ° for a) AdaI, b) CycI, c) 4tbuAnI, and d) 35tbuAnI treated $MAPbI_3$ films

We further explored the role of bulkiness on the tail group ammonium containing surface ligand penetration into the $MAPbI_3$. First, we selected the adamantane group which has been used in various organic electronic research due to its rigid, hydrophobic, bulky structure, and versatile functionalization on hydrocarbons.[176–178] The Gratzel group reported post-treatment of adamantane and adamantylamine group can successfully abate the electronic defects within the bulk and the surface and showed enhanced PV performance and operational stability of PSCs.[179] We also include cyclohexanemethyl and tert-butyl functionalized AnI in our investigation of tail group size effects. As shown in Figure 5.3, non-MA C:MA C ratios at all angles increased for all four of the $MAPbI_3$ films

that were treated with bulky ammonium containing surface ligands as compared to that of the control $MAPbI_3$ film. Interestingly we found depending on the position and the number of the tert-butyl group, the extent of ligand penetration significantly changes. Figure 5.3c 4tbuAnI shows gradual increase of non-MA C around 285.5 eV from bulk of 0 ° to more surface of 75 ° versus AdaI and CycI present constant non-MA C:MA C ratios at all angles. In contrast with 4tbuAnI, Figure 5.3d illustrates that 35tbuAnI does show a big change in the non-MA C:MA C ratios between 45 ° to 75 °. These measurements clearly explain that the size of the ligands followed by the position and the number of the bulky tail group significantly influence whether the ligand is confined to the surface or penetrates the $MAPbI_3$ film.

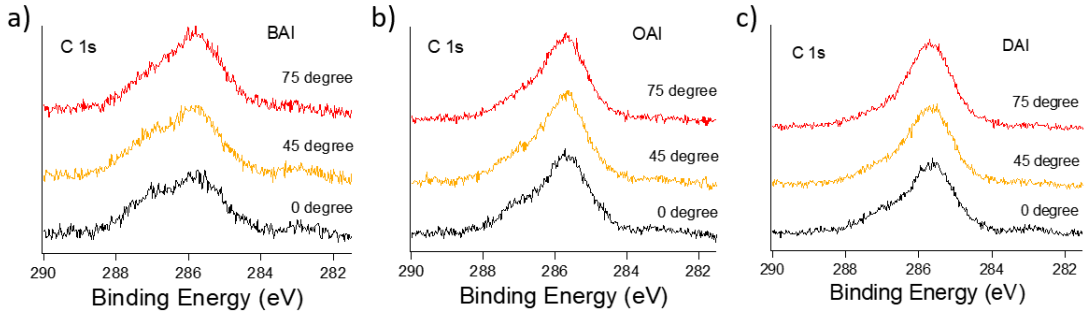


Figure 5.4 Angle dependent XPS of the C 1s region at 0, 45, and 75 ° for a) BAI, b) OAI, and d) DAI treated $MAPbI_3$ films

Figure 5.4 shows the angle dependent XPS of the C 1s region of alkyl tail group ammonium containing ligands. Increased non-MA C:MA C ratios at all angles are observed regardless of the length of alkyl chain. Additionally, larger non-MA C:MA C ratio change supports that longer carbon chain at OAI and DAI shows non-MA C peak increase around 285.5 eV compare to BAI. This XPS data indicates that all alkyl tail group ammonium containing ligands penetrate the $MAPbI_3$ film, which is consistent with previous work.[168]

Except the C 1s region, N 1s, Pb 4f, I $3d_{5/2}$ regions are measured for untreated and all surface ligand treated $MAPbI_3$ films at all angles. Here, the I:Pb ratio is between 2.9 and 3.1 and none of regions show peak shift due to surface charging from the angle-dependent XPS samples.

### 5.3.2 Crystal structure characterization

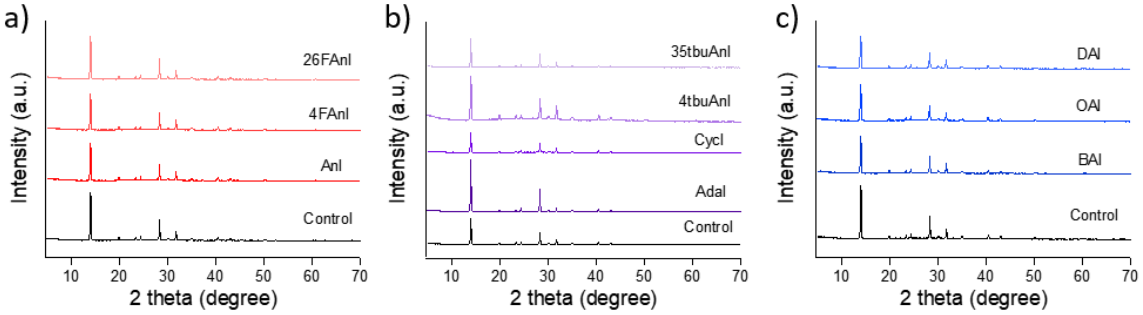


Figure 5.5 XRD spectra comparison between untreated $MAPbI_3$ and a) aryl group, b) bulky group, and c) alkyl group

The structure of the ligand treated, and untreated $MAPbI_3$ film is characterized by XRD. As shown in Figure 5.5, aryl, bulky, and alkyl tail group ammonium containing ligands treated perovskite film exhibit no extra diffraction peaks. These XRD spectra suggest they do not penetrate perovskite film enough to change the crystal structures of bulk perovskite even though they show ligand penetration on angle dependent XPS measurements.

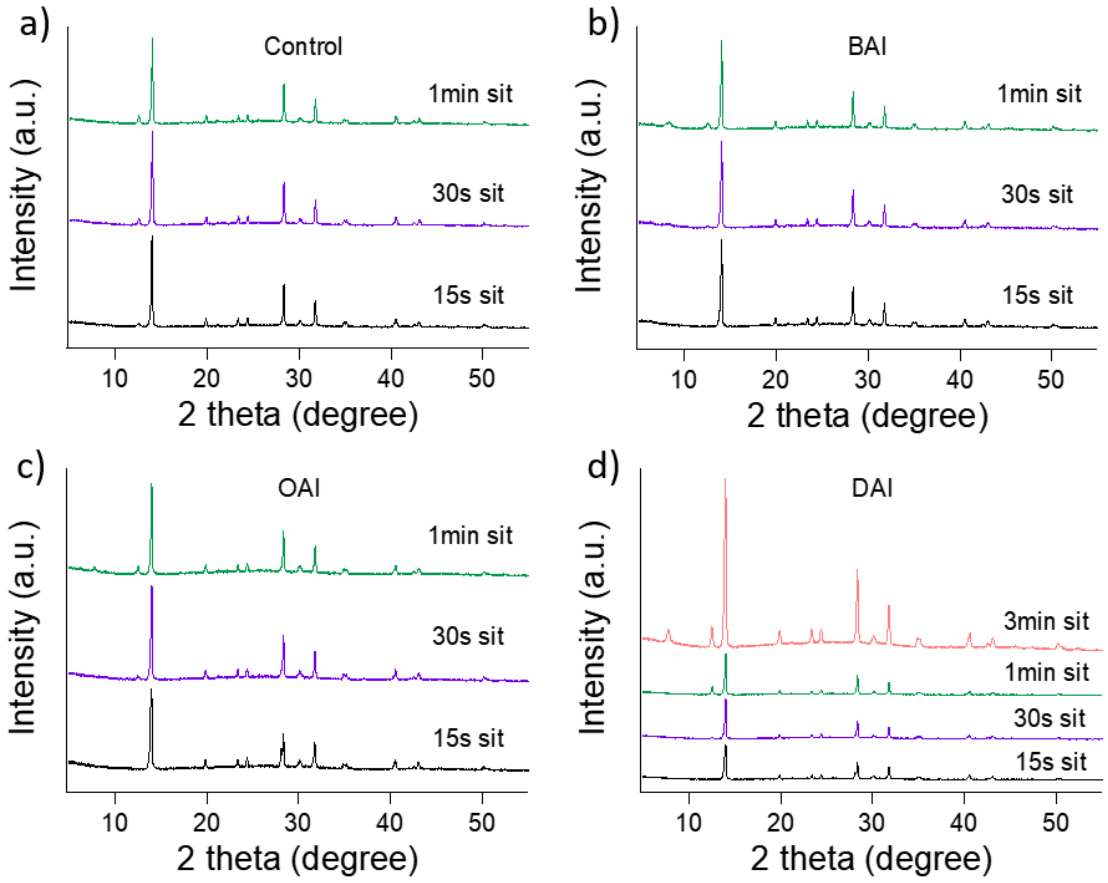


Figure 5.6 XRD spectra comparison between a) untreated $MAPbI_3$, b) BAI, c) OAI, and c) DAI of surface ligand time exposure

We further investigated structural characteristic of surface ligand treated $MAPbI_3$ film by changing the time of ligand exposure to observe when these surface ligands play a role in changing the crystal structure of $MAPbI_3$. From the comparison of XRD patterns of control $MAPbI_3$ film, as shown in Figure 5.5, new emerging peak at $2\theta = 12.7$ is observed with 15 s of IPA treatment in Figure 5.6a. Similar to previous report, this diffraction peak corresponds to $PbI_2$ which is a product of $MAPbI_3$ decomposition.[180,181] The use of IPA as a solvent for post-synthetic treatment of perovskite films is comparable with previous reports,[18,125] however, longer treatment of IPA decomposes $MAPbI_3$ film since IPA

dissolves MAI.[182] The intensity of the $PbI_2$ peak increases with longer IPA treatment, as shown in Figure 5.6a, which supports that degradation of $MAPbI_3$ is occurring. For the surface ligand treated samples, the $PbI_2$ peak is not observed at 15 s of IPA treatment, which explains surface ligand slows down the degradation process of $MAPbI_3$ film. The diffraction peak at $2\theta$ = 14.0 corresponds to (001) crystallographic planes of the 3D perovskite and this peak did not show peak shifts throughout longer ligand exposure. When the film is treated with BAI for 30 s, the XRD patterns show a new peak at around $2\theta$ = 7.9, which is attributed to the $(BA)_2(MA)_{n-1}Pb_nI_{3n+1}$ family of layered compounds[183–185] as shown in Figure 5.6b. This lower dimensional peak growth is also found when the film is treated with OAI for 1 min in Figure 5.6c, which is in agreement with previous reports.[173,186] Interestingly, DAI treated films do not show any peak less than $2\theta$ = 10 until the treatment time reaches 3 min in Figure 5.6d. This XRD data indicates that the longer alkyl chain of DAI makes it hard to fit in the perovskite crystal structure to make low dimensional perovskite, which organic molecular cations act as a spacer between the perovskite layers.[187]

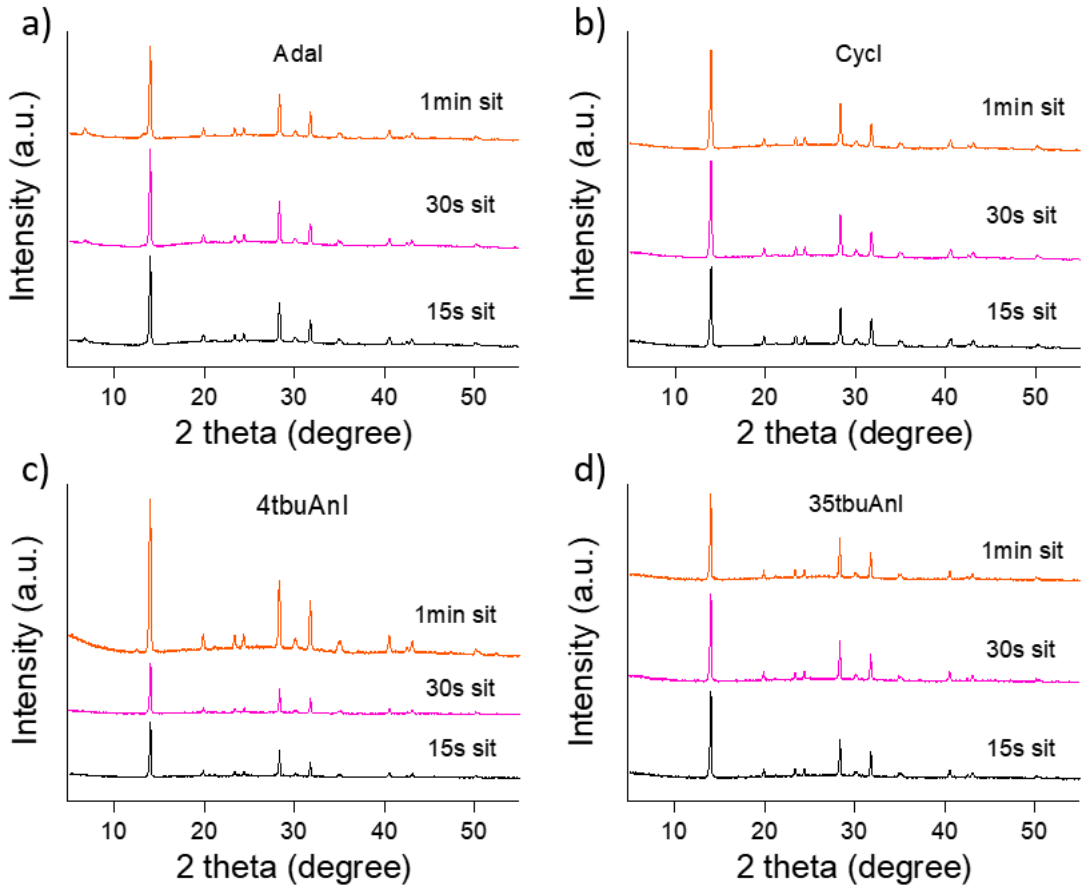


Figure 5.7 XRD spectra comparison between a) AdaI, b) CycI, c) 4tbuAnI, and d) 35tbuAnI of surface ligand time exposure

Figure 5.7 presents XRD patterns of bulky tail group ammonium containing ligand treated $MAPbI_3$ film. Interestingly, XRD spectra of AdaI treated film show emerging intensity of peak at $2\theta = 6.7$ starting from 15s treatment in Figure 5.7a versus CycI treated film do not show any additional peak until 1min of treatment in Figure 5.7b. Importantly, both 4tbuAnI and 35tbuAnI treated films do not show any reduced dimensionality peak shifts, however, emerging $PbI_2$ peak at $2\theta = 12.7$ is observed with 1 min treatment of 4tbuAnI as shown in Figure 5.7c. Compare to control XRD spectra in Figure 5.6a, this data clearly confirms that tert-butyl group inhibits the ligand penetration to bulk of the $MAPbI_3$

film which is in agreement with angle dependent XPS measurement in Figure 5.3c and d. Notably, on the basis of previous results,[175] increased steric hindrance from tert-butyl substitution on PEAI did not show extra low dimensional diffraction peak further support prevention of ligand penetration to bulk of the film. As shown in Figure 5.3c and d, time dependent XRD results indicate 4tbuAnI surface treatment do not go into bulk of the $MAPbI_3$ film to the extent needed to change the crystal structure enough to show a change in the XRD spectra.

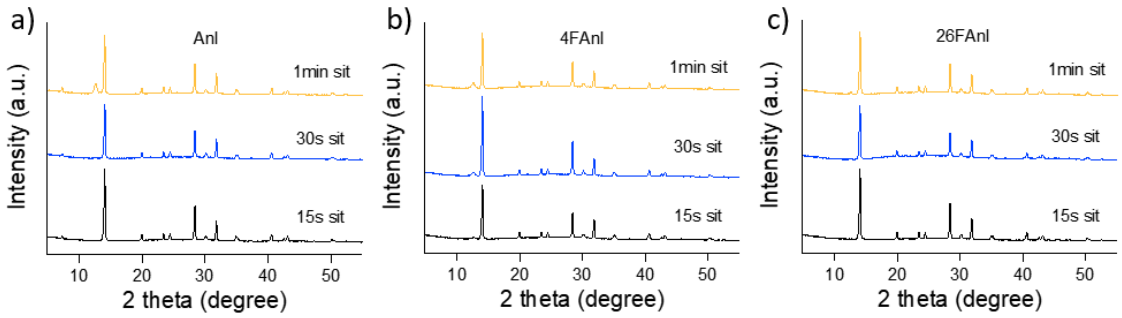


Figure 5.8 XRD spectra comparison between a) AnI, b) 4FAnI, and c) 26FAnI of surface ligand time exposure

We further studied structural characteristic of aryl tail group treated $MAPbI_3$ film by changing the time of the ligand exposure, as shown in Figure 5.8. AnI treated $MAPbI_3$ film show constant intensity of peak at $2\theta = 7.2$ starting from 15s treatment in Figure 5.8a. On the other hand, peak around $2\theta = 7.2$ is not observed with additional fluorine in anilinium iodide derivatives, 4FAnI, and 26FAnI, as shown in Figure 5.8b and c. Furthermore, $PbI_2$ peak at $2\theta = 12.7$ is not observed from 30s treatment 26FAnI and emerging when reach to 1min suggest that additional hydrophobic fluorine successfully delay the $MAPbI_3$ degradation process.

# CHAPTER 6. CONCLUSIONS AND FUTURE OUTLOOK

In this work, we have optimized the $MAPbI_3$-based PSCs and studied optical and electrical properties of the HTL materials and perovskites. We introduced a new family of triarylaminoethynyl silane molecules as HTLs to investigate how the PV performance depends on the IE of the HTL and provide a new and versatile HTL materials platform. We further expanded to a series of eleven different HTL materials with various IEs. We found that the idea HTL IE range for maximum PV efficiency is dependent on the perovskite processing conditions.

Next, we investigated a series of surface ligand binding groups and systematically probe the stability of the bound surface ligands, how they influence PL properties, film stability, and PV device performance. Here, surface ligands with different binding groups are investigated to determine their extent of surface coverage, whether they form a surface monolayer or penetrate the perovskite and how they influence material energetics. It was found that surface ligands can significantly shift the IE and EA from UPS and IPES measurements and these changes in surface energetics substantially impact the PSC performances. Furthermore, we selected ammonium functionalized surface ligands with bulky substituents and varying extents of fluorination to control whether they prefer to remain on the surface or penetrate into the perovskites. We observed hydrophobic fluorination on molecule can effectively prevent surface ligand from penetration into bulk of $MAPbI_3$ film and size of the ligands can influence whether the ligand is confined to the surface or penetrates the $MAPbI_3$ film.

In order to understand what determines performance of the device, we need to observe various material properties itself and look more carefully at interfaces with

neighboring layers at the same time, as energy level alignment and electronic properties at interfaces dictate materials and device properties. Although many groups have investigated the properties of the perovskite materials, further fundamental understanding of crystal formation, defect states, optical, electronic properties, and interfacial energetics, and improvement of device performance and stability is needed in the perovskite research community.

# REFERENCES


(1) Kojima, A.; Teshima, K.; Shirai, Y.; Miyasaka, T. Organometal Halide Perovskites as Visible-Light Sensitizers for Photovoltaic Cells. *J. Am. Chem. Soc.* **2009**, *131* (17), 6050–6051. https://doi.org/10.1021/ja809598r.

(2) Im, J.-H.; Lee, C.-R.; Lee, J.-W.; Park, S.-W.; Park, N.-G. 6.5% Efficient Perovskite Quantum-Dot-Sensitized Solar Cell. *Nanoscale* **2011**, *3* (10), 4088. https://doi.org/10.1039/c1nr10867k.

(3) Kim, H.-S.; Lee, C.-R.; Im, J.-H.; Lee, K.-B.; Moehl, T.; Marchioro, A.; Moon, S.-J.; Humphry-Baker, R.; Yum, J.-H.; Moser, J. E.; et al. Lead Iodide Perovskite Sensitized All-Solid-State Submicron Thin Film Mesoscopic Solar Cell with Efficiency Exceeding 9%. *Sci. Rep.* **2012**, *2* (1), 591. https://doi.org/10.1038/srep00591.

(4) Emery, K. Best Research-Cell Efficiencies (NREL Chart). *NREL chart*. 2018, p version 10-30-2017.

(5) Ko, Y.-H.; Prabhakaran, P.; Jalalah, M.; Lee, S.-J.; Lee, K.-S.; Park, J.-G. Correlating Nano Black Spots and Optical Stability in Mixed Halide Perovskite Quantum Dots. *J. Mater. Chem. C* **2018**, *6* (29), 7803–7813. https://doi.org/10.1039/C8TC01040D.

(6) Wu, Y.; Chen, W.; Chen, G.; Liu, L.; He, Z.; Liu, R. The Impact of Hybrid Compositional Film/Structure on Organic–Inorganic Perovskite Solar Cells. *Nanomaterials* **2018**, *8* (6), 356. https://doi.org/10.3390/nano8060356.

(7) Gholipour, S.; Ali, A. M.; Correa-Baena, J.-P.; Turren-Cruz, S.-H.; Tajabadi, F.; Tress, W.; Taghavinia, N.; Grätzel, M.; Abate, A.; De Angelis, F.; et al. Globularity-Selected Large Molecules for a New Generation of Multication Perovskites. *Adv. Mater.* **2017**, *29* (38), 1702005. https://doi.org/10.1002/adma.201702005.

(8) De Wolf, S.; Holovsky, J.; Moon, S.-J.; Löper, P.; Niesen, B.; Ledinsky, M.; Haug, F.; Yum, J.; Ballif, C. Organometallic Halide Perovskites: Sharp Optical Absorption Edge and Its Relation to Photovoltaic Performance. *J. Phys. Chem. Lett.* **2014**, *5* (6), 1035–1039. https://doi.org/10.1021/jz500279b.

(9) Urbach, F. The Long-Wavelength Edge of Photographic Sensitivity and of the Electronic Absorption of Solids. *Phys. Rev.* **1953**, *92* (5), 1324–1324. https://doi.org/10.1103/PhysRev.92.1324.

(10) Yang, W.; Yao, Y.; Guo, P.; Sun, H.; Luo, Y. Optimum Driving Energy for Achieving Balanced Open-Circuit Voltage and Short-Circuit Current Density in Organic Bulk Heterojunction Solar Cells. *Phys. Chem. Chem. Phys.* **2018**, *20* (47), 29866–29875. https://doi.org/10.1039/C8CP05145C.

(11) Varadwaj, P. R.; Varadwaj, A.; Marques, H. M.; Yamashita, K. Significance of

Hydrogen Bonding and Other Noncovalent Interactions in Determining Octahedral Tilting in the CH3NH3PbI3 Hybrid Organic-Inorganic Halide Perovskite Solar Cell Semiconductor. *Sci. Rep.* **2019**, *9* (1), 50. https://doi.org/10.1038/s41598-018-36218-1.

(12) Svane, K. L.; Forse, A. C.; Grey, C. P.; Kieslich, G.; Cheetham, A. K.; Walsh, A.; Butler, K. T. How Strong Is the Hydrogen Bond in Hybrid Perovskites? *J. Phys. Chem. Lett.* **2017**, *8* (24), 6154–6159. https://doi.org/10.1021/acs.jpclett.7b03106.

(13) Latini, A.; Gigli, G.; Ciccioli, A. A Study on the Nature of the Thermal Decomposition of Methylammonium Lead Iodide Perovskite, CH 3 NH 3 PbI 3 : An Attempt to Rationalise Contradictory Experimental Results. *Sustain. Energy Fuels* **2017**, *1* (6), 1351–1357. https://doi.org/10.1039/C7SE00114B.

(14) Bækbo, M. J.; Hansen, O.; Chorkendorff, I.; Vesborg, P. C. K. Deposition of Methylammonium Iodide via Evaporation – Combined Kinetic and Mass Spectrometric Study. *RSC Adv.* **2018**, *8* (52), 29899–29908. https://doi.org/10.1039/C8RA04851G.

(15) Ma, L.; Guo, D.; Li, M.; Wang, C.; Zhou, Z.; Zhao, X.; Zhang, F.; Ao, Z.; Nie, Z. Temperature-Dependent Thermal Decomposition Pathway of Organic–Inorganic Halide Perovskite Materials. *Chem. Mater.* **2019**, *31* (20), 8515–8522. https://doi.org/10.1021/acs.chemmater.9b03190.

(16) Zhao, L.; Kerner, R. A.; Xiao, Z.; Lin, Y. L.; Lee, K. M.; Schwartz, J.; Rand, B. P. Redox Chemistry Dominates the Degradation and Decomposition of Metal Halide Perovskite Optoelectronic Devices. *ACS Energy Lett.* **2016**, *1* (3), 595–602. https://doi.org/10.1021/acsenergylett.6b00320.

(17) Nh, C. H.; Raga, S. R.; Ono, L. K.; Qi, P. Y.; Yabing, S. Thermal Degradation of CH3NH3PbI3 Perovskite into NH3 and CH3I Gases Observed by Coupled Thermogravimetry - Mass Spectrometry Analysis. **2016**. https://doi.org/: 10.1039/c6ee02016j.

(18) Jiang, Q.; Zhao, Y.; Zhang, X.; Yang, X.; Chen, Y.; Chu, Z.; Ye, Q.; Li, X.; Yin, Z.; You, J. Surface Passivation of Perovskite Film for Efficient Solar Cells. *Nat. Photonics* **2019**, *13* (7), 460–466. https://doi.org/10.1038/s41566-019-0398-2.

(19) Li, S.; Fan, K.; Cui, Y.; Leng, S.; Ying, Y.; Zou, W.; Liu, Z.; Li, C.-Z.; Yao, K.; Huang, H. Unravelling the Mechanism of Ionic Fullerene Passivation for Efficient and Stable Methylammonium-Free Perovskite Solar Cells. *ACS Energy Lett.* **2020**, *5* (6), 2015–2022. https://doi.org/10.1021/acsenergylett.0c00871.

(20) Schulz, P.; Cahen, D.; Kahn, A. Halide Perovskites: Is It All about the Interfaces? *Chem. Rev.* **2019**, *119* (5), 3349–3417. https://doi.org/10.1021/acs.chemrev.8b00558.

(21) Chen, H.; Wei, Q.; Saidaminov, M. I.; Wang, F.; Johnston, A.; Hou, Y.; Peng, Z.; Xu, K.; Zhou, W.; Liu, Z.; et al. Efficient and Stable Inverted Perovskite Solar Cells Incorporating Secondary Amines. *Adv. Mater.* **2019**, *31* (46), 1903559. https://doi.org/10.1002/adma.201903559.

(22) Bella, F.; Griffini, G.; Correa-Baena, J.-P.; Saracco, G.; Gratzel, M.; Hagfeldt, A.; Turri, S.; Gerbaldi, C. Improving Efficiency and Stability of Perovskite Solar Cells with Photocurable Fluoropolymers. *Science (80-. ).* **2016**, *354* (6309), 203–206. https://doi.org/10.1126/science.aah4046.

(23) Rolston, N.; Bennett-Kennett, R.; Schelhas, L. T.; Luther, J. M.; Christians, J. A.; Berry, J. J.; Dauskardt, R. H. Comment on "Light-Induced Lattice Expansion Leads to High-Efficiency Perovskite Solar Cells." *Science (80-. ).* **2020**, *368* (6488), eaay8691. https://doi.org/10.1126/science.aay8691.

(24) Kim, H.-S.; Park, N.-G. Parameters Affecting I – V Hysteresis of CH 3 NH 3 PbI 3 Perovskite Solar Cells: Effects of Perovskite Crystal Size and Mesoporous TiO 2 Layer. *J. Phys. Chem. Lett.* **2014**, *5* (17), 2927–2934. https://doi.org/10.1021/jz501392m.

(25) Song, J.; Liu, L.; Wang, X.-F.; Chen, G.; Tian, W.; Miyasaka, T. Highly Efficient and Stable Low-Temperature Processed ZnO Solar Cells with Triple Cation Perovskite Absorber. *J. Mater. Chem. A* **2017**, *5* (26), 13439–13447. https://doi.org/10.1039/C7TA03331A.

(26) Ma, J.; Su, J.; Lin, Z.; Zhou, L.; He, J.; Zhang, J.; Liu, S.; Chang, J.; Hao, Y. Improve the Oxide/Perovskite Heterojunction Contact for Low Temperature High Efficiency and Stable All-Inorganic CsPbI2Br Perovskite Solar Cells. *Nano Energy* **2020**, *67*, 104241. https://doi.org/10.1016/j.nanoen.2019.104241.

(27) Yang, D.; Yang, R.; Wang, K.; Wu, C.; Zhu, X.; Feng, J.; Ren, X.; Fang, G.; Priya, S.; Liu, S. High Efficiency Planar-Type Perovskite Solar Cells with Negligible Hysteresis Using EDTA-Complexed SnO2. *Nat. Commun.* **2018**, *9* (1), 3239. https://doi.org/10.1038/s41467-018-05760-x.

(28) Smith, J. A.; Game, O. S.; Bishop, J. E.; Spooner, E. L. K.; Kilbride, R. C.; Greenland, C.; Jayaprakash, R.; Alanazi, T. I.; Cassella, E. J.; Tejada, A.; et al. Rapid Scalable Processing of Tin Oxide Transport Layers for Perovskite Solar Cells. *ACS Appl. Energy Mater.* **2020**, *3* (6), 5552–5562. https://doi.org/10.1021/acsaem.0c00525.

(29) Zhang, W.; Xiong, J.; Li, J.; Daoud, W. A. Mechanism of Water Effect on Enhancing the Photovoltaic Performance of Triple-Cation Hybrid Perovskite Solar Cells. *ACS Appl. Mater. Interfaces* **2019**, *11* (13), 12699–12708. https://doi.org/10.1021/acsami.8b20264.

(30) Huang, J.; Tan, S.; Lund, P. D.; Zhou, H. Impact of H 2 O on Organic–Inorganic Hybrid Perovskite Solar Cells. *Energy Environ. Sci.* **2017**, *10* (11), 2284–2311. https://doi.org/10.1039/C7EE01674C.

(31) Chiang, C.-H.; Wu, C.-G. A Method for the Preparation of Highly Oriented MAPbI 3 Crystallites for High-Efficiency Perovskite Solar Cells to Achieve an 86% Fill Factor. *ACS Nano* **2018**, *12* (10), 10355–10364. https://doi.org/10.1021/acsnano.8b05731.

(32) Borchert, J.; Levchuk, I.; Snoek, L. C.; Rothmann, M. U.; Haver, R.; Snaith, H. J.;

Brabec, C. J.; Herz, L. M.; Johnston, M. B. Impurity Tracking Enables Enhanced Control and Reproducibility of Hybrid Perovskite Vapor Deposition. *ACS Appl. Mater. Interfaces* **2019**, *11* (32), 28851–28857. https://doi.org/10.1021/acsami.9b07619.

(33) Lee, J.-W.; Dai, Z.; Lee, C.; Lee, H. M.; Han, T.; De Marco, N.; Lin, O.; Choi, C. S.; Dunn, B.; Koh, J.; et al. Tuning Molecular Interactions for Highly Reproducible and Efficient Formamidinium Perovskite Solar Cells via Adduct Approach. *J. Am. Chem. Soc.* **2018**, *140* (20), 6317–6324. https://doi.org/10.1021/jacs.8b01037.

(34) Jeon, N. J.; Noh, J. H.; Kim, Y. C.; Yang, W. S.; Ryu, S.; Seok, S. Il. Solvent Engineering for High-Performance Inorganic–Organic Hybrid Perovskite Solar Cells. *Nat. Mater.* **2014**, *13* (9), 897–903. https://doi.org/10.1038/nmat4014.

(35) Boehm, A. M.; Wieser, J.; Butrouna, K.; Graham, K. R. A New Photon Source for Ultraviolet Photoelectron Spectroscopy of Organic and Other Damage-Prone Materials. *Org. Electron.* **2017**, *41*, 9–16. https://doi.org/10.1016/j.orgel.2016.11.032.

(36) Bi, D.; Yi, C.; Luo, J.; Décoppet, J.-D.; Zhang, F.; Zakeeruddin, S. M.; Li, X.; Hagfeldt, A.; Grätzel, M. Polymer-Templated Nucleation and Crystal Growth of Perovskite Films for Solar Cells with Efficiency Greater than 21%. *Nat. Energy* **2016**, *1* (10), 16142. https://doi.org/10.1038/nenergy.2016.142.

(37) Yang, W. S.; Park, B.-W.; Jung, E. H.; Jeon, N. J.; Kim, Y. C.; Lee, D. U.; Shin, S. S.; Seo, J.; Kim, E. K.; Noh, J. H.; et al. Iodide Management in Formamidinium-Lead-Halide–Based Perovskite Layers for Efficient Solar Cells. *Science (80-. ).* **2017**, *356* (6345), 1376–1379. https://doi.org/10.1126/science.aan2301.

(38) Yang, W. S.; Noh, J. H.; Jeon, N. J.; Kim, Y. C.; Ryu, S.; Seo, J.; Seok, S. I. High-Performance Photovoltaic Perovskite Layers Fabricated through Intramolecular Exchange. *Science (80-. ).* **2015**, *348* (6240), 1234–1237. https://doi.org/10.1126/science.aaa9272.

(39) Shao, Y.; Xiao, Z.; Bi, C.; Yuan, Y.; Huang, J. Origin and Elimination of Photocurrent Hysteresis by Fullerene Passivation in CH3NH3PbI3 Planar Heterojunction Solar Cells. *Nat. Commun.* **2014**, *5* (1), 5784. https://doi.org/10.1038/ncomms6784.

(40) Song, D.; Wei, D.; Cui, P.; Li, M.; Duan, Z.; Wang, T.; Ji, J.; Li, Y.; Mbengue, J. M.; Li, Y.; et al. Dual Function Interfacial Layer for Highly Efficient and Stable Lead Halide Perovskite Solar Cells. *J. Mater. Chem. A* **2016**, *4* (16), 6091–6097. https://doi.org/10.1039/C6TA00577B.

(41) Polander, L. E.; Pahner, P.; Schwarze, M.; Saalfrank, M.; Koerner, C.; Leo, K. Hole-Transport Material Variation in Fully Vacuum Deposited Perovskite Solar Cells. *APL Mater.* **2014**, *2* (8), 081503. https://doi.org/10.1063/1.4889843.

(42) Cho, K. T.; Trukhina, O.; Roldán-Carmona, C.; Ince, M.; Gratia, P.; Grancini, G.; Gao, P.; Marszalek, T.; Pisula, W.; Reddy, P. Y.; et al. Molecularly Engineered Phthalocyanines as Hole-Transporting Materials in Perovskite Solar Cells Reaching

Power Conversion Efficiency of 17.5%. *Adv. Energy Mater.* **2017**, *7* (7), 1601733. https://doi.org/10.1002/aenm.201601733.

(43) Xu, B.; Sheibani, E.; Liu, P.; Zhang, J.; Tian, H.; Vlachopoulos, N.; Boschloo, G.; Kloo, L.; Hagfeldt, A.; Sun, L. Carbazole-Based Hole-Transport Materials for Efficient Solid-State Dye-Sensitized Solar Cells and Perovskite Solar Cells. *Adv. Mater.* **2014**, *26* (38), 6629–6634. https://doi.org/10.1002/adma.201402415.

(44) Cheng, M.; Xu, B.; Chen, C.; Yang, X.; Zhang, F.; Tan, Q.; Hua, Y.; Kloo, L.; Sun, L. Phenoxazine-Based Small Molecule Material for Efficient Perovskite Solar Cells and Bulk Heterojunction Organic Solar Cells. *Adv. Energy Mater.* **2015**, *5* (8), 1401720. https://doi.org/10.1002/aenm.201401720.

(45) Sin, D. H.; Ko, H.; Jo, S. B.; Kim, M.; Bae, G. Y.; Cho, K. Decoupling Charge Transfer and Transport at Polymeric Hole Transport Layer in Perovskite Solar Cells. *ACS Appl. Mater. Interfaces* **2016**, *8* (10), 6546–6553. https://doi.org/10.1021/acsami.5b12023.

(46) Ono, L. K.; Raga, S. R.; Remeika, M.; Winchester, A. J.; Gabe, A.; Qi, Y. Pinhole-Free Hole Transport Layers Significantly Improve the Stability of MAPbI 3 -Based Perovskite Solar Cells under Operating Conditions. *J. Mater. Chem. A* **2015**, *3* (30), 15451–15456. https://doi.org/10.1039/C5TA03443D.

(47) Liao, H.-C.; Tam, T. L. D.; Guo, P.; Wu, Y.; Manley, E. F.; Huang, W.; Zhou, N.; Soe, C. M. M.; Wang, B.; Wasielewski, M. R.; et al. Dopant-Free Hole Transporting Polymers for High Efficiency, Environmentally Stable Perovskite Solar Cells. *Adv. Energy Mater.* **2016**, *6* (16), 1600502. https://doi.org/10.1002/aenm.201600502.

(48) Huang, J.; Yu, X.; Xie, J.; Li, C.-Z.; Zhang, Y.; Xu, D.; Tang, Z.; Cui, C.; Yang, D. Fulleropyrrolidinium Iodide As an Efficient Electron Transport Layer for Air-Stable Planar Perovskite Solar Cells. *ACS Appl. Mater. Interfaces* **2016**, *8* (50), 34612–34619. https://doi.org/10.1021/acsami.6b08771.

(49) Reddy, S. S.; Gunasekar, K.; Heo, J. H.; Im, S. H.; Kim, C. S.; Kim, D.-H.; Moon, J. H.; Lee, J. Y.; Song, M.; Jin, S.-H. Highly Efficient Organic Hole Transporting Materials for Perovskite and Organic Solar Cells with Long-Term Stability. *Adv. Mater.* **2016**, *28* (4), 686–693. https://doi.org/10.1002/adma.201503729.

(50) Yu, Z.; Sun, L. Recent Progress on Hole-Transporting Materials for Emerging Organometal Halide Perovskite Solar Cells. *Adv. Energy Mater.* **2015**, *5* (12), 1500213. https://doi.org/10.1002/aenm.201500213.

(51) Huang, A. B.; Zhu, J. T.; Zheng, J. Y.; Yu, Y.; Liu, Y.; Yang, S. W.; Bao, S. H.; Lei, L.; Jin, P. Achieving High-Performance Planar Perovskite Solar Cells with Co-Sputtered Co-Doping NiO x Hole Transport Layers by Efficient Extraction and Enhanced Mobility. *J. Mater. Chem. C* **2016**, *4* (46), 10839–10846. https://doi.org/10.1039/C6TC03624D.

(52) Kim, J. H.; Liang, P.-W.; Williams, S. T.; Cho, N.; Chueh, C.-C.; Glaz, M. S.; Ginger, D. S.; Jen, A. K.-Y. High-Performance and Environmentally Stable Planar Heterojunction Perovskite Solar Cells Based on a Solution-Processed Copper-

Doped Nickel Oxide Hole-Transporting Layer. *Adv. Mater.* **2015**, *27* (4), 695–701. https://doi.org/10.1002/adma.201404189.

(53) Yang, J.; Siempelkamp, B. D.; Liu, D.; Kelly, T. L. Investigation of CH 3 NH 3 PbI 3 Degradation Rates and Mechanisms in Controlled Humidity Environments Using in Situ Techniques. *ACS Nano* **2015**, *9* (2), 1955–1963. https://doi.org/10.1021/nn506864k.

(54) Han, Y.; Meyer, S.; Dkhissi, Y.; Weber, K.; Pringle, J. M.; Bach, U.; Spiccia, L.; Cheng, Y.-B. Degradation Observations of Encapsulated Planar CH 3 NH 3 PbI 3 Perovskite Solar Cells at High Temperatures and Humidity. *J. Mater. Chem. A* **2015**, *3* (15), 8139–8147. https://doi.org/10.1039/C5TA00358J.

(55) You, J.; Meng, L.; Song, T.-B.; Guo, T.-F.; Yang, Y. (Michael); Chang, W.-H.; Hong, Z.; Chen, H.; Zhou, H.; Chen, Q.; et al. Improved Air Stability of Perovskite Solar Cells via Solution-Processed Metal Oxide Transport Layers. *Nat. Nanotechnol.* **2016**, *11* (1), 75–81. https://doi.org/10.1038/nnano.2015.230.

(56) Zhang, J.; Xu, B.; Johansson, M. B.; Vlachopoulos, N.; Boschloo, G.; Sun, L.; Johansson, E. M. J.; Hagfeldt, A. Strategy to Boost the Efficiency of Mixed-Ion Perovskite Solar Cells: Changing Geometry of the Hole Transporting Material. *ACS Nano* **2016**, *10* (7), 6816–6825. https://doi.org/10.1021/acsnano.6b02442.

(57) Wang, J.; Liu, K.; Ma, L.; Zhan, X. Triarylamine: Versatile Platform for Organic, Dye-Sensitized, and Perovskite Solar Cells. *Chem. Rev.* **2016**, *116* (23), 14675–14725. https://doi.org/10.1021/acs.chemrev.6b00432.

(58) Sung, S. Do; Kang, M. S.; Choi, I. T.; Kim, H. M.; Kim, H.; Hong, M.; Kim, H. K.; Lee, W. I. 14.8% Perovskite Solar Cells Employing Carbazole Derivatives as Hole Transporting Materials. *Chem. Commun.* **2014**, *50* (91), 14161–14163. https://doi.org/10.1039/C4CC06716A.

(59) Kang, M. S.; Sung, S. Do; Choi, I. T.; Kim, H.; Hong, M.; Kim, J.; Lee, W. I.; Kim, H. K. Novel Carbazole-Based Hole-Transporting Materials with Star-Shaped Chemical Structures for Perovskite-Sensitized Solar Cells. *ACS Appl. Mater. Interfaces* **2015**, *7* (40), 22213–22217. https://doi.org/10.1021/acsami.5b04662.

(60) Wang, H.; Sheikh, A. D.; Feng, Q.; Li, F.; Chen, Y.; Yu, W.; Alarousu, E.; Ma, C.; Haque, M. A.; Shi, D.; et al. Facile Synthesis and High Performance of a New Carbazole-Based Hole-Transporting Material for Hybrid Perovskite Solar Cells. *ACS Photonics* **2015**, *2* (7), 849–855. https://doi.org/10.1021/acsphotonics.5b00283.

(61) Kranthiraja, K.; Gunasekar, K.; Kim, H.; Cho, A.-N.; Park, N.-G.; Kim, S.; Kim, B. J.; Nishikubo, R.; Saeki, A.; Song, M.; et al. High-Performance Long-Term-Stable Dopant-Free Perovskite Solar Cells and Additive-Free Organic Solar Cells by Employing Newly Designed Multirole π-Conjugated Polymers. *Adv. Mater.* **2017**, *29* (23), 1700183. https://doi.org/10.1002/adma.201700183.

(62) Bi, C.; Wang, Q.; Shao, Y.; Yuan, Y.; Xiao, Z.; Huang, J. Non-Wetting Surface-Driven High-Aspect-Ratio Crystalline Grain Growth for Efficient Hybrid Perovskite

Solar Cells. *Nat. Commun.* **2015**, *6* (1), 7747. https://doi.org/10.1038/ncomms8747.

(63) Jeon, N. J.; Noh, J. H.; Kim, Y. C.; Yang, W. S.; Ryu, S.; Seok, S. Il. Solvent Engineering for High-Performance Inorganic-Organic Hybrid Perovskite Solar Cells. *Nat. Mater.* **2014**, *13* (September), 897–903. https://doi.org/10.1038/nmat4014.

(64) Li, X.; Liu, X.; Wang, X.; Zhao, L.; Jiu, T.; Fang, J. Polyelectrolyte Based Hole-Transporting Materials for High Performance Solution Processed Planar Perovskite Solar Cells. *J. Mater. Chem. A* **2015**, *3* (29), 15024–15029. https://doi.org/10.1039/C5TA04712A.

(65) Choi, H.; Mai, C.-K.; Kim, H.-B.; Jeong, J.; Song, S.; Bazan, G. C.; Kim, J. Y.; Heeger, A. J. Conjugated Polyelectrolyte Hole Transport Layer for Inverted-Type Perovskite Solar Cells. *Nat. Commun.* **2015**, *6* (1), 7348. https://doi.org/10.1038/ncomms8348.

(66) Mali, S. S.; Hong, C. K. P-i-n/n-i-p Type Planar Hybrid Structure of Highly Efficient Perovskite Solar Cells towards Improved Air Stability: Synthetic Strategies and the Role of p-Type Hole Transport Layer (HTL) and n-Type Electron Transport Layer (ETL) Metal Oxides. *Nanoscale* **2016**, *8* (20), 10528–10540. https://doi.org/10.1039/C6NR02276F.

(67) Belisle, R. A.; Jain, P.; Prasanna, R.; Leijtens, T.; McGehee, M. D. Minimal Effect of the Hole-Transport Material Ionization Potential on the Open-Circuit Voltage of Perovskite Solar Cells. *ACS Energy Lett.* **2016**, *1* (3), 556–560. https://doi.org/10.1021/acsenergylett.6b00270.

(68) Ishida, N.; Wakamiya, A.; Saeki, A. Quantifying Hole Transfer Yield from Perovskite to Polymer Layer: Statistical Correlation of Solar Cell Outputs with Kinetic and Energetic Properties. *ACS Photonics* **2016**, *3* (9), 1678–1688. https://doi.org/10.1021/acsphotonics.6b00331.

(69) Kim, G.-W.; Kang, G.; Malekshahi Byranvand, M.; Lee, G.-Y.; Park, T. Gradated Mixed Hole Transport Layer in a Perovskite Solar Cell: Improving Moisture Stability and Efficiency. *ACS Appl. Mater. Interfaces* **2017**, *9* (33), 27720–27726. https://doi.org/10.1021/acsami.7b07071.

(70) Rakstys, K.; Abate, A.; Dar, M. I.; Gao, P.; Jankauskas, V.; Jacopin, G.; Kamarauskas, E.; Kazim, S.; Ahmad, S.; Grätzel, M.; et al. Triazatruxene-Based Hole Transporting Materials for Highly Efficient Perovskite Solar Cells. *J. Am. Chem. Soc.* **2015**, *137* (51), 16172–16178. https://doi.org/10.1021/jacs.5b11076.

(71) Planells, M.; Abate, A.; Hollman, D. J.; Stranks, S. D.; Bharti, V.; Gaur, J.; Mohanty, D.; Chand, S.; Snaith, H. J.; Robertson, N. Diacetylene Bridged Triphenylamines as Hole Transport Materials for Solid State Dye Sensitized Solar Cells. *J. Mater. Chem. A* **2013**, *1* (23), 6949. https://doi.org/10.1039/c3ta11417a.

(72) Schulz, P.; Edri, E.; Kirmayer, S.; Hodes, G.; Cahen, D.; Kahn, A. Interface Energetics in Organo-Metal Halide Perovskite-Based Photovoltaic Cells. *Energy Environ. Sci.* **2014**, *7* (4), 1377. https://doi.org/10.1039/c4ee00168k.

(73) Miller, E. M.; Zhao, Y.; Mercado, C. C.; Saha, S. K.; Luther, J. M.; Zhu, K.; Stevanović, V.; Perkins, C. L.; van de Lagemaat, J. Substrate-Controlled Band Positions in CH 3 NH 3 PbI 3 Perovskite Films. *Phys. Chem. Chem. Phys.* **2014**, *16* (40), 22122–22130. https://doi.org/10.1039/C4CP03533J.

(74) Lo, M.-F.; Guan, Z.-Q.; Ng, T.-W.; Chan, C.-Y.; Lee, C.-S. Electronic Structures and Photoconversion Mechanism in Perovskite/Fullerene Heterojunctions. *Adv. Funct. Mater.* **2015**, *25* (8), 1213–1218. https://doi.org/10.1002/adfm.201402692.

(75) Endres, J.; Egger, D. A.; Kulbak, M.; Kerner, R. A.; Zhao, L.; Silver, S. H.; Hodes, G.; Rand, B. P.; Cahen, D.; Kronik, L.; et al. Valence and Conduction Band Densities of States of Metal Halide Perovskites: A Combined Experimental–Theoretical Study. *J. Phys. Chem. Lett.* **2016**, *7* (14), 2722–2729. https://doi.org/10.1021/acs.jpclett.6b00946.

(76) Harwell, J. R.; Baikie, T. K.; Baikie, I. D.; Payne, J. L.; Ni, C.; Irvine, J. T. S.; Turnbull, G. A.; Samuel, I. D. W. Probing the Energy Levels of Perovskite Solar Cells via Kelvin Probe and UV Ambient Pressure Photoemission Spectroscopy. *Phys. Chem. Chem. Phys.* **2016**, *18* (29), 19738–19745. https://doi.org/10.1039/C6CP02446G.

(77) Li, C.; Wei, J.; Sato, M.; Koike, H.; Xie, Z.-Z.; Li, Y.-Q.; Kanai, K.; Kera, S.; Ueno, N.; Tang, J.-X. Halide-Substituted Electronic Properties of Organometal Halide Perovskite Films: Direct and Inverse Photoemission Studies. *ACS Appl. Mater. Interfaces* **2016**, *8* (18), 11526–11531. https://doi.org/10.1021/acsami.6b02692.

(78) Calloni, A.; Abate, A.; Bussetti, G.; Berti, G.; Yivlialin, R.; Ciccacci, F.; Duò, L. Stability of Organic Cations in Solution-Processed CH 3 NH 3 PbI 3 Perovskites: Formation of Modified Surface Layers. *J. Phys. Chem. C* **2015**, *119* (37), 21329–21335. https://doi.org/10.1021/acs.jpcc.5b05422.

(79) Olthof, S. Research Update: The Electronic Structure of Hybrid Perovskite Layers and Their Energetic Alignment in Devices. *APL Mater.* **2016**, *4* (9), 091502. https://doi.org/10.1063/1.4960112.

(80) Jung, M.-C.; Qi, Y. Dopant Interdiffusion Effects in N-i-p Structured Spiro-OMeTAD Hole Transport Layer of Organometal Halide Perovskite Solar Cells. *Org. Electron.* **2016**, *31*, 71–76. https://doi.org/10.1016/j.orgel.2016.01.018.

(81) Graham, K. R.; Ndjawa, G. O. N.; Conron, S. M.; Munir, R.; Vandewal, K.; Chen, J. J.; Sweetnam, S.; Thompson, M. E.; Salleo, A.; McGehee, M. D.; et al. The Roles of Structural Order and Intermolecular Interactions in Determining Ionization Energies and Charge-Transfer State Energies in Organic Semiconductors. *Adv. Energy Mater.* **2016**, *6* (22), 1601211. https://doi.org/10.1002/aenm.201601211.

(82) Endres, J.; Pelczer, I.; Rand, B. P.; Kahn, A. Determination of Energy Level Alignment within an Energy Cascade Organic Solar Cell. *Chem. Mater.* **2016**, *28* (3), 794–801. https://doi.org/10.1021/acs.chemmater.5b03857.

(83) Zhao, L.; Luo, D.; Wu, J.; Hu, Q.; Zhang, W.; Chen, K.; Liu, T.; Liu, Y.; Zhang, Y.; Liu, F.; et al. High-Performance Inverted Planar Heterojunction Perovskite Solar

Cells Based on Lead Acetate Precursor with Efficiency Exceeding 18%. *Adv. Funct. Mater.* **2016**, *26* (20), 3508–3514. https://doi.org/10.1002/adfm.201601175.

(84) Neophytou, M.; Griffiths, J.; Fraser, J.; Kirkus, M.; Chen, H.; Nielsen, C. B.; McCulloch, I. High Mobility, Hole Transport Materials for Highly Efficient PEDOT:PSS Replacement in Inverted Perovskite Solar Cells. *J. Mater. Chem. C* **2017**, *5* (20), 4940–4945. https://doi.org/10.1039/C7TC00858A.

(85) Alnuaimi, A.; Almansouri, I.; Nayfeh, A. Effect of Mobility and Band Structure of Hole Transport Layer in Planar Heterojunction Perovskite Solar Cells Using 2D TCAD Simulation. *J. Comput. Electron.* **2016**, *15* (3), 1110–1118. https://doi.org/10.1007/s10825-016-0850-1.

(86) Ball, J. M.; Petrozza, A. Defects in Perovskite-Halides and Their Effects in Solar Cells. *Nat. Energy* **2016**, *1* (11), 16149. https://doi.org/10.1038/nenergy.2016.149.

(87) Wu, J.; Shi, J.; Li, Y.; Li, H.; Wu, H.; Luo, Y.; Li, D.; Meng, Q. Quantifying the Interface Defect for the Stability Origin of Perovskite Solar Cells. *Adv. Energy Mater.* **2019**, *9* (37), 1901352. https://doi.org/10.1002/aenm.201901352.

(88) Wang, J.; Fu, W.; Jariwala, S.; Sinha, I.; Jen, A. K. Y.; Ginger, D. S. Reducing Surface Recombination Velocities at the Electrical Contacts Will Improve Perovskite Photovoltaics. *ACS Energy Lett.* **2019**, *4* (1), 222–227. https://doi.org/10.1021/acsenergylett.8b02058.

(89) Bi, S.; Leng, X.; Li, Y.; Zheng, Z.; Zhang, X.; Zhang, Y.; Zhou, H. Interfacial Modification in Organic and Perovskite Solar Cells. *Adv. Mater.* **2019**, *31* (45), 1805708. https://doi.org/10.1002/adma.201805708.

(90) Stolterfoht, M.; Caprioglio, P.; Wolff, C. M.; Márquez, J. A.; Nordmann, J.; Zhang, S.; Rothhardt, D.; Hörmann, U.; Amir, Y.; Redinger, A.; et al. The Impact of Energy Alignment and Interfacial Recombination on the Internal and External Open-Circuit Voltage of Perovskite Solar Cells. *Energy Environ. Sci.* **2019**, *12* (9), 2778–2788. https://doi.org/10.1039/C9EE02020A.

(91) Lu, J.; Lin, X.; Jiao, X.; Gengenbach, T.; Scully, A. D.; Jiang, L.; Tan, B.; Sun, J.; Li, B.; Pai, N.; et al. Interfacial Benzenethiol Modification Facilitates Charge Transfer and Improves Stability of Cm-Sized Metal Halide Perovskite Solar Cells with up to 20% Efficiency. *Energy Environ. Sci.* **2018**, *11* (7), 1880–1889. https://doi.org/10.1039/C8EE00754C.

(92) Zhang, H.; Wu, Y.; Shen, C.; Li, E.; Yan, C.; Zhang, W.; Tian, H.; Han, L.; Zhu, W. Efficient and Stable Chemical Passivation on Perovskite Surface via Bidentate Anchoring. *Adv. Energy Mater.* **2019**, *9* (13), 1803573. https://doi.org/10.1002/aenm.201803573.

(93) Liu, C.; Huang, Z.; Hu, X.; Meng, X.; Huang, L.; Xiong, J.; Tan, L.; Chen, Y. Grain Boundary Modification via F4TCNQ To Reduce Defects of Perovskite Solar Cells with Excellent Device Performance. *ACS Appl. Mater. Interfaces* **2018**, *10* (2), 1909–1916. https://doi.org/10.1021/acsami.7b15031.

(94) Jiang, H.; Yan, Z.; Zhao, H.; Yuan, S.; Yang, Z.; Li, J.; Liu, B.; Niu, T.; Feng, J.; Wang, Q.; et al. Bifunctional Hydroxylamine Hydrochloride Incorporated Perovskite Films for Efficient and Stable Planar Perovskite Solar Cells. *ACS Appl. Energy Mater.* **2018**, *1* (2), 900–909. https://doi.org/10.1021/acsaem.8b00060.

(95) Wang, S.; Zhu, Y.; Wang, C.; Ma, R. Interface Modification by a Multifunctional Ammonium Salt for High Performance and Stable Planar Perovskite Solar Cells. *J. Mater. Chem. A* **2019**, *7* (19), 11867–11876. https://doi.org/10.1039/C9TA02631B.

(96) Zheng, X.; Deng, Y.; Chen, B.; Wei, H.; Xiao, X.; Fang, Y.; Lin, Y.; Yu, Z.; Liu, Y.; Wang, Q.; et al. Dual Functions of Crystallization Control and Defect Passivation Enabled by Sulfonic Zwitterions for Stable and Efficient Perovskite Solar Cells. *Adv. Mater.* **2018**, *30* (52), 1803428. https://doi.org/10.1002/adma.201803428.

(97) Li, X.; Ibrahim Dar, M.; Yi, C.; Luo, J.; Tschumi, M.; Zakeeruddin, S. M.; Nazeeruddin, M. K.; Han, H.; Grätzel, M. Improved Performance and Stability of Perovskite Solar Cells by Crystal Crosslinking with Alkylphosphonic Acid ω-Ammonium Chlorides. *Nat. Chem.* **2015**, *7* (9), 703–711. https://doi.org/10.1038/nchem.2324.

(98) Lin, C.; De Rossi, F.; Kim, J.; Baker, J.; Ngiam, J.; Xu, B.; Pont, S.; Aristidou, N.; Haque, S. A.; Watson, T.; et al. Evidence for Surface Defect Passivation as the Origin of the Remarkable Photostability of Unencapsulated Perovskite Solar Cells Employing Aminovaleric Acid as a Processing Additive. *J. Mater. Chem. A* **2019**, *7* (7), 3006–3011. https://doi.org/10.1039/C8TA11985F.

(99) Wang, S.; Chen, H.; Zhang, J.; Xu, G.; Chen, W.; Xue, R.; Zhang, M.; Li, Y.; Li, Y. Targeted Therapy for Interfacial Engineering Toward Stable and Efficient Perovskite Solar Cells. *Adv. Mater.* **2019**, *31* (41), 1903691. https://doi.org/10.1002/adma.201903691.

(100) Zhao, L.; Rolston, N.; Lee, K. M.; Zhao, X.; Reyes-Martinez, M. A.; Tran, N. L.; Yeh, Y.-W.; Yao, N.; Scholes, G. D.; Loo, Y.; et al. Influence of Bulky Organo-Ammonium Halide Additive Choice on the Flexibility and Efficiency of Perovskite Light-Emitting Devices. *Adv. Funct. Mater.* **2018**, *28* (31), 1802060. https://doi.org/10.1002/adfm.201802060.

(101) Yang, J.; Liu, C.; Cai, C.; Hu, X.; Huang, Z.; Duan, X.; Meng, X.; Yuan, Z.; Tan, L.; Chen, Y. High-Performance Perovskite Solar Cells with Excellent Humidity and Thermo-Stability via Fluorinated Perylenediimide. *Adv. Energy Mater.* **2019**, *9* (18), 1900198. https://doi.org/10.1002/aenm.201900198.

(102) Cao, J.; Yin, J.; Yuan, S.; Zhao, Y.; Li, J.; Zheng, N. Thiols as Interfacial Modifiers to Enhance the Performance and Stability of Perovskite Solar Cells. *Nanoscale* **2015**, *7* (21), 9443–9447. https://doi.org/10.1039/C5NR01820J.

(103) Xie, L.; Chen, J.; Vashishtha, P.; Zhao, X.; Shin, G. S.; Mhaisalkar, S. G.; Park, N.-G. Importance of Functional Groups in Cross-Linking Methoxysilane Additives for High-Efficiency and Stable Perovskite Solar Cells. *ACS Energy Lett.* **2019**, *4* (9),

2192–2200. https://doi.org/10.1021/acsenergylett.9b01356.

(104) Noel, N. K.; Abate, A.; Stranks, S. D.; Parrott, E. S.; Burlakov, V. M.; Goriely, A.; Snaith, H. J. Enhanced Photoluminescence and Solar Cell Performance via Lewis Base Passivation of Organic–Inorganic Lead Halide Perovskites. *ACS Nano* **2014**, *8* (10), 9815–9821. https://doi.org/10.1021/nn5036476.

(105) de Quilettes, D. W.; Vorpahl, S. M.; Stranks, S. D.; Nagaoka, H.; Eperon, G. E.; Ziffer, M. E.; Snaith, H. J.; Ginger, D. S. Impact of Microstructure on Local Carrier Lifetime in Perovskite Solar Cells. *Science (80-. ).* **2015**, *348* (6235), 683–686. https://doi.org/10.1126/science.aaa5333.

(106) Jeon, N. J.; Noh, J. H.; Kim, Y. C.; Yang, W. S.; Ryu, S.; Seok, S. Il. Solvent Engineering for High-Performance Inorganic–Organic Hybrid Perovskite Solar Cells. *Nat. Mater.* **2014**, *13* (9), 897–903. https://doi.org/10.1038/nmat4014.

(107) Fu, S.; Li, X.; Wan, L.; Wu, Y.; Zhang, W.; Wang, Y.; Bao, Q.; Fang, J. Efficient Passivation with Lead Pyridine-2-Carboxylic for High-Performance and Stable Perovskite Solar Cells. *Adv. Energy Mater.* **2019**, *9* (35), 1901852. https://doi.org/10.1002/aenm.201901852.

(108) Zhao, L.; Kerner, R. A.; Xiao, Z.; Lin, Y. L.; Lee, K. M.; Schwartz, J.; Rand, B. P. Redox Chemistry Dominates the Degradation and Decomposition of Metal Halide Perovskite Optoelectronic Devices. *ACS Energy Lett.* **2016**, *1* (3), 595–602. https://doi.org/10.1021/acsenergylett.6b00320.

(109) Quintero-Bermudez, R.; Proppe, A. H.; Mahata, A.; Todorović, P.; Kelley, S. O.; De Angelis, F.; Sargent, E. H. Ligand-Induced Surface Charge Density Modulation Generates Local Type-II Band Alignment in Reduced-Dimensional Perovskites. *J. Am. Chem. Soc.* **2019**, *141* (34), 13459–13467. https://doi.org/10.1021/jacs.9b04801.

(110) Kayesh, M. E.; Matsuishi, K.; Kaneko, R.; Kazaoui, S.; Lee, J.-J.; Noda, T.; Islam, A. Coadditive Engineering with 5-Ammonium Valeric Acid Iodide for Efficient and Stable Sn Perovskite Solar Cells. *ACS Energy Lett.* **2019**, *4* (1), 278–284. https://doi.org/10.1021/acsenergylett.8b02216.

(111) Zhou, W.; Li, D.; Xiao, Z.; Wen, Z.; Zhang, M.; Hu, W.; Wu, X.; Wang, M.; Zhang, W.; Lu, Y.; et al. Zwitterion Coordination Induced Highly Orientational Order of CH 3 NH 3 PbI 3 Perovskite Film Delivers a High Open Circuit Voltage Exceeding 1.2 V. *Adv. Funct. Mater.* **2019**, *29* (23), 1901026. https://doi.org/10.1002/adfm.201901026.

(112) deQuilettes, D. W.; Koch, S.; Burke, S.; Paranji, R. K.; Shropshire, A. J.; Ziffer, M. E.; Ginger, D. S. Photoluminescence Lifetimes Exceeding 8 Ms and Quantum Yields Exceeding 30% in Hybrid Perovskite Thin Films by Ligand Passivation. *ACS Energy Lett.* **2016**, *1* (2), 438–444. https://doi.org/10.1021/acsenergylett.6b00236.

(113) Koscher, B. A.; Swabeck, J. K.; Bronstein, N. D.; Alivisatos, A. P. Essentially Trap-Free CsPbBr 3 Colloidal Nanocrystals by Postsynthetic Thiocyanate Surface Treatment. *J. Am. Chem. Soc.* **2017**, *139* (19), 6566–6569.

https://doi.org/10.1021/jacs.7b02817.

(114) Uddin, M. A.; Calabro, R. L.; Kim, D.-Y.; Graham, K. R. Halide Exchange and Surface Modification of Metal Halide Perovskite Nanocrystals with Alkyltrichlorosilanes. *Nanoscale* **2018**, *10* (35), 16919–16927. https://doi.org/10.1039/C8NR04763D.

(115) Yoon, Y. J.; Lee, K. T.; Lee, T. K.; Kim, S. H.; Shin, Y. S.; Walker, B.; Park, S. Y.; Heo, J.; Lee, J.; Kwak, S. K.; et al. Reversible, Full-Color Luminescence by Post-Treatment of Perovskite Nanocrystals. *Joule* **2018**, *2* (10), 2105–2116. https://doi.org/10.1016/j.joule.2018.07.012.

(116) Uddin, M. A.; Mobley, J. K.; Masud, A. A.; Liu, T.; Calabro, R. L.; Kim, D.; Richards, C. I.; Graham, K. R. Mechanistic Exploration of Dodecanethiol-Treated Colloidal CsPbBr 3 Nanocrystals with Photoluminescence Quantum Yields Reaching Near 100%. *J. Phys. Chem. C* **2019**, *123* (29), 18103–18112. https://doi.org/10.1021/acs.jpcc.9b05612.

(117) Ahmed, T.; Seth, S.; Samanta, A. Boosting the Photoluminescence of CsPbX 3 (X = Cl, Br, I) Perovskite Nanocrystals Covering a Wide Wavelength Range by Postsynthetic Treatment with Tetrafluoroborate Salts. *Chem. Mater.* **2018**, *30* (11), 3633–3637. https://doi.org/10.1021/acs.chemmater.8b01235.

(118) Brown, A. A. M.; Hooper, T. J. N.; Veldhuis, S. A.; Chin, X. Y.; Bruno, A.; Vashishtha, P.; Tey, J. N.; Jiang, L.; Damodaran, B.; Pu, S. H.; et al. Self-Assembly of a Robust Hydrogen-Bonded Octylphosphonate Network on Cesium Lead Bromide Perovskite Nanocrystals for Light-Emitting Diodes. *Nanoscale* **2019**, *11* (25), 12370–12380. https://doi.org/10.1039/C9NR02566A.

(119) Nenon, D. P.; Pressler, K.; Kang, J.; Koscher, B. A.; Olshansky, J. H.; Osowiecki, W. T.; Koc, M. A.; Wang, L.-W.; Alivisatos, A. P. Design Principles for Trap-Free CsPbX 3 Nanocrystals: Enumerating and Eliminating Surface Halide Vacancies with Softer Lewis Bases. *J. Am. Chem. Soc.* **2018**, *140* (50), 17760–17772. https://doi.org/10.1021/jacs.8b11035.

(120) Abdelmageed, G.; Sully, H. R.; Bonabi Naghadeh, S.; El-Hag Ali, A.; Carter, S. A.; Zhang, J. Z. Improved Stability of Organometal Halide Perovskite Films and Solar Cells toward Humidity via Surface Passivation with Oleic Acid. *ACS Appl. Energy Mater.* **2018**, *1* (2), 387–392. https://doi.org/10.1021/acsaem.7b00069.

(121) Li, X.; Chen, C.-C.; Cai, M.; Hua, X.; Xie, F.; Liu, X.; Hua, J.; Long, Y.-T.; Tian, H.; Han, L. Efficient Passivation of Hybrid Perovskite Solar Cells Using Organic Dyes with □COOH Functional Group. *Adv. Energy Mater.* **2018**, *8* (20), 1800715. https://doi.org/10.1002/aenm.201800715.

(122) Yang, S.; Wang, Y.; Liu, P.; Cheng, Y.; Zhao, H. J.; Yang, H. G. Functionalization of Perovskite Thin Films with Moisture-Tolerant Molecules. *Nat. Energy* **2016**, *1* (2), 15016. https://doi.org/10.1038/nenergy.2015.16.

(123) Abtahi, A.; Mazza, S. M.; Ryno, S. M.; Loya, E. K.; Li, R.; Parkin, S. R.; Risko, C.; Anthony, J. E.; Graham, K. R. Effect of Halogenation on the Energetics of Pure and

Mixed Phases in Model Organic Semiconductors Composed of Anthradithiophene Derivatives and C 60. *J. Phys. Chem. C* **2018**, *122* (9), 4757–4767. https://doi.org/10.1021/acs.jpcc.7b11729.

(124) Zhang, F.; Huang, Q.; Song, J.; Zhang, Y.; Ding, C.; Liu, F.; Liu, D.; Li, X.; Yasuda, H.; Yoshida, K.; et al. Growth of Amorphous Passivation Layer Using Phenethylammonium Iodide for High-Performance Inverted Perovskite Solar Cells. *Sol. RRL* **2020**, *4* (2), 1900243. https://doi.org/10.1002/solr.201900243.

(125) Yang, S.; Dai, J.; Yu, Z.; Shao, Y.; Zhou, Y.; Xiao, X.; Zeng, X. C.; Huang, J. Tailoring Passivation Molecular Structures for Extremely Small Open-Circuit Voltage Loss in Perovskite Solar Cells. *J. Am. Chem. Soc.* **2019**, *141* (14), 5781–5787. https://doi.org/10.1021/jacs.8b13091.

(126) Adriaenssens, L.; Gil-Ramírez, G.; Frontera, A.; Quiñonero, D.; Escudero-Adán, E. C.; Ballester, P. Thermodynamic Characterization of Halide−π Interactions in Solution Using "Two-Wall" Aryl Extended Calix[4]Pyrroles as Model System. *J. Am. Chem. Soc.* **2014**, *136* (8), 3208–3218. https://doi.org/10.1021/ja412098v.

(127) Giese, M.; Albrecht, M.; Rissanen, K. Experimental Investigation of Anion–π Interactions – Applications and Biochemical Relevance. *Chem. Commun.* **2016**, *52* (9), 1778–1795. https://doi.org/10.1039/C5CC09072E.

(128) Gliboff, M.; Li, H.; Knesting, K. M.; Giordano, A. J.; Nordlund, D.; Seidler, G. T.; Brédas, J.-L.; Marder, S. R.; Ginger, D. S. Competing Effects of Fluorination on the Orientation of Aromatic and Aliphatic Phosphonic Acid Monolayers on Indium Tin Oxide. *J. Phys. Chem. C* **2013**, *117* (29), 15139–15147. https://doi.org/10.1021/jp404033e.

(129) Brundle, C. R.; Hopster, H.; Swalen, J. D. Electron Mean-free Pathlengths through Monolayers of Cadmium Arachidate. *J. Chem. Phys.* **1979**, *70* (11), 5190–5196. https://doi.org/10.1063/1.437361.

(130) Bain, C. D.; Whitesides, G. M. Attenuation Lengths of Photoelectrons in Hydrocarbon Films. *J. Phys. Chem.* **1989**, *93* (4), 1670–1673. https://doi.org/10.1021/j100341a095.

(131) Seah, M. P.; Spencer, S. J. Attenuation Lengths in Organic Materials. *Surf. Interface Anal.* **2011**, *43* (3), 744–751. https://doi.org/10.1002/sia.3607.

(132) Gao, W.; Zielinski, K.; Drury, B. N.; Carl, A. D.; Grimm, R. L. Elucidation of Chemical Species and Reactivity at Methylammonium Lead Iodide and Cesium Tin Bromide Perovskite Surfaces via Orthogonal Reaction Chemistry. *J. Phys. Chem. C* **2018**, *122* (31), 17882–17894. https://doi.org/10.1021/acs.jpcc.8b05352.

(133) Carl, A. D.; Kalan, R. E.; Obayemi, J. D.; Zebaze Kana, M. G.; Soboyejo, W. O.; Grimm, R. L. Synthesis and Characterization of Alkylamine-Functionalized Si(111) for Perovskite Adhesion With Minimal Interfacial Oxidation or Electronic Defects. *ACS Appl. Mater. Interfaces* **2017**, *9* (39), 34377–34388. https://doi.org/10.1021/acsami.7b07117.

(134) Ebel, M. F. Zur Bestimmung Der Reduzierten Dicke D/λ Dünner Schichten Mittels XPS. *J. Electron Spectros. Relat. Phenomena* **1978**, *14* (4), 287–322. https://doi.org/10.1016/0368-2048(78)80005-X.

(135) D. Briggs, M. P. S. *Practical Surface Analysis by Auger and X-Ray Photoelectron Spectroscopy*; 1983.

(136) John F. Moulder, William F. Stickle, Peter E. Sobol, K. D. B. *Handbook of X-Ray Photoelectron Spectroscopy*; 1992.

(137) de Boer, B.; Hadipour, A.; Mandoc, M. M.; van Woudenbergh, T.; Blom, P. W. M. Tuning of Metal Work Functions with Self-Assembled Monolayers. *Adv. Mater.* **2005**, *17* (5), 621–625. https://doi.org/10.1002/adma.200401216.

(138) Crispin, X. Interface Dipole at Organic/Metal Interfaces and Organic Solar Cells. *Sol. Energy Mater. Sol. Cells* **2004**, *83* (2–3), 147–168. https://doi.org/10.1016/j.solmat.2004.02.022.

(139) Ishii, H.; Sugiyama, K.; Ito, E.; Seki, K. Energy Level Alignment and Interfacial Electronic Structures at Organic/Metal and Organic/Organic Interfaces. *Adv. Mater.* **1999**, *11* (8), 605–625. https://doi.org/10.1002/(SICI)1521-4095(199906)11:8<605::AID-ADMA605>3.0.CO;2-Q.

(140) Heimel, G.; Salzmann, I.; Duhm, S.; Koch, N. Design of Organic Semiconductors from Molecular Electrostatics †. *Chem. Mater.* **2011**, *23* (3), 359–377. https://doi.org/10.1021/cm1021257.

(141) Meggiolaro, D.; Mosconi, E.; Proppe, A. H.; Quintero-Bermudez, R.; Kelley, S. O.; Sargent, E. H.; De Angelis, F. Energy Level Tuning at the MAPbI 3 Perovskite/Contact Interface Using Chemical Treatment. *ACS Energy Lett.* **2019**, *4* (9), 2181–2184. https://doi.org/10.1021/acsenergylett.9b01584.

(142) Emara, J.; Schnier, T.; Pourdavoud, N.; Riedl, T.; Meerholz, K.; Olthof, S. Impact of Film Stoichiometry on the Ionization Energy and Electronic Structure of CH 3 NH 3 PbI 3 Perovskites. *Adv. Mater.* **2016**, *28* (3), 553–559. https://doi.org/10.1002/adma.201503406.

(143) Boehm, A. M.; Wieser, J.; Butrouna, K.; Graham, K. R. A New Photon Source for Ultraviolet Photoelectron Spectroscopy of Organic and Other Damage-Prone Materials. *Org. Electron.* **2017**, *41*, 9–16. https://doi.org/10.1016/j.orgel.2016.11.032.

(144) Yoshida, H. Near-Ultraviolet Inverse Photoemission Spectroscopy Using Ultra-Low Energy Electrons. *Chem. Phys. Lett.* **2012**, *539–540*, 180–185. https://doi.org/10.1016/j.cplett.2012.04.058.

(145) Yang, S.; Wang, Y.; Liu, P.; Cheng, Y.-B.; Zhao, H. J.; Yang, H. G. Functionalization of Perovskite Thin Films with Moisture-Tolerant Molecules. *Nat. Energy* **2016**, *1* (2), 15016. https://doi.org/10.1038/nenergy.2015.16.

(146) Wang, F.; Geng, W.; Zhou, Y.; Fang, H.-H.; Tong, C.-J.; Loi, M. A.; Liu, L.-M.; Zhao, N. Phenylalkylamine Passivation of Organolead Halide Perovskites Enabling

High-Efficiency and Air-Stable Photovoltaic Cells. *Adv. Mater.* **2016**, *28* (45), 9986–9992. https://doi.org/10.1002/adma.201603062.

(147) Yoo, H.; Park, N. Post-Treatment of Perovskite Film with Phenylalkylammonium Iodide for Hysteresis-Less Perovskite Solar Cells. *Sol. Energy Mater. Sol. Cells* **2018**, *179*, 57–65. https://doi.org/10.1016/j.solmat.2018.02.015.

(148) Perovskites Take Steps to Industrialization. *Nat. Energy* **2020**, *5* (1), 1–1. https://doi.org/10.1038/s41560-020-0552-6.

(149) Belisle, R. A.; Bush, K. A.; Bertoluzzi, L.; Gold-Parker, A.; Toney, M. F.; McGehee, M. D. Impact of Surfaces on Photoinduced Halide Segregation in Mixed-Halide Perovskites. *ACS Energy Lett.* **2018**, *3* (11), 2694–2700. https://doi.org/10.1021/acsenergylett.8b01562.

(150) Abdelmageed, G.; Jewell, L.; Hellier, K.; Seymour, L.; Luo, B.; Bridges, F.; Zhang, J. Z.; Carter, S. Mechanisms for Light Induced Degradation in MAPbI 3 Perovskite Thin Films and Solar Cells. *Appl. Phys. Lett.* **2016**, *109* (23), 233905. https://doi.org/10.1063/1.4967840.

(151) Gao, P.; Bin Mohd Yusoff, A. R.; Nazeeruddin, M. K. Dimensionality Engineering of Hybrid Halide Perovskite Light Absorbers. *Nat. Commun.* **2018**, *9* (1), 5028. https://doi.org/10.1038/s41467-018-07382-9.

(152) Lee, J.-W.; Kim, S.-G.; Yang, J.-M.; Yang, Y.; Park, N.-G. Verification and Mitigation of Ion Migration in Perovskite Solar Cells. *APL Mater.* **2019**, *7* (4), 041111. https://doi.org/10.1063/1.5085643.

(153) Song, Q.; Liang, C.; Zhang, H.; Ji, C.; Sun, M.; Sun, F.; Jing, X.; You, F.; Lu, Y.; He, Z. Additional Organic-Solvent-Rinsing Process to Enhance Perovskite Photovoltaic Performance. *Adv. Electron. Mater.* **2019**, *5* (10), 1900244. https://doi.org/10.1002/aelm.201900244.

(154) Yavari, M.; Mazloum-Ardakani, M.; Gholipour, S.; Tavakoli, M. M.; Turren-Cruz, S.-H.; Taghavinia, N.; Grätzel, M.; Hagfeldt, A.; Saliba, M. Greener, Nonhalogenated Solvent Systems for Highly Efficient Perovskite Solar Cells. *Adv. Energy Mater.* **2018**, *8* (21), 1800177. https://doi.org/10.1002/aenm.201800177.

(155) Yun, Y.; Wang, F.; Huang, H.; Fang, Y.; Liu, S.; Huang, W.; Cheng, Z.; Liu, Y.; Cao, Y.; Gao, M.; et al. A Nontoxic Bifunctional (Anti)Solvent as Digestive-Ripening Agent for High-Performance Perovskite Solar Cells. *Adv. Mater.* **2020**, *32* (14), 1907123. https://doi.org/10.1002/adma.201907123.

(156) Han, T.-H.; Lee, J.-W.; Choi, C.; Tan, S.; Lee, C.; Zhao, Y.; Dai, Z.; De Marco, N.; Lee, S.-J.; Bae, S.-H.; et al. Perovskite-Polymer Composite Cross-Linker Approach for Highly-Stable and Efficient Perovskite Solar Cells. *Nat. Commun.* **2019**, *10* (1), 520. https://doi.org/10.1038/s41467-019-08455-z.

(157) Zheng, X.; Hou, Y.; Bao, C.; Yin, J.; Yuan, F.; Huang, Z.; Song, K.; Liu, J.; Troughton, J.; Gasparini, N.; et al. Managing Grains and Interfaces via Ligand Anchoring Enables 22.3%-Efficiency Inverted Perovskite Solar Cells. *Nat. Energy*

**2020**, *5* (2), 131–140. https://doi.org/10.1038/s41560-019-0538-4.

(158) Yoo, J. J.; Wieghold, S.; Sponseller, M. C.; Chua, M. R.; Bertram, S. N.; Hartono, N. T. P.; Tresback, J. S.; Hansen, E. C.; Correa-Baena, J.-P.; Bulović, V.; et al. An Interface Stabilized Perovskite Solar Cell with High Stabilized Efficiency and Low Voltage Loss. *Energy Environ. Sci.* **2019**, *12* (7), 2192–2199. https://doi.org/10.1039/C9EE00751B.

(159) Zheng, Y.; Yang, X.; Su, R.; Wu, P.; Gong, Q.; Zhu, R. High-Performance CsPbI x Br 3- x All-Inorganic Perovskite Solar Cells with Efficiency over 18% via Spontaneous Interfacial Manipulation. *Adv. Funct. Mater.* **2020**, *2000457*, 2000457. https://doi.org/10.1002/adfm.202000457.

(160) Tao, S.; Schmidt, I.; Brocks, G.; Jiang, J.; Tranca, I.; Meerholz, K.; Olthof, S. Absolute Energy Level Positions in Tin- and Lead-Based Halide Perovskites. *Nat. Commun.* **2019**, *10* (1), 2560. https://doi.org/10.1038/s41467-019-10468-7.

(161) Wolff, C. M.; Canil, L.; Rehermann, C.; Ngoc Linh, N.; Zu, F.; Ralaiarisoa, M.; Caprioglio, P.; Fiedler, L.; Stolterfoht, M.; Kogikoski, S.; et al. Perfluorinated Self-Assembled Monolayers Enhance the Stability and Efficiency of Inverted Perovskite Solar Cells. *ACS Nano* **2020**, *14* (2), 1445–1456. https://doi.org/10.1021/acsnano.9b03268.

(162) Zhang, M.; Hu, W.; Shang, Y.; Zhou, W.; Zhang, W.; Yang, S. Surface Passivation of Perovskite Film by Sodium Toluenesulfonate for Highly Efficient Solar Cells. *Sol. RRL* **2020**, *4* (6), 2000113. https://doi.org/10.1002/solr.202000113.

(163) Wei, M.; Xiao, K.; Walters, G.; Lin, R.; Zhao, Y.; Saidaminov, M. I.; Todorović, P.; Johnston, A.; Huang, Z.; Chen, H.; et al. Combining Efficiency and Stability in Mixed Tin–Lead Perovskite Solar Cells by Capping Grains with an Ultrathin 2D Layer. *Adv. Mater.* **2020**, *32* (12), 1907058. https://doi.org/10.1002/adma.201907058.

(164) Guo, P.; Ye, Q.; Yang, X.; Zhang, J.; Xu, F.; Shchukin, D.; Wei, B.; Wang, H. Surface & Grain Boundary Co-Passivation by Fluorocarbon Based Bifunctional Molecules for Perovskite Solar Cells with Efficiency over 21%. *J. Mater. Chem. A* **2019**, *7* (6), 2497–2506. https://doi.org/10.1039/C8TA11524A.

(165) Bai, S.; Da, P.; Li, C.; Wang, Z.; Yuan, Z.; Fu, F.; Kawecki, M.; Liu, X.; Sakai, N.; Wang, J. T.-W.; et al. Planar Perovskite Solar Cells with Long-Term Stability Using Ionic Liquid Additives. *Nature* **2019**, *571* (7764), 245–250. https://doi.org/10.1038/s41586-019-1357-2.

(166) Zhang, Y.; Fei, Z.; Gao, P.; Lee, Y.; Tirani, F. F.; Scopelliti, R.; Feng, Y.; Dyson, P. J.; Nazeeruddin, M. K. A Strategy to Produce High Efficiency, High Stability Perovskite Solar Cells Using Functionalized Ionic Liquid-Dopants. *Adv. Mater.* **2017**, *29* (36), 1702157. https://doi.org/10.1002/adma.201702157.

(167) Kim, M.; Motti, S. G.; Sorrentino, R.; Petrozza, A. Enhanced Solar Cell Stability by Hygroscopic Polymer Passivation of Metal Halide Perovskite Thin Film. *Energy Environ. Sci.* **2018**, *11* (9), 2609–2619. https://doi.org/10.1039/C8EE01101J.

(168) Park, S. M.; Abtahi, A.; Boehm, A. M.; Graham, K. R. Surface Ligands for Methylammonium Lead Iodide Films: Surface Coverage, Energetics, and Photovoltaic Performance. *ACS Energy Lett.* **2020**, *5* (3), 799–806. https://doi.org/10.1021/acsenergylett.0c00054.

(169) Zhao, Q.; Hazarika, A.; Chen, X.; Harvey, S. P.; Larson, B. W.; Teeter, G. R.; Liu, J.; Song, T.; Xiao, C.; Shaw, L.; et al. High Efficiency Perovskite Quantum Dot Solar Cells with Charge Separating Heterostructure. *Nat. Commun.* **2019**, *10* (1), 2842. https://doi.org/10.1038/s41467-019-10856-z.

(170) Zheng, X.; Troughton, J.; Gasparini, N.; Lin, Y.; Wei, M.; Hou, Y.; Liu, J.; Song, K.; Chen, Z.; Yang, C.; et al. Quantum Dots Supply Bulk- and Surface-Passivation Agents for Efficient and Stable Perovskite Solar Cells. *Joule* **2019**, *3* (8), 1963–1976. https://doi.org/10.1016/j.joule.2019.05.005.

(171) Kayesh, M. E.; Matsuishi, K.; Kaneko, R.; Kazaoui, S.; Lee, J.-J.; Noda, T.; Islam, A. Coadditive Engineering with 5-Ammonium Valeric Acid Iodide for Efficient and Stable Sn Perovskite Solar Cells. *ACS Energy Lett.* **2019**, *4* (1), 278–284. https://doi.org/10.1021/acsenergylett.8b02216.

(172) Hou, M.; Xu, Y.; Zhou, B.; Tian, Y.; Wu, Y.; Zhang, D.; Wang, G.; Li, B.; Ren, H.; Li, Y.; et al. Aryl Diammonium Iodide Passivation for Efficient and Stable Hybrid Organ-Inorganic Perovskite Solar Cells. *Adv. Funct. Mater.* **2020**, *30* (34), 2002366. https://doi.org/10.1002/adfm.202002366.

(173) Koh, T. M.; Shanmugam, V.; Guo, X.; Lim, S. S.; Filonik, O.; Herzig, E. M.; Müller-Buschbaum, P.; Swamy, V.; Chien, S. T.; Mhaisalkar, S. G.; et al. Enhancing Moisture Tolerance in Efficient Hybrid 3D/2D Perovskite Photovoltaics. *J. Mater. Chem. A* **2018**, *6* (5), 2122–2128. https://doi.org/10.1039/C7TA09657G.

(174) Zhao, S.; Qin, M.; Wang, H.; Xie, J.; Xie, F.; Chen, J.; Lu, X.; Yan, K.; Xu, J. Cascade Type-II 2D/3D Perovskite Heterojunctions for Enhanced Stability and Photovoltaic Efficiency. *Sol. RRL* **2020**, 2000282. https://doi.org/10.1002/solr.202000282.

(175) Zhu, H.; Liu, Y.; Eickemeyer, F. T.; Pan, L.; Ren, D.; Ruiz-Preciado, M. A.; Carlsen, B.; Yang, B.; Dong, X.; Wang, Z.; et al. Tailored Amphiphilic Molecular Mitigators for Stable Perovskite Solar Cells with 23.5% Efficiency. *Adv. Mater.* **2020**, *32* (12), 1907757. https://doi.org/10.1002/adma.201907757.

(176) SMITH, G. W.; WILLIAMS, H. D. Some Reactions of Adamantane and Adamantane Derivatives. *J. Org. Chem.* **1961**, *26* (7), 2207–2212. https://doi.org/10.1021/jo01351a011.

(177) Kovalenko, A.; Yumusak, C.; Heinrichova, P.; Stritesky, S.; Fekete, L.; Vala, M.; Weiter, M.; Sariciftci, N. S.; Krajcovic, J. Adamantane Substitutions: A Path to High-Performing, Soluble, Versatile and Sustainable Organic Semiconducting Materials. *J. Mater. Chem. C* **2017**, *5* (19), 4716–4723. https://doi.org/10.1039/C6TC05076J.

(178) Li, W.; Cai, X.; Li, B.; Gan, L.; He, Y.; Liu, K.; Chen, D.; Wu, Y.; Su, S.

Adamantane-Substituted Acridine Donor for Blue Dual Fluorescence and Efficient Organic Light-Emitting Diodes. *Angew. Chemie Int. Ed.* **2019**, *58* (2), 582–586. https://doi.org/10.1002/anie.201811703.

(179) Tavakoli, M. M.; Bi, D.; Pan, L.; Hagfeldt, A.; Zakeeruddin, S. M.; Grätzel, M. Adamantanes Enhance the Photovoltaic Performance and Operational Stability of Perovskite Solar Cells by Effective Mitigation of Interfacial Defect States. *Adv. Energy Mater.* **2018**, *8* (19), 1800275. https://doi.org/10.1002/aenm.201800275.

(180) Chhillar, P.; Dhamaniya, B. P.; Dutta, V.; Pathak, S. K. Recycling of Perovskite Films: Route toward Cost-Efficient and Environment-Friendly Perovskite Technology. *ACS Omega* **2019**, *4* (7), 11880–11887. https://doi.org/10.1021/acsomega.9b01053.

(181) Juarez-Perez, E. J.; Ono, L. K.; Maeda, M.; Jiang, Y.; Hawash, Z.; Qi, Y. Photodecomposition and Thermal Decomposition in Methylammonium Halide Lead Perovskites and Inferred Design Principles to Increase Photovoltaic Device Stability. *J. Mater. Chem. A* **2018**, *6* (20), 9604–9612. https://doi.org/10.1039/C8TA03501F.

(182) Mao, P.; Zhou, Q.; Jin, Z.; Li, H.; Wang, J. Efficiency-Enhanced Planar Perovskite Solar Cells via an Isopropanol/Ethanol Mixed Solvent Process. *ACS Appl. Mater. Interfaces* **2016**, *8* (36), 23837–23843. https://doi.org/10.1021/acsami.6b08863.

(183) Stoumpos, C. C.; Cao, D. H.; Clark, D. J.; Young, J.; Rondinelli, J. M.; Jang, J. I.; Hupp, J. T.; Kanatzidis, M. G. Ruddlesden–Popper Hybrid Lead Iodide Perovskite 2D Homologous Semiconductors. *Chem. Mater.* **2016**, *28* (8), 2852–2867. https://doi.org/10.1021/acs.chemmater.6b00847.

(184) Jung, M.; Shin, T. J.; Seo, J.; Kim, G.; Seok, S. Il. Structural Features and Their Functions in Surfactant-Armoured Methylammonium Lead Iodide Perovskites for Highly Efficient and Stable Solar Cells. *Energy Environ. Sci.* **2018**, *11* (8), 2188–2197. https://doi.org/10.1039/C8EE00995C.

(185) Venkatesan, N. R.; Labram, J. G.; Chabinyc, M. L. Charge-Carrier Dynamics and Crystalline Texture of Layered Ruddlesden–Popper Hybrid Lead Iodide Perovskite Thin Films. *ACS Energy Lett.* **2018**, *3* (2), 380–386. https://doi.org/10.1021/acsenergylett.7b01245.

(186) Wang, H.; Zhu, C.; Liu, L.; Ma, S.; Liu, P.; Wu, J.; Shi, C.; Du, Q.; Hao, Y.; Xiang, S.; et al. Interfacial Residual Stress Relaxation in Perovskite Solar Cells with Improved Stability. *Adv. Mater.* **2019**, *31* (48), 1904408. https://doi.org/10.1002/adma.201904408.

(187) Grancini, G.; Nazeeruddin, M. K. Dimensional Tailoring of Hybrid Perovskites for Photovoltaics. *Nat. Rev. Mater.* **2019**, *4* (1), 4–22. https://doi.org/10.1038/s41578-018-0065-0.

VITA

# So Min Park

## EDUCATION

Jan 2017- Present Ph.D. Department of Chemical and Materials Engineering, University of Kentucky (UK), Lexington, United States Advisor : Professor. Yang-Tse Cheng
Research advisor : Professor. Kenneth Graham

Sep 2014 - Dec 2016 M.S. Department of Chemistry, University of Kentucky (UK), Lexington, United States
Advisor : Professor. Kenneth Graham
Thesis Title: Energetic Effects of Hole Transporting Materials on the Performance of Organometal Halide Perovskite Photovoltaic Cells

Mar 2011 - Feb 2013 - M.S. Department of Material Science and Engineering, Gyeongsang National University (GNU), Jinju, South Korea
Advisor: President. Soon-Ki Kwon, and Professor. Yun-Hi Kim
Thesis Title: "Synthesis and Characterization of Organic Semiconducting Polymers and Oligomers for OTFT and OPV"

Mar 2007 - Feb 2011 B.S. Department of Material Science and Engineering, Gyeongsang National University (GNU), Jinju, South Korea Advisor: Professor. Soon-Ki Kwon

## PROFESSIONAL SERVICE & AFFILIATION

Sep 2018 - May 2019 Vice president, Material Research Society (MRS) University of Kentucky Chapter
Jan 2017 - July 2019 Event chair, Kentucky Chapter, Korean-American Scientists and Engineers Association (KSEA)
Jan 2017 - July 2019 President, Korean Scholar Association at University of Kentucky (KSAUK)
Feb 2011 - Feb 2013 - Researcher, SAMSUNG Display OLED Center
Sep 2008 - Jul 2009 – Government Scholar, 'Teach and Learn in Korea' (TaLK) program

## AWARDS AND HONORS

[7] **"Viji Jeganathan Scholarship for cross-cultural understanding"**, University of Kentucky International Center in April 2019.
[6] **"Poster presentation award"**, Korean-American Scientists and Engineers Association, Kentucky chapter in December 2015.

[5] **"Young Pioneer Researcher Award"**, GNU in October 2012.
[4] **"Capstone Design Grand Prize"**, GNU in November 2010.
[3] **"Portfolio Competition Honorable Mention"**, Accreditation Board for Engineering Education
of Korea in November 2010.
[2] **"Portfolio Competition Grand Prize"**, GNU in September 2010.
[1] **"Scholarship for interdisciplinary research between industry and school"**, GNU in November 2010.

## PUBLICATIONS

[19] M. A. Uddin, J. D. Glover, **S. M. Park**, J. T. Pham, K. R. Graham, 'Growth of highly stable and luminescent anisotropic $CsPbX_3$ (X = Cl, Br, and I) nanocrystals via ligand mediated anion exchange of $CsPbCl_3$ nanocubes with $AlX_3$' **Chemistry of Material, 2020**, 32, 12, 5217-5225

[18] A. A. Masud, W. E. Martin, F. H. Munschi, **S. M. Park**, B. R. Srijanto, K. R. Graham, C. P. Collier, C. I, Richards, 'Mixed metal zero-mode guides (ZMWs) for tunable fluorescence enhancement' **Nanoscale Advances, 2020,** 2, 1894-1903

[17] **S. M. Park**, A. Abtahi, A. Boehm, K. Graham, 'Surface ligands for methylammonium lead iodide films: surface coverage, energetics, and photovoltaic performance' **ACS Energy Letters**, **2020,** 5, 799-806

[16] A. Boehm, T, Liu, **S. M. Park**, A. Abtahi K. Graham, 'Influence of surface ligands on energetic at $FASnI_3/C_{60}$ interfaces and their impact on photovoltaic performance' **ACS Applied Materials & Interfaces, 2020,** 12, 5, 5209-5218

[15] A. Abtahi, S. Johnson, **S. M. Park**, X. Luo, Z. Liang, J. Mei, K. Graham, 'Designing π-conjugated polymer blends with improved thermoelectric power factors' **Journal of Materials Chemistry A**, **2019**, 7, 19774-19785

[14] F. Wang, Z. Ye, H. Sarvari, **S. M. Park**, A. Abtahi, K. Graham, Y. Zhao, Y. Wang, Z. D. Chen, S. Li, 'Humidity-insensitive fabrication of efficient perovskite solar cells in ambient air' **Journal of Power Sources**, **2019**, 412, 359-365

[13] **S. M. Park**, S. Mazza, Z. Liang, A. Abtahi, A. Boehm, S. Parkin, J. Anthony, K. Graham, 'Processing Dependent Influence of the Hole Transport Layer Ionization Energy on Methylammonium Lead Iodide Perovskite Photovoltaics' **ACS Applied Materials & Interfaces**, **2018**, 10, 15548-15557

[12] N. Y. Jeong, M. S. Jang, **S. M. Park**, D. S. Chung, Y. H. Kim, S. K. Kwon, 'Synthesis and Characterization of Highly Soluble Phenanthro[1,10,9,8-c,d,e,f,g]carbazole-based Copolymer: Effects of Thermal Treatment on Crystalline Order and Charge Carrier Mobility' **Dyes and Pigments**, **2018**, 149, 560-565

[11] C. Sun, S. Song, H. G. Song, **S. M. Park**, J. Y. Kim, Y. H. Kim, S. K. Kwon, 'A New Dithienopyridine-Based Polymer for an Organic Electronics' **Journal of Nanoscience and Nanotechnology**, **2017**, 17, 5792-5795

[10] H. G. Song, Y. B. Kim, **S. M. Park**, T. K. An, S. K. Kwon, C. E. Park, Y. H. Kim, 'Synthesis, characterization, and transistor applications of new linear molecules: Naphthayl-ethynyl-anthracene-based small molecules containing different alkyl end group' **Dyes and Pigments, 2016**, 131, 349-355

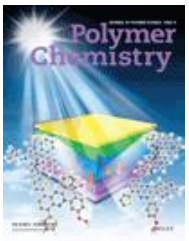


[9] **S. M. Park**, Y. Yoon, C. W. Jeon, H. Kim, M. J. Kim, D. K. Lee, J. Y. Kim, H. J. Son, S. K. Kwon, Y. H. Kim, B. S. Kim, 'Synthesis of Phenanthro[1,10,9,8-cdefg]carbazole-based Conjugated Polymers for Organic Solar Cell Applications' **Journal of Polymer Science: Part A**, **2014**, 52, 6, 796-803 **(front cover article)**

[8] **S. M. Park**, H. N. Kim, S. C. Shin, Y. H. Kim, 'New Semiconducting Copolymers Containing Alkyl Quaterthiophene and Alkoxy Naphthalene Moieties for Organic Thin Film Transistors' **Macromolecular Research, 2014**, 22, 9, 1012-1017

[7] **S. M. Park**, I. Kang, Y. L. Yu, S. Y. Nam, J. Hwang, Y. H. Kim, 'Organic Semiconductor Based on Asymmetric Naphthalene-Thiophene Molecule for Organic Thin Film Transistors' **Journal of Nanoscience and Nanotechnology, 2014**, 14, 8, 6172-6176

[6] H. J. Yun, M. C. Hwang, **S. M. Park**, R. Kim, D. S. Chung, Y. H. Kim, S. K. Kwon, 'Synthesis of a Low-Bandgap Fluorinated Donor-Acceptor Copolymer and Its Optoelectronic Application' **ACS Applied Materials & Interfaces**, **2013**, 5, 6045-6053

[5] T. K. An,** **S. M. Park**,** S. Nam, J. Hwang, S. J. Yoo, M. J. Lee, W. M. Yun, J. Jang, H. Cha, J. Hwang, S. Park, J. Kim, D. S. Chung, Y. H. Kim, S. K. Kwon, C. E. Park, 'Thin Film Morphology Control via a Mixed Solvent System for High-Performance Organic Thin Film Transistors' **Science of Advanced Materials**, **2013**, 5, 1323-1327 **(** equal contribution)**

[4] I. Kang, **S. M. Park**, D. H. Lee, S. H. Han, D. S. Chung, Y. H. Kim, S. K. Kwon, 'Novel Unsymmetric Oligomers Based on Benzo[d,d']Thieno[3,2-b:4,5-b']Dithiophenes for Solution-Processed Organic Field-Effect Transistors' **Science of Advanced Materials**, **2013**, 5, 1-10

[3] **S. M. Park**, I. Kang, H. J. Yun, S. Y. Nam, J. Hwang, Y. H Kim, 'New Si-Based Material with Pyridopyrazine Substituents' **Bull. Korean. Chem. Soc**. **2012**, 33, 3469-3472

[2] S. O. Kim, K. Thangaraju, S. Jung, W. Lu, **S. M. Park**, J. Lee, J. I. Lee, H. Y. Chu, Y. H. Kim, S. K. Kwon, 'Highly Efficient Phosphorescent Organic Light Emitting Diodes Based on Iridium(Ⅲ) Complex with Bulky Substituent Spacers' **Journal of Nanoscience and Nanotechnology**, **2012**, 12, 4375-4378

[1] S. O. Kim, M. W. Lee, S. H. Jang, **S. M. Park**, J. W. Park, M. H. Park, S. H. Kang, Y. H. Kim, C. K. Song, S. K. Kwon, 'Organic semiconductor based on phenylethynyl end-capped anthracene' **Thin Solid Films**, **2011**, 519, 7998-8002